

Lehrstuhl für Thermodynamik  
Technische Universität München

# **Measurement and Scaling of Acoustic Transfer Matrices of Premixed Swirl Flames**

**Panduranga Reddy Alemela**

Vollständiger Abdruck der von der Fakultät für Maschinenwesen  
der Technischen Universität München  
zur Erlangung des akademischen Grades eines  
DOKTOR – INGENIEURS  
genehmigten Dissertation.

Vorsitzender:

Univ.–Prof. Dr.–Ing. habil. Günter H. Schnerr

Prüfer der Dissertation:

1. Univ.–Prof. Dr.–Ing. Thomas Sattelmayer

2. Assoc. Prof. Dr. ir. Jim. B. W. Kok,

University of Twente, Niederlande

Die Dissertation wurde am 09.07.2009 bei der Technischen Universität München eingereicht  
und durch die Fakultät für Maschinenwesen am 20.08.2009 angenommen.



# Acknowledgments

First of all, I am very much thankful to my thesis advisor Univ.–Prof. Dr.–Ing. Thomas Sattelmayer for giving me the kind opportunity to work at Lehrstuhl für Thermodynamik. His valuable guidance and experience in the field of gas turbine combustion helped me to further my knowledge in this field throughout the course of this work.

I would like to thank Univ.–Prof. Dr.–Ing. habil. Günter H. Schnerr for accepting the invitation to be chairman of my thesis defense committee. I am also thankful to Assoc. Prof. Dr. ir. Jim. B. W. Kok for being my thesis co-examiner. My sincere thanks to Dr.–Ing. Christoph Hirsch for his constant encouragement and valuable discussions. He has been a source of motivation at times of difficulty during the project work. This work would not have been possible without his kind support.

I would like to express my sincere thanks to Prof. Polifke, Ph.D., for his kind interest in my work and for his valuable suggestions.

My special thanks to Prof. Sujith of IIT madras, for his continuous support throughout my career. He is the key person in motivating and recommending me to pursue this wonderful research career at TU–München.

My office and project colleague Dan Fanaca, was of great help through out my thesis work. I remain thankful to him for all his co–operation in conducting the experiments and for his friendly subject and non–subject discussions. I would like to thank Stefanie Bade, for her kind help with my German text translations during this thesis writing. Many thanks to all the colleagues at the chair with whom I spent almost five years with lots of fun and at the same time learning subject, making it a pleasant and productive environment to work. Their enormous support (through "nebenjobs") starting from day one at the chair until my thesis submission is greatly acknowledged.

---

Special thanks to Mrs. Bassett and Mrs. Schulz-Reichwald for all their friendly support in bureaucratic dealings. In particular, Mrs. Bassett who took care of my visa issues very kindly during the final stages of my thesis writing.

I am very much thankful to our mechanical and electric workshop colleagues for their kind understanding and support in building the test rig and conducting the experiments smoothly. Especially, Erich Sieber, Bernhard Strobl and Jens Hümmer for their helpful suggestions and assistance in handling practical problems concerned with experimental work.

I wish to thank all my friends at my hostel (HHG-Garching) with whom I had a very pleasant time and a refreshing environment after work. There are many friends and relatives who had given me their moral and also financial support in India prior to coming Germany. I wish to thank one and all of them from deep of my heart. With out their support I would have never reached this day. Finally I wish to thank my wife Pallavi and my parents in India for having given me moral support and enough strength to complete this task.

This project is funded by Alstom, Bayerische Forschungstiftung, Bayerisches Staatsministerium für Wirtschaft, Forschung und Kunst and Bayerisches Staatsministerium für Wirtschaft, Infrastruktur und Technologie. Their financial support is gratefully acknowledged.

München, Sep 2009

Reddy Alemela

# Abstract

In this work, three alternative ways to determine the thermoacoustical characteristics of lean premixed flames typical for gas turbine combustion systems are investigated. The dynamic flame characteristics given by their transfer matrices are obtained *directly* using the multi microphone technique. These transfer matrices are determined at several operating points on an atmospheric single burner test rig with a scaled down model of an industrial gas turbine burner. Alternatively, the transfer matrices are determined using the *hybrid method* which is based on Rankine-Hugoniot relations and the experimentally derived flame transfer function from OH\*-chemiluminescence measurements.

A network modelling approach is applied to simulate the acoustic behavior of the single burner test rig. The main aim of the network modelling is to provide a functional template with a restricted set of physically motivated parameters that can be determined from regressional analysis of the experimental data (*model based regression method*). The test rig consists of several subsystems like plenum, burner, flame etc., element each characterized by its transfer matrix. The burner is modelled as a pressure loss element with an effective length, while the flame is treated as a concentrated heat release zone with an axial dispersion. In the flame model the heat release fluctuations are assumed to be caused from mass flow fluctuations at the burner exit and fuel equivalence ratio fluctuations at the injector location. The results indicated a very good consistency between the direct, hybrid and model based techniques providing a global check of the methods/tools used for analyzing the thermoacoustic mechanisms of flames. In particular, the model based regression procedure which greatly reduces the experimental effort and therefore allows to provide

---

this flame data for many more operation points is successfully validated.

In order to perform a detailed stability analysis of the industrial gas turbine systems using the network model approach the dynamic flame characteristics are to be known at several operating points. Therefore, relevant scaling rules to calculate the flame characteristics at other operating points from a known operating point are presented. A simplified geometric flame length model was used to calculate the flame lengths at several operating points. The mean and distributed time delays characterizing the flames are obtained. These are proportional to the calculated flame length. A new correlation to calculate the value of the flame interaction index has been proposed. The comparison between the measured and modelled flame lengths and convective time delays showed an excellent agreement demonstrating the capability of the model to reproduce the experimental data in the range of operation of the burner.

# Zusammenfassung

In dieser Arbeit werden drei verschiedene Methoden zur Charakterisierung von thermoakustischen Instabilitäten untersucht, die bei der mageren Vormischverbrennung in Gasturbinen auftreten. Das dynamische Flammenverhalten erhält man direkt aus den Transfermatrizen, die mit der Multimikrofonmethode bestimmt werden. Die Transfermatrizen werden an verschiedenen Stellen des atmosphärischen Einzelbrennkammerversuchsstands bestimmt, in dem ein Modell eines Industriebrenners eingebaut ist. Ebenso, sind die Transfermatrizen mit der Hybrid-Methode bestimmbar. Diese basiert auf den Rankine-Hugoniot Beziehungen und der experimentell ermittelten Flammentransferfunktion aus den OH\*-Chemilumineszenz Messungen.

Um das akustische Verhalten des Einzelbrennkammerversuchsstandes zu simulieren, wird ein Netzwerkmodell verwendet. Das Ziel dieses Modells ist es, ein Werkzeug bereitzustellen, das auf physikalische Parameter basiert, die aus der reduzierten Analyse der experimentellen Daten festgelegt werden (Modellbasierte Reduktionsmethode). Dabei werden die verschiedenen Bereiche des Versuchsstands, wie das Plenum, der Brenner, die Flamme, ... jeweils mit ihrer Transfermatrix charakterisiert. Der Brenner wird mit einem Druckverlust-Element mit einer effektiven Länge modelliert. Die Flamme dagegen wird als konzentrierte Wärmefreisetzungszone mit axialer Verteilung behandelt. Die Ursache der Wärmefreisetzungsfuktuationen wird im Flammenmodell als Fluktuationen des Massenstroms am Brenneraustritt und als Fluktuationen der Luftzahl an der Gaseindüsungposition angenommen. Die Ergebnisse zeigen eine sehr gute Übereinstimmung zwischen der direkten, der hybriden und der modellbasierten Methode, die eine allgemeine Kontrolle der Methoden darstellen, die zur Analyse des thermoakustischen Verhaltens

---

dienen. Insbesondere ist die modellbasierte Reduktionsmethode erfolgreich validiert. Sie reduziert den experimentellen Aufwand deutlich und erlaubt deshalb das Bereitstellen von Flammendaten zusätzlicher Betriebspunkte.

Um eine detaillierte Stabilitätsanalyse einer Industriegasturbine mit Hilfe des Netzwerkmodells durchzuführen, müssen die dynamischen Flammeneigenschaften von bestimmten Betriebspunkten bekannt sein. Es werden relevante Skalierungsregeln zur Berechnung der Flammeneigenschaften an Betriebspunkten auf Basis der Eigenschaften von bekannten Punkten abgeleitet. Für die Berechnung der Flammenlänge wird ein vereinfachtes geometrisches Flammenlänge-Modell verwendet. Mit diesem Modell erhält man den mittleren Zeitverzug und die Zeitverzugsverteilung, die proportional zur Flammenlänge sind. Des Weiteren wird eine neue Korrelation zur Berechnung des Flammeninteraktionsindex vorgeschlagen. Der Vergleich zwischen der gemessenen und der modellbasierenden Flammenlänge sowie dem konvektiven Zeitverzug zeigt eine hervorragende Übereinstimmung und demonstriert somit die Fähigkeit des Modells, experimentelle Daten im Betriebsbereich des Brenners zu reproduzieren.

# Contents

<b>1</b>	<b>Introduction</b>	<b>1</b>
1.1	Lean premixed combustion instabilities . . . . .	1
1.1.1	Instability driving mechanisms . . . . .	3
1.1.2	Instability damping mechanisms . . . . .	5
1.2	Various approaches to the problem . . . . .	6
1.2.1	Modelling . . . . .	6
1.2.2	Experimental methods . . . . .	9
1.3	Stability analysis . . . . .	11
1.3.1	Scaling rules . . . . .	12
1.4	Thesis Overview . . . . .	13
<b>2</b>	<b>Acoustic Theory</b>	<b>15</b>
2.1	Linearized acoustic relations . . . . .	15
2.2	Wave equation and solution . . . . .	18
2.2.1	Convective wave equation . . . . .	20
2.2.2	Wave propagation with damping . . . . .	21
2.3	Duct element . . . . .	23
2.4	Compact elements . . . . .	24
2.4.1	Compact element with losses . . . . .	25
2.4.2	Burner as a compact element . . . . .	29
2.5	Acoustic flame model . . . . .	29
2.5.1	Rankine–Hugoniot relations for acoustic quantities . . . . .	29
2.5.2	Flame transfer functions and transfer matrices . . . . .	32
2.5.3	Flame as sensitive time lag model . . . . .	33
2.5.4	Flame as a distributed time lag model . . . . .	34
2.6	Reflection coefficient and impedance . . . . .	38

---

2.7	Low order network model . . . . .	39
<b>3</b>	<b>Test Rig and Measurement Techniques</b>	<b>43</b>
3.1	Single burner test rig . . . . .	43
3.2	Measurement techniques . . . . .	53
3.2.1	Direct acoustic transfer matrix measurement . . . . .	53
3.2.2	Constant temperature anemometer . . . . .	57
3.2.3	OH*- chemiluminescence . . . . .	59
3.2.4	Particle image velocimetry . . . . .	60
<b>4</b>	<b>Experimental Results and Discussion</b>	<b>62</b>
4.1	Operating domain . . . . .	62
4.2	Burner transfer matrices . . . . .	67
4.3	Flame transfer matrices . . . . .	74
4.4	Flame transfer function - hybrid method . . . . .	79
4.5	Analytical flame transfer matrix . . . . .	83
4.5.1	Global check . . . . .	83
4.6	Injector premixed mode operation (IPM) . . . . .	84
4.7	Interpretation of flame parameters . . . . .	87
4.8	Network model validation . . . . .	89
4.9	Model based regression method . . . . .	93
4.10	PIV results . . . . .	96
4.10.1	Cold flow field . . . . .	97
4.10.2	Cold and hot flow field comparison . . . . .	100
<b>5</b>	<b>Scaling Rules</b>	<b>105</b>
5.1	Flame length model . . . . .	105
5.2	Flame length comparison . . . . .	108
5.3	Scaling of flame parameters . . . . .	110
<b>6</b>	<b>Summary and Conclusions</b>	<b>115</b>
<b>A</b>	<b>Appendix</b>	<b>118</b>
A.1	Acoustic FEM model . . . . .	118
A.2	Flame length model . . . . .	121
A.3	Data post processing . . . . .	122

# Nomenclature

## Notation

$\bar{p}$	mean value of $p$
$p'$	acoustic fluctuation of $p$
$\hat{p}$	complex amplitude
$p_k$	$p$ at position $k$
$T_{ij}$	the $ij$ element of the matrix $T$
$x^*$	non dimensionalized value of $x$

## Latin Characters

$A_i$	cross sectional area at location $i$
$c$	speed of sound [ $m/s$ ]
$C$	model coefficient
$d$	diameter of the duct [ $m$ ]
$D$	nominal burner exit diameter [ $m$ ]
$e$	relative error, specific internal energy
$\mathbf{f}$	mass inherent external body forces
$f$	Riemann invariant travelling in positive $x$ -direction [ $m/s$ ], frequency [ $Hz$ ]
$g$	Riemann invariant travelling in negative $x$ -direction [ $m/s$ ]
$h$	duct height [ $m$ ]
$i$	imaginary unit
$k, k_i$	wave number, wave number in $i$ -direction
$l$	length [ $m$ ]
$l_t$	turbulent length scale [ $m$ ]

---

$L_f$	flame length [ $m$ ]
<b>m</b>	mass source terms
$\dot{m}$	mass flow rate [ $kg/s$ ]
$\dot{m}_A$	mass flow rate per unit area [ $kg/s - m^2$ ]
$MW_f$	molecular weight of the fuel [ $kg/kmol$ ]
$n$	interaction index, sample index
$N$	total number of microphones, total number of samples
$O$	order of magnitude
$p$	pressure [ $Pa$ ]
$P$	thermal power [ $kW$ ]
<b>q</b>	heat source terms
$\dot{Q}$	heat release rate per unit area [ $W/m^2$ ]
$r$	radius of the duct [ $m$ ]
$R$	reflection coefficient, gas constant [ $J/mol-K$ ]
$s$	entropy [ $J/kg - K$ ]
$s_l$	laminar flame speed [ $m/s$ ]
$t$	time [ $s$ ]
$T$	temperature [ $K$ ]
$u, v, w$	velocity in $x$ -, $y$ - and $z$ -direction [ $m/s$ ]
$U$	nominal burner exit velocity [ $m/s$ ]
$\vec{v}$	velocity vector [ $m/s$ ]
$x, y, z$	Cartesian coordinates [ $m$ ]
$Z$	acoustic impedance

### Greek Characters

$\alpha_0$	flow jet half angle [ $deg$ ]
$\alpha$	thermal diffusivity [ $m^2/s$ ], area ratio, flame half angle [ $deg$ ]
$\beta$	ratio of specific impedance [ $\bar{\rho}_h c_c / \bar{\rho}_h c_h$ ]
$\delta$	thickness of boundary layer, laminar flame front thickness [ $m$ ]
$\gamma$	ratio of specific heats [ $c_p / c_v$ ]
$\lambda$	air excess ratio, wave length [ $m$ ]
$\nu$	kinematic viscosity [ $m^2/s$ ]
$\phi$	equivalence ratio, phase angle [ $rad$ ]
$\Phi$	probability density function

## Nomenclature

---

$\rho$	density [ $kg/m^3$ ]
$\sigma$	time delay distribution [s]
$\sigma_\phi$	time delay distribution due to equivalence ratio fluctuations [s]
$\tau$	average time delay [s]
$\tau_0$	mean shear stress [ $N/m^2$ ]
$\tau_\phi$	average time delay due to equivalence ratio fluctuations [s]
$\zeta$	loss coefficient
$\omega$	angular frequency [ $rad/s$ ]
$\bar{\omega}$	mean reaction rate [ $kmol/s - m^3$ ]

## Indices

<i>ac</i>	acoustic
<i>ad</i>	adiabatic
<i>b</i>	burner
<i>c</i>	cold side, model coefficient
<i>cc</i>	combustion chamber
<i>co</i>	cut-off
<i>conv</i>	convective
<i>crit</i>	critical
<i>d</i>	downstream side, damping
<i>e</i>	exit
<i>eff</i>	effective
<i>exp</i>	experiment
<i>f</i>	flame
<i>h</i>	hot side
<i>hyd</i>	hydraulic
<i>k</i>	position
<i>l</i>	sub layer, laminar
<i>mod</i>	model
<i>OH</i>	OH*–chemiluminescence
<i>Pl</i>	plenum
<i>ref</i>	reference
$\sigma^2$	standard deviation squared
$\tau$	average time delay

---

<i>th</i>	thermal
<i>u</i>	upstream side
0	at the burner exit plane

### Non-Dimensional numbers

$Da_t$	turbulent Damköhler number $[\frac{l_t}{u'} \cdot \frac{s_t^2}{\nu}]$
$He$	Helmholtz number [-]
$Ka$	Karlovitz number $[\sqrt{Re_t}/Da_t]$
$M$	Mach number $[U/c]$
$Pr$	Prandtl number $[\nu/\alpha]$
$Re_t$	turbulent Reynolds number $[u' \cdot l_t/\nu]$
$Sh$	Shear number $[r\sqrt{\omega/\nu}]$
$Str$	Strouhal number $[f X_{OH}/U]$

### Abbreviations

BTM	Burner transfer matrix
BFTM	Burner transfer matrix with flame
CFD	Computational fluid dynamics
Erf	Error function term
FTM	Flame transfer matrix
IPM	Injector premixed mode
MBRM	Model based regression method
MMM	Multi microphone method
OLG	Open loop gain method
PIV	Particle image velocimetry
PPM	Perfectly premixed mode
R-H	Rankine-Hugoniot relations

# 1 Introduction

This thesis is based on work performed by the author at the Lehrstuhl für Thermodynamik, TU–München as part of the research project “Kraftwerke des 21. Jahrhunderts KW21, Teilprojekt – GV4” dealing with combustion oscillations in annular combustion chambers. The goal of this project is to investigate both experimentally and theoretically the dynamic flame characteristics given by their transfer matrices in a single burner combustion chamber and in an annular multi–burner combustion chamber. Special attention is given to the transferability of the results between both configurations. The specific emphasis of this thesis is the development of methods to determine the thermoacoustic characteristics of flames in an atmospheric single burner test rig and check their feasibility before using them in annular test rig.

The first section of this chapter introduces briefly the advantages and problems associated with lean premixed gas turbine combustion technology. Section two describes various approaches to solve the problems with combustion instabilities including different experimental methods used to validate the thermoacoustic models. Section three briefs on the application of network models to perform the stability analysis and its prerequisites like scaling rules. Towards the end section four gives the overview of the thesis.

## 1.1 Lean premixed combustion instabilities

An increased environmental awareness and competitive power production are driving the gas turbine manufacturers towards lean premixed combustion as the prevailing technology in particular for stationary gas turbines. Since the formation of  $NO_x$  (thermal  $NO_x$ ) has a strong dependence on the local temperature in the region of combustion [9, 45], a uniform temperature is desir-

able in the combustion region. This can be achieved by mixing the fuel and air very well before reaching the main reaction zone. Also, limiting the flame temperature using considerable excess air, i.e. lean flames, does not necessarily reduce the thermodynamic efficiency of present gas turbine cycles. This is because in the original (older) gas turbines the primary combustion gases would have been diluted by adding a large quantity of air in the later part of the combustor to produce an appropriate combustor exit temperature, the prime determinant of efficiency. Thus the flame temperature may be lowered for achieving low  $NO_x$  levels without effecting the combustor exit temperature by using the entire air for premixing with the fuel rather than diluting in the later stage. This has made lean premixed combustion a standard combustion technology to meet low  $NO_x$  objectives.

Unfortunately, lean premix technologies increase the combustion stability problems well known as *thermoacoustic instabilities* [10, 37, 46]. Due to the absence of mixture gradients, which provide very stable flames, the flame becomes very sensitive to the perturbations of the velocity and equivalence ratio. Also, the acoustic damping in the combustion chamber is reduced as the dilution air holes and their associated pressure losses are eliminated. These combustion driven oscillations may constrain the operating envelope and power output of installed machines and in some cases, lead to failure of the hot combustion chamber components. These instabilities arise mainly due to the interaction of acoustic waves and unsteady heat release in the combustion chamber. They grow in time depending on the relative phases between the unsteady heat release and pressure at the heat source. This mechanism is described by the Rayleigh criterion [77] represented mathematically as the Rayleigh integral:

$$\oint_t p'(t) \dot{Q}'(t) dt > 0 \quad (1.1)$$

where  $p'$  is the pressure fluctuation and  $\dot{Q}'$  is the heat release rate fluctuation. The Rayleigh integral becomes positive (negative) when the pressure and heat release fluctuations are in phase (out of phase), to enhance (suppress) oscillations. But the acoustic energy gained (Eqn. 1.1) can be lost/reduced due to the

dissipation/damping effects within the combustor. Therefore, the instabilities grow in time only if the energy supplied by the periodic combustion process to the acoustic field is larger than the rate at which the acoustic energy is dissipated within the combustor and/or transmitted through its boundaries. Thus the Rayleigh criterion represents a necessary, but not sufficient criterion for instability to occur.

### 1.1.1 Instability driving mechanisms

The combustion instabilities stated above are due to complex interactions of the flame with the acoustics of the system. The acoustic waves travel back and forth across the entire combustion system. Therefore, the boundary conditions far upstream and downstream of the flame also influence flame stability. An overview of several possible mechanisms that drive combustion instabilities in a gas turbine combustor are shown in the Fig. 1.1. Here a simple combustion system with several individual components like air/fuel supply, burner, combustion chamber with the flame and the combustor exit is considered. The performance of such combustion systems is very much dependent on the degree of air–fuel mixing, the dynamic flame response to inherent turbulence noise and, importantly, to the acoustic properties of the system. The acoustic behaviour of the burner and flame are given by their respective transfer matrices, which relate the acoustic variables pressure  $p'$  and velocity  $u'$  across these elements. Usually these acoustic quantities are expressed in terms of forward ( $f$ ) and backward ( $g$ ) travelling waves known as Riemann Invariants [73]. The supply unit and the combustor exit are characterized acoustically by their boundary conditions given by their impedances ( $Z$ ). The acoustic characteristics of these elements will be discussed in chapter 2.

Now consider small perturbations in the flow field due to turbulence at the burner exit which causes flame area fluctuations and, consequently, heat release fluctuations ( $\dot{Q}'$ ) [46, 89]. This causes fluctuations in volume expansion, producing perturbations of combustor pressure. These fluctuations (in terms of  $f, g$ ) travel with the speed of sound to the end of the combustor and are

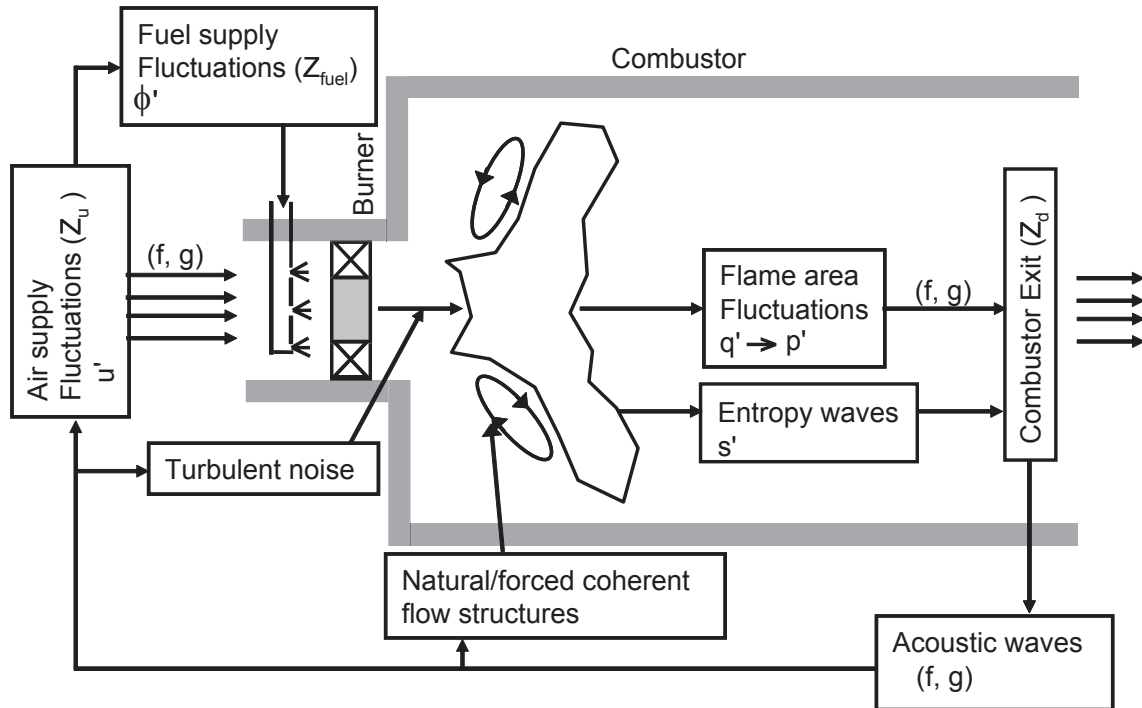


**Figure 1.1:** *Combustion instability driving mechanisms in a model gas turbine combustor*

then reflected back towards the flame zone. The magnitude of the reflected waves depends on the acoustic boundary condition at the combustor exit (e.g. impedance  $Z_d$ ). However, the magnitude of these reflected waves is very small compared to the turbulent noise generated at the flame front and will not directly influence the heat release fluctuations. Instead, these waves travel upstream through the burner into the plenum and modulates the air and fuel flow rate again depending on their respective acoustic boundary conditions (impedance  $Z_u$  and  $Z_{fuel}$ ). These cause perturbations in velocity ( $u'$ ) and equivalence ratio ( $\phi'$ ) within the burner unit. These velocity fluctuations may trigger the already existing shear layer disturbances caused by flow separation from the flame holder (burner) and augments in formation of large scale coherent vortices during the rapid expansion of the jet into the combustor [30,62,67,85]. Often the magnitude of these velocity fluctuations is needed to be above a certain threshold value to actually trigger the flow field and to influence the coherent flow structures.

Initially, these coherent vortices contain combustible mixture. Later, as they propagate, these vortices entrain hot combustion products and get ignited. This causes a rapid combustion and sudden breakdown of the vortical structure into turbulence [7, 96, 98]. Also these vortical structures, which are convected along the mean flow, reach the flame after certain time delay ( $\tau$ ) and cause the flame surface area to fluctuate. This conversion of acoustic velocity fluctuations in convective transport of the fuel is believed to be the most important mechanism leading to thermoacoustic instabilities. An oscillatory heat release rate process is produced that can drive the acoustic field in the combustor. These processes complete the feed back loop to sustain the combustion instabilities. Depending on the phase relation between the heat release and pressure oscillations the combustion instabilities either grow or get suppressed with time as given by Eqn. 1.1.

In addition, the equivalence ratio fluctuations ( $\phi'$ ) convected into the flame zone influence the heat release rate. This effect produces periodic temperature fluctuations causing strong deviations from the isentropic state of the flow well known as entropy wave fluctuations ( $s'$ ) [47, 81]. These temperature non-uniformities in the flow result in local density fluctuations which can interact with the acoustic field. The entropy waves when convected across strong area contractions like the combustor exit, will effect the reflected waves which modulate the combustor acoustics. As discussed previously these waves travel towards the supply side and forms a feed back loop for driving combustion instabilities.

### 1.1.2 Instability damping mechanisms

Acoustic damping plays an important role in the attenuation of combustion instabilities [37, 46]. The acoustic energy gained as discussed in the preceding section can be dissipated by the following mechanisms:

**Viscous and heat transfer mechanisms:** These effects mainly consist of boundary layer losses and flow separation losses. Boundary layer losses occur due to the acoustic perturbations close to the walls/surfaces of the system where viscosity and thermal dissipation are dominant [63, 79]. The flow

separation losses can occur in zones of strong velocity gradients e.g. rapid expansion of the jet into the combustor. Here, the acoustic energy is transferred between the acoustic mode and vorticity mode through the mean flow [56,58]. These mechanisms are in particular important for acoustic losses occurring in recirculation zones and in shear layers.

**Convection and structural damping:** Here the acoustic energy is lost from the system by convection through the mean flow e.g. to the non-rigid combustor walls. Usually these losses increase with increase in Mach number and also with increasing frequencies.

**Transfer of energy from natural modes to other higher modes:** This mechanism consists of transferring energy from the excited modes (natural frequency) to other modes that oscillate at frequencies that are not amplified in the combustor or at which the energy is more rapidly dissipated. Non-linear combustor behavior is the key to promote this transfer of acoustic energy to higher modes or even sometimes to subharmonic modes [11].

## 1.2 Various approaches to the problem

In order to understand and avoid thermoacoustic instabilities numerous theoretical and experimental investigations were carried out in the past, e.g. [10, 16, 42, 68, 84, 89], all of which aim at methods to predict the thermoacoustic stability of a given combustor. The following section gives an overview of these approaches investigated.

### 1.2.1 Modelling

**Network modelling approach:** Complex thermoacoustic systems such as in gas turbines can be represented by simple network models consisting of individual elements of the system like supply duct, burner, flame, choked exit etc.. Each of these elements is represented as multi-port, and described mathematically by its respective *transfer matrix*. In this basic representation, a

transfer matrix gives the linear relationships between acoustic variables e.g. fluctuations of pressure  $p'$  and velocity  $u'$  at the ports of an element. For simple components like ducts, area change etc., the transfer matrix can be derived from the (linearized) equations of conservation of mass and momentum and suitable additional assumptions. However, the determination of the transfer matrix from first principles is not possible due to complex interactions of the acoustic waves across these elements for burners and flames. Therefore, the transfer matrices of these individual elements are determined by appropriate analytical, numerical and experimental methods [2, 54, 61, 72, 92].

Usually burner and flame are treated as compact elements, as the geometric length of these elements is small compared to the acoustic wavelength. From the conservation of mass and the linearized unsteady Bernoulli equation the model for the burner is obtained as a pressure loss element [59, 68]. In this notation the *burner transfer matrix* couples the acoustic field up- and downstream of the burner element, independent of combustion. Several investigations have been made on the coupling between the acoustic field and fluctuating heat release using the well known *Rankine–Hugoniot* (R–H) relations [6, 71]. Crocco and Cheng [10] have proposed the sensitive time lag model, classically known as  $n - \tau$  model, originally for describing the unsteady heat release in liquid propellant rocket motors as a result of pressure fluctuations. But for low Mach number applications like in the gas turbines it can be assumed that the periodic heat release fluctuations are mainly a result of periodic velocity fluctuations from the burner exit after a certain time delay  $\tau$ . The factor  $n$  represents the interaction index, which is a proportionality constant, showing to what extent the heat release fluctuations are amplified with respect to the velocity fluctuations. This simple model has been found to be very useful in predicting the quantitative behavior of combustion oscillations in a variety of cases e.g. [24, 37]. This model was further developed to take into account the axial dispersion of flame perturbations due to the effect of equivalence ratio fluctuations ( $\phi'$ ) [81, 89]. Sattelmayer, [81] has made a detailed analytical investigation on the influence of  $\phi'$  and its axial dispersion on the heat release fluctuations ( $\dot{Q}'$ ) using a model combustor.

A low order network model can be formulated, once all the constituent ele-

ments are expressed analytically, coupling the unknown acoustic variables  $p'$  and  $u'$  at several ports or junctions in terms of their transfer matrices. All the coefficients of the transfer matrices can be combined to form a system matrix relating the unknowns, which can be solved numerically. A short review of previous work carried out exclusively on the development of thermoacoustic tools is presented in [68]. The application of low order models for thermoacoustic stability analysis has been performed by many researchers even as early as in 1956 by Merk [52] for a simple geometry with fuel supply system, a burner head and a combustion system. Later similar studies were carried out on Rijke tubes [32, 76] and lean premixed stationary gas turbine systems [37]. The validation of the low order 1–D network model against experiments and some times numerical data has been carried out by Schuermans et al. 2000 [93] and Gentemann et al. 2003 [28]. Furthermore, the low order network models have been extended to be applicable for annular combustors with 3–D geometries. Under the guidance of Keller. J., Curlier in 1996 [12] has developed an acoustic feed back program (*AFP*) to simulate the acoustic response of a network system. Later a thermoacoustic software  $ta^2$  tool (written as a Mathematica package) has been developed over several years as a result of research projects carried out at ABB corporate research [73]. An advanced version of this software known as  $taX$  is under development at TU München [36].

**Computational methods:** Application of *computational fluid dynamics* (CFD) for thermoacoustic instability problems has gained interest due to its robustness in capturing all relevant processes. It has been proposed recently to use the transient CFD data in combination with an efficient network models [69, 91] for thermoacoustic analysis of gas turbine systems. Here only a part of the problem that cannot be represented by low order network models, such as acoustic boundary condition, burner and flame are computed by CFD. One disadvantage of this approach is that it relies strongly on how well the physics is represented by numerics. Also, due to high computational cost, the length of the time traces computed is limited and very short compared to the experiments. Therefore, very efficient system identification methods are required for the post processing of CFD data. Flohr et al. 2001 and Krebs et al. 2002 [25, 41] have used CFD for modelling the time delay and its distribution in a premixed combustion system.

### 1.2.2 Experimental methods

In order to validate the analytical and numerical (thermoacoustic) models as outlined previously, reliable experimental data is required. Some of the available experimental methods from the literature concerned to thermoacoustic instabilities are explained below:

**Direct transfer matrices:** In analogy to electronic two ports used to characterize passive electronic networks, acoustic two ports are introduced to characterize the plane wave field in complex geometries with ducts, bends, junctions, area changes etc. [1]. The transfer matrix represents mathematically the acoustic two-port and links the acoustic variables like pressure and velocity across the element. The experimental and theoretical determination of acoustical two ports or four pole matrices are presented by Abom, 1992, Munjal and Dodgie, 1990 [1, 54]. To determine the acoustic properties at two ports/four poles two independent test states are required. This is done either by acoustic forcing on one end and changing the load (two load method) or by changing the forcing location (two source location method). It has been found that the two source location method is reliable and can produce two independent acoustic test states. To overcome the measurement uncertainties that prevail in the presence of turbulent flow noise and combustion, this technique was further developed as *multi microphone method* (MMM), where more microphones are used on either side of the test element [22, 23, 60, 63, 79, 87]. Experience has shown that this approach requires very high experimental precision — especially in the presence of mean flow and combustion — sophisticated post-processing of large amounts of raw experimental data, and long test runs, if the transfer matrix is to be recorded accurately over a range of frequencies [22, 23]. This requires a considerable amount of time, e.g. with eight sensors approx. three to four hours per data set. Also, in the case of more complex acoustics an exponential growth of the number of sensors required to resolve the acoustical modes restricts the use of this technique [20], albeit the most accurate, to generic tests with 1-D acoustics.

**Flame transfer function:** *Flame transfer function* (FTF) give the dynamic relation between the heat release fluctuations and the velocity fluctuations as

the function of frequency [33, 39]. It is often determined experimentally and used to represent flames as acoustic elements in low order network models. FTF measurements consist of measuring the OH\*-chemiluminescence representing the heat release fluctuations using an UV-photomultiplier and velocity fluctuations using an anemometer [22]. Here the assumption is made that the OH-chemiluminescence released is directly proportional to the heat release rate [31]. The measured FTF is then used with the R–H relations to get the *flame transfer matrix* (FTM) making it a hybrid method [2]. In the past the hybrid method often failed when there were significant equivalence ratio fluctuations, but recently progress has been made [90]. Extreme care has to be taken while using the hot wire anemometer in particular when measuring in complex geometries and hot environment.

**Model based regression method:** As pointed out previously, it is very difficult (or rather impossible!) to fully characterize the complex acoustic field in an annular test rig with MMM directly. This would require a huge number of dynamic pressure transducers (>30) apart from large calibration effort. For this reason, a novel *model based regression method* (MBRM) which greatly reduces the experimental effort is developed and first implemented on a single burner test rig [2]. Furthermore, this method is developed and applied to determine the FTM in an annular test rig successfully [20]. In this method the acoustic field is described as a superposition of discrete number of eigenmodes following the work of Mastrovito et al. 2005 [50]. The model provides physical constraints that otherwise would have to be replaced by measured data and, thereby, allows reducing the number of sensors. A promising feature of this method is that it requires only one set of measurements unlike the direct method, where two independent set of acoustic measurements are required.

**Flow field investigation:** Flow field investigations by laser based techniques like *particle image velocimetry* (PIV) [75] and intensified high speed OH\*-Chemiluminescence imaging are becoming increasingly popular to understand the fundamental mechanism of thermoacoustic instabilities. Fritag et al. 2006 [26] have performed a detailed analysis of high speed camera phase-locked images to get locally resolved information revealing different regions of high activity within the flame. Static mean flame characteristics like flame

length were obtained using a high speed camera in single burner and annular multi burner combustion chambers [2, 20]. The results indicated that a longer flames exist in the annular combustor compared to the single combustor, although the area ratio between the two configurations was same. A PIV flow field investigation was carried out to understand these differences found in both configurations [21]. The results indicated a free swirling jet flow regime in contrast to a swirling wall jet regime in annular and single burner configurations, respectively, depending on the critical area confinement ratio [27]. Based on these results, it is very important to implement the appropriate corrections to the single burner results before these are used for the stability analysis of the annular combustion chambers.

### 1.3 Stability analysis

A stability analysis of a complex combustion system can be performed using a low order network model as introduced in the previous section. Several authors have used network models representing the Rijke tube as a basic example to understand the complex combustion instability theory [15, 40, 51]. The stability of the system is determined by searching for the eigenmodes and eigenfrequencies by solving the system of equations [57, 83]. The imaginary part of the eigenfrequencies then tells us whether the system is linearly stable (if infinitesimal perturbations die out with time) or unstable (if the perturbations grow). This method is well known as dynamic stability analysis. Additionally, acoustic damping or loss mechanisms can also be included in the network model based stability analysis.

However, in this approach, the finding of the roots numerically depends on the initial guess value and is sometimes very difficult to find all the eigenfrequencies that may be located any where in the complex plane. For some cases the coefficients of the system matrix are known only for real-valued frequencies for e.g. FTM determined from experiments. So one cannot solve for complex-valued roots of the characteristic equation, as the determinant of the system matrix away from the real axis is not known [68]. To overcome this problem, the “Generalized Nyquist criterion” can be used to analyze the sta-

bility of thermoacoustic systems by generating Nyquist plots as proposed by Sattelmayer and Polifke, 2003 [84]. This method is very powerful and it can be applied to networks for which the characteristic equation cannot be evaluated for complex valued frequencies.

### 1.3.1 Scaling rules

In order to perform a detailed stability analysis using a low order network model as discussed above the dynamic flame parameters (e.g.  $n, \tau$ ) are required to characterize each individual operating point. These parameters can be obtained either experimentally, analytically or from CFD. But, the experimental determination of these parameters in the entire range of operation of burners is very costly and cumbersome. To solve this issue flame parameters are often obtained from atmospheric single burner test rig measurements and only at few relevant operating points. These results need to be scaled to represent all other operating points. Therefore, it is highly desirable to have reliable and effective **scaling rules** as a function of thermal power, equivalence ratio and preheat temperature. An earlier investigation [33] has shown that the mean convective time delays can be computed from a simplified heat release profile exiting from a typical swirl burner. Scaling laws for the prediction of thermoacoustic characteristics in dependence of the main operating parameters were formulated and validated for premixed flames by Lohrman and Büchner, 2004 and Russ et al., 2007 [48, 80]. They have obtained a characteristic mean time delay model based on Strouhal number scaling. The mean time delays strongly depend on the turbulent flame speed which in turn depends on the operating point. The mean time delay was obtained as a function of turbulent flame speed and flame geometry (flow angle).

Damköhler, 1940 [13] has presented an early theoretical expression for the turbulent burning velocity. This theory has been applied to determine the turbulent flame speed for large-scale and small-scale turbulence [65]. One of the prerequisites for proper estimation of turbulent flame speed is to take into account the effect of turbulent macro scales i.e., length scale  $l_t$ , RMS velocity  $u_{rms}$  and laminar flame speed  $s_l$ . The laminar flame speed for methane

as a function of equivalence ratio, preheat temperature and operating pressure can be calculated following Peters, 1997 [64]. An estimate of turbulent quantities can be obtained as shown in Wäsle et al. 2005 [99]. Blow out characteristics were captured with classical Damköhler number scalings to predict blowoff equivalence ratios with syngas mixture compositions [55]. Hoffmann et al. 1994 & 1997 [34, 35] performed experiments and developed a model to predict the stability limits of turbulent swirling flames in unconfined geometries based on Peclet number. Still, with respect to prediction of proper convective time delays and development of scaling theories reliable experimental data is required covering several operating points.

### 1.4 Thesis Overview

Methods to determine the dynamics of premixed flames stabilized with a scaled down industrial burner in an atmospheric test rig will be presented. Two gas injection strategies are investigated. In the **Perfectly Premixed Mode** (PPM), mixture is generated far upstream of the burner and temporal as well as spatial mixture inhomogeneities are prevented by static mixers, whereas in the **Injector Premixed Mode** (IPM), the mixture is generated by fuel injectors in the burner. This results in temporal as well as spatial mixture inhomogeneities. The investigation is made in both *static* and *dynamic* operation. In static operation the flow field is not excited externally and the flow field is expected to behave as in a steady state. On the other hand, in dynamic operation the flow field is excited externally using sirens.

**Chapter 2** introduces the relevant acoustic theory starting from conservation equations to the linearized wave equation. The 1D solution of this wave equation is used to represent the wave propagation in simple ducts, also including damping. Relations representing the burner and flame as compact elements are derived. The flame model based on sensitive time lag is also presented. Towards the end of the chapter the low order network model used to simulate the experiments will be illustrated.

In **chapter 3**, the experimental test facility and the measurement techniques

applied in this study are presented. In particular, low reflecting boundary conditions were desired for precise acoustic measurements. This was achieved by implementing an end plate with porosity. Later, the details of the data acquisition procedure and the consecutive application of the post processing tools developed will be discussed.

The experimental results obtained with various methods are discussed in **chapter 4**. The operating domain covering the static and dynamic measurements is presented. The transfer matrices determined from direct MMM are compared with hybrid and analytical methods. An interpretation of the flame parameters obtained in both PPM and IPM operation is presented. The low order network model validation procedure is discussed. A new model based regression method, which requires only one test state to determine the flame parameters, is demonstrated. Towards the end, the PIV results obtained from the single and annular test rig will be discussed.

**Chapter 5** introduces scaling rules that were developed to determine the dynamic flame parameters at several operating points from a known operating point. The basic geometric flame model used to predict the flame lengths is presented and compared with measured flame lengths. Later the sensitive time lags and their distributions are obtained. A new correlation to scale the values of the interaction index ( $n$ ) based on flame length and sensitive time lag is proposed and validated against the experimental results.

The thesis comes to an end with an overall summary and important conclusions in **chapter 6**.

## 2 Acoustic Theory

This chapter has two main parts. In the first part, the relevant acoustic theory for wave propagation in fluids will be discussed. From basic conservation equations the linearized 1-D acoustic wave equation is derived and the assumptions which were made for simplification are stated. The solutions of this wave equation are used to represent the plane wave propagation in ducts with one dimensional flow field, in terms of *Riemann invariants*  $f$  and  $g$ . The influence of damping on the wave propagation is also considered. In the second part, the acoustic relations representing the compact elements like burner and flame are derived. An acoustic flame model based on the sensitive time lag is presented. Towards the end a low order network model developed to simulate the test rig used in the experiments will be discussed.

### 2.1 Linearized acoustic relations

The basic conservation equations for mass, momentum and energy and the equation of state can be written in differential form [78] as follows:

$$\frac{\partial \rho}{\partial t} + \nabla \cdot (\rho \vec{v}) = \mathbf{m} \quad (2.1)$$

$$\rho \frac{\partial \vec{v}}{\partial t} + \nabla \cdot (\rho \vec{v} \cdot \vec{v}) + \nabla p = \mathbf{f} \quad (2.2)$$

$$\rho \frac{\partial}{\partial t} \left( e + \frac{1}{2} \vec{v} \cdot \vec{v} \right) + \nabla \cdot \left( \rho \vec{v} \left( e + \frac{1}{2} \vec{v} \cdot \vec{v} \right) \right) + \nabla \cdot (p \vec{v}) = \mathbf{q} \quad (2.3)$$

$$p = p(\rho, s) \quad (2.4)$$

where  $\mathbf{m}$  is the mass source terms,  $\mathbf{f}$  denotes the external body forces and the viscous forces and  $\mathbf{q}$  represents the heat sources. Assuming a frictionless flow

without inherent body forces and heat conduction, the conservation equations can be simplified to a large extent. In acoustics the fluctuations of pressure and density are considered to be very small compared to the mean quantities. The flow variables  $p, u, \rho$  can be decomposed into their mean and oscillating quantities as

$$p(\mathbf{X}, t) = \bar{p} + p'(\mathbf{X}, t) \quad (2.5)$$

$$\vec{v}(\mathbf{X}, t) = \bar{v} + v'(\mathbf{X}, t) \quad (2.6)$$

$$\rho(\mathbf{X}, t) = \bar{\rho} + \rho'(\mathbf{X}, t). \quad (2.7)$$

Here  $\mathbf{X}$  is the local coordinate,  $t$  is the time, the overbar represent the mean quantities and the primed quantities represent their acoustic fluctuating components. Now substituting the acoustic quantities into the conservation equations (Eqns. 2.1 & 2.2) without source terms and linearizing around their mean values, one can get the equations for acoustic perturbations in 1-D without mean flow ( $\bar{v} = 0$ ) as

$$\frac{\partial \rho'}{\partial t} + \bar{\rho} \frac{\partial u'}{\partial x} = 0 \quad (2.8)$$

$$\bar{\rho} \frac{\partial u'}{\partial t} + \frac{\partial p'}{\partial x} = 0. \quad (2.9)$$

From the basic laws of thermodynamic for a reversible process we get

$$T ds = de + pd(\rho^{-1}). \quad (2.10)$$

Using the equation for mechanical energy obtained from the simplified mass and momentum conservation laws (Eqns. 2.1 & 2.2)

$$\frac{\partial e}{\partial t} - \frac{p}{\rho^2} \frac{\partial \rho}{\partial t} = 0 \quad (2.11)$$

we get the equation for entropy as

$$\frac{\partial s}{\partial t} + \vec{v} \cdot \nabla s = 0, \quad (2.12)$$

which means that the entropy for each particle is constant (isentropic flow). Now the set of equations for acoustic perturbations can be completed by obtaining a relation between the pressure and density from the equation of state (Eqn. 2.4)

$$p = \rho^2 \left( \frac{\partial e}{\partial \rho} \right)_s \quad (2.13)$$

$$T = \left( \frac{\partial e}{\partial s} \right)_\rho. \quad (2.14)$$

Equation 2.13 can be written in differential form using Taylor series, after neglecting higher order terms, as

$$dp = \left( \frac{\partial p}{\partial \rho} \right)_s d\rho + \left( \frac{\partial p}{\partial s} \right)_\rho ds. \quad (2.15)$$

With  $ds = 0$  and

$$c^2 = \left( \frac{\partial p}{\partial \rho} \right)_s \quad (2.16)$$

where  $c$  is the mean speed of sound, we get the following relation for acoustic pressure and density

$$p' = c^2 \rho'. \quad (2.17)$$

## 2.2 Wave equation and solution

A linearized wave equation can be derived by differentiating Eqn. 2.8 with respect to  $t$  and Eqn. 2.9 with respect to  $x$  and subtracting one from another in order to eliminate the acoustic velocity. This yields the following relation:

$$\frac{\partial^2 \rho'}{\partial t^2} - \frac{\partial^2 p'}{\partial x^2} = 0. \quad (2.18)$$

This equation is known as 1-D acoustic wave equation and using Eqn. 2.17 the wave equation in its classical form can be obtained as

$$\frac{\partial^2 p'}{\partial t^2} - c^2 \frac{\partial^2 p'}{\partial x^2} = 0. \quad (2.19)$$

**Properties of the wave equation:** The wave equation is linear allowing superposition of solutions. The wave equation is homogeneous, and has no forcing terms, which drive or damp the pressure perturbations. The wave equation (Eqn. 2.19) can be factorized and represented as

$$\left( \frac{\partial}{\partial t} + c \frac{\partial}{\partial x} \right) \left( \frac{\partial}{\partial t} - c \frac{\partial}{\partial x} \right) p' = 0. \quad (2.20)$$

The general solution of the wave equation from D'Alembert's method for 1-D can be obtained as

$$\frac{p'(x, t)}{\bar{\rho}c} = f(x - ct) + g(x + ct) \quad (2.21)$$

where  $f$  and  $g$  are the arbitrary constants determined by boundary and initial conditions. It can be seen from the arguments  $x \pm ct$ , that  $f$  represents

the wave propagating in the positive  $x$ -direction and  $g$  represents the wave running in the negative  $x$ -direction. This solution is in particular useful in determining the acoustic variables in hard walled ducts with planar propagating waves. The factor  $\bar{\rho} c$  is used to normalize the pressure and attain units that are consistent with velocity.

Using the general solution of the wave equation (Eqn. 2.21) in the Eqn. 2.9 (also known as linearized Euler equation), the acoustic velocity can be obtained in terms of  $f$  and  $g$  as

$$u'(x, t) = f(x - ct) - g(x + ct). \quad (2.22)$$

Using Eqns. 2.21 and 2.22 the Riemann invariants  $f$  and  $g$  can be expressed in terms of  $p'$  and  $u'$  as

$$f = \frac{1}{2} \left( \frac{p'}{\bar{\rho}c} + u' \right) \quad (2.23)$$

$$g = \frac{1}{2} \left( \frac{p'}{\bar{\rho}c} - u' \right). \quad (2.24)$$

Now assuming a harmonic time dependence of the Riemann invariants in exponential form  $e^{i\omega t}$ , a harmonic solution of the wave equation (Eqn. 2.19) can be obtained. From Eqns. 2.21 and 2.22 we get

$$\frac{p'(x, t)}{\bar{\rho}c} = f \cdot e^{i\omega(t-x/c)} + g \cdot e^{i\omega(t+x/c)} \quad (2.25)$$

$$u'(x, t) = f \cdot e^{i\omega(t-x/c)} - g \cdot e^{i\omega(t+x/c)}. \quad (2.26)$$

Here  $\omega = 2\pi f$  represents the angular frequency of the wave under consideration. Using the wave number defined as  $k = \omega/c$ , the Eqns. 2.25 and 2.26 can be written as

$$\frac{p'(x, t)}{\bar{\rho}c} = f \cdot e^{(i\omega t - ikx)} + g \cdot e^{(i\omega t + ikx)} \quad (2.27)$$

$$u'(x, t) = f \cdot e^{(i\omega t - ikx)} - g \cdot e^{(i\omega t + ikx)}. \quad (2.28)$$

This form of the harmonic solution in complex notation is very handy, especially in formulating acoustic relations for the wave propagation in the context of network modelling.

### 2.2.1 Convective wave equation

The wave equation with mean flow can be derived similarly as shown in the previous section using the acoustic conservation equations (from Eqns. 2.8 & 2.9). Now the mean velocity is non-zero,  $\bar{u} \neq 0$  so the linearized Euler equations in 1-D become

$$\left( \frac{\partial}{\partial t} + \bar{u} \frac{\partial}{\partial x} \right) \frac{p'}{c^2} + \bar{\rho} \frac{\partial u'}{\partial x} = 0 \quad (2.29)$$

$$\bar{\rho} \left( \frac{\partial u'}{\partial t} + \bar{u} \frac{\partial u'}{\partial x} \right) + \frac{\partial p'}{\partial x} = 0. \quad (2.30)$$

Subtracting the divergence ( $\frac{\partial}{\partial x}$ ) of the momentum conservation law (Eqn. 2.30) from the total time derivative ( $\partial_t + \bar{u}\partial_x$ ) of the mass conservation law (Eqn. 2.29) to eliminate  $u'$  the *convective wave equation* is obtained as

$$\left( \frac{\partial}{\partial t} + \bar{u} \frac{\partial}{\partial x} \right)^2 p' - c^2 \frac{\partial^2 p'}{\partial x^2} = 0. \quad (2.31)$$

It can be seen by comparing Eqn. 2.31 with Eqn. 2.19 a structurally equal ansatz, will solve Eqn. 2.31. We obtain in analogous to Eqns. 2.21 and 2.22

$$\frac{p'(x, t)}{\bar{\rho}c} = f(x - (c + \bar{u})t) + g(x + (c - \bar{u})t) \quad (2.32)$$

$$u'(x, t) = f(x - (c + \bar{u})t) - g(x + (c - \bar{u})t). \quad (2.33)$$

Here, the solution can be interpreted as the forward travelling wave  $f$  with a propagation speed of  $c + \bar{u}$  and the backward travelling wave  $g$  with a propagation speed of  $c - \bar{u}$ . The harmonic solution of the wave equation can be obtained as

$$\frac{p'(x, t)}{\bar{\rho}c} = f \cdot e^{(i\omega t - ik_+x)} + g \cdot e^{(i\omega t + ik_-x)} \quad (2.34)$$

$$u'(x, t) = f \cdot e^{(i\omega t - ik_+x)} - g \cdot e^{(i\omega t + ik_-x)} \quad (2.35)$$

with the convective wave number defined as

$$k_{\pm} = \frac{\omega}{c \pm \bar{u}} = \frac{k}{1 \pm M}. \quad (2.36)$$

### 2.2.2 Wave propagation with damping

Acoustic damping plays an important role in combustion instabilities. Increased damping due to the thermo viscous effects may even suppress self excited acoustic instabilities at the resonance frequencies. To investigate the influence of damping on the wave propagation, the damped duct is introduced following the work of Peters et al. 1993 [63]. In the presence of mean flow, the convective effect on the damping of acoustic waves has been studied by Ronneberger, 1977 [79]. He proposed a quasi-laminar theory with two important parameters:  $\delta_{ac} = \sqrt{2\nu/\omega}$  the thickness of acoustic boundary layer and  $\delta_l \approx 10\nu/\sqrt{\tau_0/\rho_0}$ , the thickness of the viscous sublayer of the turbulent mean flow boundary layer. Here  $\nu$  is the kinematic viscosity,  $\rho_0$  is the density of the fluid and  $\tau_0$  is the mean shear stress. If their ratio is small ( $\delta_{ac}/\delta_l \ll 1$ ), the

damping of acoustic waves is not influenced by the turbulent stresses. But for the case  $\delta_{ac}/\delta_l > 1$ , turbulence effects the damping. In the low frequency approximation, for which  $kr \ll 1$  and for high shear numbers  $Sh = r\sqrt{\omega/\nu} \gg 1$ , with  $r$  the radius of the duct and  $\nu$  the kinematic viscosity of the medium, the acoustic plane wave propagation is governed by an additional damping term. This results in a correction factor to the wave number (Eqn. 2.36) as follows:

$$k_{\pm} = \frac{\omega}{c \pm \bar{u}} \left[ 1 + \frac{1-i}{\sqrt{2}Sh} \left( 1 + \frac{\gamma-1}{\sqrt{Pr}} \right) - \frac{i}{Sh^2} \left( 1 + \frac{\gamma-1}{\sqrt{Pr}} - \frac{\gamma\gamma-1}{2Pr} \right) \right] \quad (2.37)$$

where  $Pr$  is the Prandtl number and  $\gamma$  the ratio of specific heats. The temperature dependency of the kinematic viscosity is given by  $\nu = A + B(T - T_{ref})$ , with  $T$  the absolute temperature of the fluid (air) inside the duct,  $A = 1.51 \times 10^{-5} m^2/s$ ,  $B = 9.2 \times 10^{-8} m^2/s/K$  and  $T_{ref} = 293.16K$ . The first correction term in the equation, which is inversely proportional to the shear number, changes the phase velocity of the acoustic plane waves. The second term which is inversely proportional to  $Sh^2$  is usually neglected for  $Sh > 20$  (Davies, 1988 [14]). In the present study the value of the shear number for the lowest frequency of interest (10Hz) with a radius of the duct around 60 mm will be  $Sh = 74$ . Therefore the second term can be neglected. With an additional factor ( $C_d$ ), the roughness of the inner surface of the duct, taken into account the Eqn. 2.37 becomes

$$k_{\pm} = \frac{\omega}{c \pm \bar{u}} \left[ 1 + C_d \frac{1-i}{\sqrt{2}Sh} \left( 1 + \frac{\gamma-1}{\sqrt{Pr}} \right) \right]. \quad (2.38)$$

As can be seen from the Eqn. 2.38 the effect of damping is two-fold. The real part will increase the wave number which reflects the well known decrease of the resonance frequency in damped systems when compared with undamped systems. The imaginary part provides amplitude damping according to

$$\alpha_d = \frac{\omega}{c \pm \bar{u}} \left[ \frac{C_d}{\sqrt{2}Sh} \left( 1 + \frac{\gamma-1}{\sqrt{Pr}} \right) \right]. \quad (2.39)$$

With these equations implemented in the network models the wave propaga-

tion in damped ducts can be obtained and hence the acoustic response in the presence of damping can be simulated.

## 2.3 Duct element

The present study is oriented to develop a low order 1-D network model representing a gas turbine combustion system which mainly consists of geometries that can be represented by straight ducts and few connecting elements to represent area changes. Therefore the acoustic wave propagation in a straight uniform duct will be discussed in this section. Consider a simple duct of length  $l$  and diameter  $d$  with mean flow. Assuming a harmonic, 1-D wave propagation, the acoustic pressure (Eqn. 2.34) at two different locations  $x_1$  and  $x_2$  at a given moment  $t_0$  in time can be related by a linear set of equations [22, 87] as

$$\begin{pmatrix} \frac{p'_1}{\rho c} \\ \frac{p'_2}{\rho c} \end{pmatrix} = \begin{pmatrix} e^{-ik_+x_1} & e^{ik_-x_1} \\ e^{-ik_+x_2} & e^{ik_-x_2} \end{pmatrix} \begin{pmatrix} f \\ g \end{pmatrix}. \quad (2.40)$$

Alternatively, the relation between Riemann invariants at two locations  $x_1$  and  $x_2$  can be obtained using Eqn. 2.34 and expressed in terms of a linear transfer matrix as [87]

$$\begin{pmatrix} f \\ g \end{pmatrix}_2 = \underbrace{\begin{pmatrix} e^{-ik_+(x_2-x_1)} & 0 \\ 0 & e^{ik_+(x_2-x_1)} \end{pmatrix}}_{\text{TM}_{fg}(\omega)} \begin{pmatrix} f \\ g \end{pmatrix}_1. \quad (2.41)$$

The Eqn. 2.41 gives the transfer matrix ( $\text{TM}_{fg}$ ) of the duct element which describes how the acoustic information is being transferred from one end to the other end. Also, the transfer matrix in the  $f$  and  $g$  notation can be easily transformed into  $p$  and  $u$  notation using the coordinate transformation as follows:

$$\text{TM}_{pu} = \Omega \cdot \text{TM}_{fg} \cdot \Omega^{-1} \quad (2.42)$$

$$\text{TM}_{fg} = \Omega^{-1} \cdot \text{TM}_{pu} \cdot \Omega \quad (2.43)$$

$$(2.44)$$

using the transformation matrix

$$\Omega = \begin{pmatrix} 1 & 1 \\ 1 & -1 \end{pmatrix}. \quad (2.45)$$

However, in reality a gas turbine combustion system has not only the duct elements but also area changes that e.g. join ducts of unequal cross section and other connecting elements (node elements). These are called *compact elements* since they either have no physical extent or have lengths that are small compared with the acoustic wave length. Such elements are discussed in detail in the following section.

## 2.4 Compact elements

In the field of thermoacoustics concerned with network modeling the burner and flame are usually represented as *acoustically compact elements* based on the assumption that the geometric length ( $l$ ) of these elements is very small compared to the acoustic wave length ( $\lambda$ ). This condition is represented mathematically by *Helmholtz number*  $He = \frac{\omega l}{c} = k l \ll 1$ . A *compact element* can be interpreted as a discontinuity between two flow states and cannot be described in detail. Here only the relations suitable to match the flow conditions between two elements are derived from the conservation equations. In the acoustic network modelling approach, several elements are interconnected at their junctions. At these junctions the surface areas should be equal. Therefore, appropriate corrections are required for the area change to match with its connecting element. This approach is valid in the low frequency range of interest assuming, 1-D flow field, incompressible, isentropic and irrotational flow without source terms.

### 2.4.1 Compact element with losses

In this section the acoustic relations to represent a *compact element* with losses and inertia will be derived from the conservation of mass and momentum equations [73]. The relations thus developed will be applicable to any element in general with losses like in a sudden area change or a burner with complex acoustic pressure losses. This type of element with an arbitrary geometry can be schematically represented as shown in Fig. 2.1.

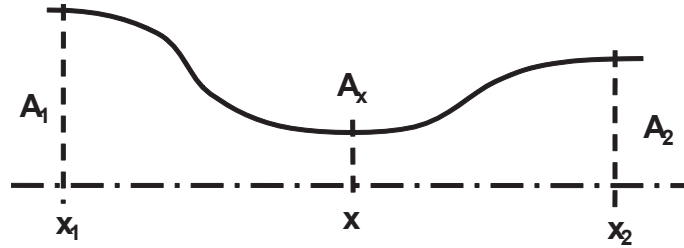


**Figure 2.1:** *Acoustically compact element (courtesy Polifke et al. 1997 [73])*

#### Mass conservation:

By integrating the mass conservation equation (Eqn. 2.1) over a fixed volume gives

$$\frac{\partial}{\partial t} \int_V \rho dV + \int_A \rho \vec{v} d\vec{A} = 0. \quad (2.46)$$

Now assuming a quasi 1-D flow field through the compact element (Fig. 2.1) Eqn. 2.46 can be integrated for the volume enclosed between the two axial planes at  $x = x_1$  and  $x = x_2$  as

$$\frac{\partial}{\partial t} \int_{x_1}^{x_2} \rho(x) A(x) dx + [\rho u A]_1^2 = 0. \quad (2.47)$$

Substituting the acoustic variables as given in Eqns. 2.6 & 2.7 and after linearizing and retaining only the acoustic quantities gives

$$\frac{\partial}{\partial t} \int_{x_1}^{x_2} \rho' A(x) dx + [(\rho' \bar{u} + \bar{\rho} u') A]_1^2 = 0. \quad (2.48)$$

Once again assuming a harmonic time dependency and for density,  $\rho'(x) = \rho_1 + O(kl)$  we get

$$i\omega \rho_1 \int_{x_1}^{x_2} A(x) dx + [(\rho_1 \bar{u} + \bar{\rho} u') A]_1^2 = O(kl)^2. \quad (2.49)$$

Assuming a constant speed of sound and using the relation  $p' = p'/c^2$  we get

$$i\omega \frac{p'_1}{c^2} \int_{x_1}^{x_2} A(x) dx + \left[ \left( \frac{p'_1}{c^2} \bar{u} + \bar{\rho} u' \right) A \right]_1^2 = 0. \quad (2.50)$$

Now defining a reduced length as

$$l_{red} = \int_{x_1}^{x_2} \frac{A(x)}{A_2} dx \quad (2.51)$$

and substituting into Eqn. 2.50, dividing by mean density  $\bar{\rho}$ , one can obtain the acoustic mass conservation equation for a compact element as

$$\frac{i\omega}{c} l_{red} A_2 \frac{p'_1}{\bar{\rho} c} + \left[ \left( \frac{p'_1}{\bar{\rho} c} M + u' \right) A \right]_1^2 = 0. \quad (2.52)$$

The first term in the above equation can often be neglected, using the assumption of compactness, as its absolute value is very small compared to the other terms (for more details see Polifke et al. 1997 [73]). So the equation above is further simplified as

$$\left[ \left( \frac{p'_1}{\bar{\rho} c} M + u' \right) A \right]_1^2 = 0. \quad (2.53)$$

**Momentum conservation:**

From the conservation of momentum (Eqn. 2.2) without source terms the Bernoulli equation for non-stationary, compressible flow field can be obtained. According to Polifke et al. 1997 [73], the Bernoulli equation for compressible and incompressible flow are equivalent up to second order in Mach numbers. Therefore, in this study (gas turbine applications) for low Mach number flows the incompressible Bernoulli equation is applicable. The momentum equation Eqn. 2.2 without source terms is written as

$$\frac{\partial \vec{v}}{\partial t} + \nabla \cdot (\vec{v} \cdot \vec{v}) + \frac{\nabla p}{\rho} = 0. \quad (2.54)$$

Applying this equation for a compact element (Fig. 2.1), i.e. integrating between two points at  $x = x_1$  and  $x = x_2$  in a one dimensional flow field, the Bernoulli equation is obtained:

$$\frac{\partial}{\partial t} \int_{x_1}^{x_2} u \, dx + \left[ \frac{u^2}{2} + \frac{p}{\rho} \right]_1^2 = 0. \quad (2.55)$$

A pressure loss which can occur due to friction or/and flow separation can be obtained from steady state Bernoulli equation between two points as follows:

$$p_1 + \frac{\bar{\rho} u_1^2}{2} = p_2 + \frac{\bar{\rho} u_2^2}{2} + \Delta p. \quad (2.56)$$

Where  $\Delta p$  represents the pressure loss term and is usually defined as

$$\Delta p = \frac{\zeta \bar{\rho} u_2^2}{2}. \quad (2.57)$$

The value of the loss coefficient  $\zeta$  is dependent on the selection of reference cross sectional area which determines the reference velocity up- or downstream of the element. Now substituting Eqn. 2.57 after dividing it by mean density  $\bar{\rho}$  into Eqn. 2.55 to account for pressure losses we get

$$\frac{\partial}{\partial t} \int_{x_1}^{x_2} u \, dx + \left[ \frac{u^2}{2} + \frac{p}{\rho} \right]_1^2 + \frac{\zeta u_2^2}{2} = 0. \quad (2.58)$$

Introducing the acoustic relations (Eqns. 2.5 and 2.6) into Eqn. 2.58, considering the harmonic time dependency of acoustic fluctuations, linearizing and dividing by  $c$  yields

$$\frac{i\omega}{c} \int_{x_1}^{x_2} u' \, dx + \left[ \frac{p'}{\rho c} + M u' \right]_1^2 + M_2 u_2' \zeta = 0. \quad (2.59)$$

With the compactness assumption, from continuity  $u'(x) = u_1' A_1 / A(x)$ , the integral term in Eqn. 2.59 can be approximated as

$$\frac{i\omega}{c} \int_{x_1}^{x_2} u'(x) \, dx = i k u_1' \int_{x_1}^{x_2} \frac{A_1}{A(x)} \, dx = i k l_{eff} u_1'. \quad (2.60)$$

The term  $l_{eff}$  introduced in Eqn. 2.60 takes into account the effect of inertia, i.e. the pressure drop between two reference positions 1 and 2 ( $p_1' - p_2'$ ) will accelerate the fluid between these points, which change the acoustic velocity  $u'$  gradually through the element, leading to a phase shift between pressure drop  $p_1' - p_2'$  and  $u'$  [68].

Finally, the linearized conservation of momentum equation for an acoustically compact element can be obtained after substituting Eqn. 2.60 in to Eqn. 2.59 as

$$i k l_{eff} u_1' + \left[ \frac{p'}{\rho c} + M u' \right]_1^2 + M_2 u_2' \zeta = 0. \quad (2.61)$$

### 2.4.2 Burner as a compact element

As discussed above, burners can also be treated as acoustically compact elements. The linearized conservation equations from mass and momentum (Eqns. 2.52 & 2.61) can be applied to derive a burner transfer matrix relating the acoustic variables  $(p', u')$  up- (1) and downstream (2) as

$$\begin{pmatrix} \frac{p'}{\rho c} \\ u' \end{pmatrix}_2 = \underbrace{\begin{pmatrix} 1 & M_1 - (1 + \zeta)\alpha M_2 - ikl_{eff} \\ \alpha M_1 - ikl_{red} & \alpha \end{pmatrix}}_{BTM} \begin{pmatrix} \frac{p'}{\rho c} \\ u' \end{pmatrix}_1. \quad (2.62)$$

Here the  $\alpha$  represents the area ratio  $A_1/A_2$ . Also, the higher order terms in Mach number are neglected for simplicity. The experience has shown that the influence of the  $T_{21}$  element on the overall transfer matrix is very low and often being neglected [2, 87]. Thus the burner model shown above is completely described by knowing the values of  $l_{eff}$  and  $\zeta$ . However, due to very complex interaction of the acoustics within the burner (*compact element*), these parameters are often obtained by fitting them to the measured transfer matrices or sometimes even to CFD results [25]. A similar type of transfer matrices to represent the burner and even sometimes sudden area changes are presented in the literature [28, 59]. A detailed derivation of the effective length  $l_{eff}$  and reduced length  $l_{red}$  are presented in [22, 28].

## 2.5 Acoustic flame model

### 2.5.1 Rankine–Hugoniot relations for acoustic quantities

Using the same analogy as presented in previous section, the flame can also be treated as a discontinuity in a reacting medium. The flame is considered as a thin sheet with all the heat released in this single plane. Thus, the assumption that axial flame length is small compared to the acoustic wave length (i.e.  $kl \ll 1$ ) is applicable. However, the acoustic relations derived so far without heat source cannot be applied since the local conditions are extremely

non-isentropic. But, the isentropic relations still hold just before and after the flame. The static relations to describe the mean flow discontinuity condition will be obtained from the conservation equations. These relations are linearized across the discontinuity. For the steady case, the conservation equation of mass, momentum, energy and state (Eqns. 2.1-2.4) across a flame sheet with heat addition per unit area  $\dot{Q}$  can be written as

$$[\rho u]_c^h = 0 \quad (2.63)$$

$$[p + \rho u^2]_c^h = 0 \quad (2.64)$$

$$\dot{m}_A \left[ e + \frac{u^2}{2} \right]_c^h + [p u]_c^h = \dot{Q} \quad (2.65)$$

$$\left[ \frac{\rho R T}{p} \right]_c^h = 0 \quad (2.66)$$

with the subscripts  $c$ ,  $h$  representing the cold and hot side of the flame sheet, respectively.  $\dot{m}_A (= \rho u)$  is the mass flow flux observed at the plane of discontinuity (flame sheet). In the equation of state  $R$  represents the gas constant ( $J/kg \cdot K$ ). Using the relations for sound speed in isentropic flow  $c^2 = \gamma p / \rho$  and with caloric properties of the gas  $R$  and  $\gamma$  being assumed to be constant across the flame<sup>1</sup> we get

$$h = c_p T = e + \frac{p}{\rho} = \frac{\gamma p}{(\gamma - 1)\rho}. \quad (2.67)$$

Now using the Eqns. 2.63–2.67, the following jump conditions across the flame well known as *Rankine-Hugoniot* (R–H) relations can be obtained [6, 38, 71]:

---

<sup>1</sup>The temperatures across the flame are assumed to be constant and hence for the ease of notation  $T = \bar{T}$  is used throughout the text hereafter

$$\frac{\rho_c}{\rho_h} = \frac{u_h}{u_c} = 1 + \frac{(\gamma-1)\dot{Q}}{\gamma p_c u_c} + O(M^2) \quad (2.68)$$

$$\frac{p_h}{p_c} = 1 - \frac{(\gamma-1)\dot{Q}}{p_c u_c} M_c^2 + O(M^4) \quad (2.69)$$

$$\frac{T_h}{T_c} = \left(\frac{c_h}{c_c}\right)^2 = 1 + \frac{(\gamma-1)\dot{Q}}{\gamma p_c u_c} + O(M^2). \quad (2.70)$$

With low Mach number assumption, which is the case in this study, the terms that depend on the second and higher orders in Mach number can be neglected. Now substituting the acoustic relations Eqns. 2.5-2.7 into the above equations, linearizing and retaining only the terms up to first order in acoustic quantities, the Rankine-Hugoniot relations for acoustic perturbations can be obtained as

$$\left(\frac{p'}{\bar{\rho}c}\right)_h = \beta \left(\frac{p'}{\bar{\rho}c}\right)_c - \beta \left(\frac{T_h}{T_c} - 1\right) M_c \bar{u}_c \left(\frac{\dot{Q}'}{\bar{Q}} + \frac{u'_c}{\bar{u}_c}\right) \quad (2.71)$$

$$u'_h = u'_c + \left(\frac{T_h}{T_c} - 1\right) \bar{u}_c \left(\frac{\dot{Q}'}{\bar{Q}} - \frac{p'_c}{\bar{p}_c}\right) \quad (2.72)$$

where  $\beta = (\bar{\rho}_c c_c)/(\bar{\rho}_h c_h)$  is the ratio of specific impedances and  $\bar{Q}$  is the average rate of heat addition per unit area. By rearranging the Eqns. 2.71 and 2.72, the heat release fluctuations are expressed in relative terms of acoustic velocity fluctuations as

$$\left(\frac{p'}{\bar{\rho}c}\right)_h = \beta \left(\frac{p'}{\bar{\rho}c}\right)_c - \beta \left(\frac{T_h}{T_c} - 1\right) M_c u'_c \left(1 + \frac{\dot{Q}'/\bar{Q}}{u'_c/\bar{u}_c}\right) \quad (2.73)$$

$$u'_h = -\left(\frac{T_h}{T_c} - 1\right) \gamma M_c \left(\frac{p'}{\bar{\rho}c}\right)_c + \left(1 + \left(\frac{T_h}{T_c} - 1\right) \frac{\dot{Q}'/\bar{Q}}{u'_c/\bar{u}_c}\right) u'_c. \quad (2.74)$$

### 2.5.2 Flame transfer functions and transfer matrices

In order to get the relation between the acoustic quantities up- and downstream of the flame, one has to know how these quantities influence the heat release fluctuations. For low Mach number-perfectly premixed flames generally an assumption is made that the heat release fluctuations are mainly due to the velocity fluctuations upstream of the flame [22, 49]. The flame transfer function (FTF)  $f_Q(\omega)$  as a function of frequency can be defined as the ratio of relative fluctuations of the heat release to the relative fluctuations of the velocity at the burner exit, mathematically represented as

$$f_Q(\omega) = \frac{\dot{Q}'/\bar{\dot{Q}}}{u'_c/\bar{u}_c}. \quad (2.75)$$

The fluctuations of both heat and velocity are normalized with their respective mean values. In the low frequency limit ( $\omega \rightarrow 0$ ) the FTF approaches to a value of unity ( $f_Q(\omega) \rightarrow 1$ ) corresponding to a quasi steady state response of the flame to the velocity fluctuations at the burner exit. A dynamic response of the flame is usually observed towards the higher frequencies, which is very crucial for the prediction of the stability behavior using network models. The FTF can be obtained either theoretically [17, 38, 71] or experimentally [26, 44]. The FTF is measured using an UV-sensitive photomultiplier with the assumption that the  $\text{OH}^*$ -chemiluminescence from the flame is directly proportional to the heat release rate [31]. The velocity fluctuation  $u'_c$  at the burner exit can be directly measured from a constant temperature anemometer (CTA). Also,  $u'_c$  can be extracted by measuring only the acoustic pressure upstream using the 1-D network theory and the BTM, e.g. using Eqn. 2.62 [2].

Now substituting the FTF as defined in Eqn. 2.75 into the acoustic Rankine-Hugoniot relations Eqns. 2.73 and 2.74 and rearranging the equations, the flame transfer matrix (FTM) relating the acoustic pressure and velocity up- (cold,  $c$ ) and downstream (hot,  $h$ ) of the flame can be obtained as

$$\begin{pmatrix} \frac{p'}{\rho c} \\ u' \end{pmatrix}_h = \underbrace{\begin{pmatrix} \beta & -\beta \left( \frac{T_h}{T_c} - 1 \right) M_c (1 + f_Q(\omega)) \\ -\left( \frac{T_h}{T_c} - 1 \right) \gamma M_c & 1 + \left( \frac{T_h}{T_c} - 1 \right) f_Q(\omega) \end{pmatrix}}_{FTM} \begin{pmatrix} \frac{p'}{\rho c} \\ u' \end{pmatrix}_c. \quad (2.76)$$

### 2.5.3 Flame as sensitive time lag model

The FTF can also be obtained by means of an analytical flame model with free parameters. Crocco and Cheng, 1956 [10] have proposed the sensitive time lag model, classically known as  $n - \tau$  model for describing the unsteady heat release in liquid propellant rocket motors. Here the heat release fluctuations are assumed to be due to pressure fluctuations within the combustor. But, for the gas turbine applications with very low Mach number approximation it is assumed that the periodic heat release fluctuations  $\dot{Q}'$  are mainly a result of acoustic velocity (mass flow) fluctuations  $u'_c$  from the burner exit after a certain time delay  $\tau$  [51]. The factor  $n$  represents the interaction index, which is a proportionality constant, showing to what extent the heat release fluctuations are amplified with respect to the velocity fluctuations. These can be represented as

$$u'_h(t) = u'_c(t) + n u'_c(t - \tau) \quad (2.77)$$

$$\Rightarrow \frac{\dot{Q}'(t)}{\bar{Q}} = \frac{n}{\left( \frac{T_h}{T_c} - 1 \right)} \frac{u'_c(t - \tau)}{\bar{u}_c}. \quad (2.78)$$

Substituting the harmonic time dependency of the velocity fluctuations in the above equations we get the heat release fluctuations as a function of frequency, i.e the FTF  $f_Q(\omega)$ , as follows

$$u'_h(t) = u'_c(t) + nu'_c(t)e^{-i\omega\tau} \quad (2.79)$$

$$\Rightarrow \frac{\dot{Q}'(t)}{\bar{\dot{Q}}} = \frac{n}{\left(\frac{T_h}{T_c} - 1\right)} \frac{u'_c(t)}{\bar{u}_c} e^{-i\omega\tau} \quad (2.80)$$

$$\Rightarrow f_Q(\omega) = \frac{\dot{Q}'/\bar{\dot{Q}}}{u'_c/\bar{u}_c} = \frac{n}{\left(\frac{T_h}{T_c} - 1\right)} e^{-i\omega\tau}. \quad (2.81)$$

This simple model has laid a strong foundation for the understanding of the complex thermoacoustic mechanism and also in developing tools for performing stability analysis in various applications [51]. However, this simplistic model is not necessarily valid for practical gas turbine applications, as the heat release rate  $\dot{Q}'$  may respond to velocity and equivalence ratio fluctuations at the location of fuel injection. Sattelmayer, 2003 [81] has demonstrated that equivalence ratio fluctuations and its convective dispersion should be taken into account for stability analysis of gas turbine combustors. Hirsch et al. 2005 [33] have proposed a FTF model that consists of the standard convective time delay distribution as well as swirl induced velocity fluctuations. This model has predicted the specific differences observed between the two FTFs obtained using different burner configurations. Also, Polifke et al. 2001 [70] have investigated the impact of time delay distributions on the combustion instability, using different burner nozzles. It found that with increase of the time delay distribution the stability actually increases. It is noted that the axial extent of flame ( $L_f$ ) may be very small compared to the acoustic wave length ( $\lambda_{ac} = 2\pi c/\omega$ ) and hence compact. But, with respect to the convective wave length of equivalence ratio waves ( $\lambda_{conv} = 2\pi\bar{u}/\omega$ ) it may not be compact. Therefore, the effect of axial time lag distribution has to be included along with a fixed mean time delay for a more realistic description.

#### 2.5.4 Flame as a distributed time lag model

Following the work of Schuermans et al. [87, 89] the heat release fluctuations are considered to be due to both velocity fluctuations and equivalence ra-

fluctuations. Here the fuel transport and correspondingly combustion is assumed to take place with an axial distribution, instead of being occurring at one fixed position without any dispersion. Consequently, the heat release distribution has been approximated with a Gaussian function with a mean time delay  $\tau$  and its standard deviation as  $\sigma$ . A schematic representation of the above assumption is shown in Fig. 2.2. The  $r_i, r_o$  represent the inner and outer radii of the annulus of the burner and the flame axial intensity profile is shown as red solid line.

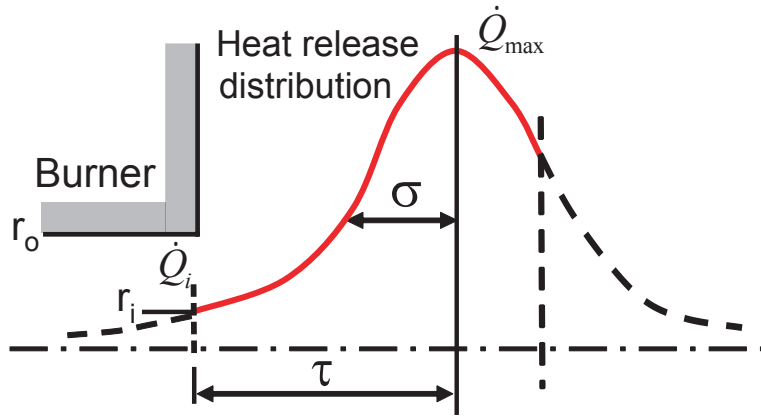


**Figure 2.2:** Schematic of the heat release distribution of the flame close to the burner vicinity. This is approximated with a Gaussian function having mean time delay  $\tau$  and its standard distribution  $\sigma$

As seen from Fig. 2.2, the value of time lag at each location on the flame surface is given by a time lag distribution function (a probability density function) as

$$\Phi_{\tau, \sigma^2}(t) = \frac{1}{\sqrt{2\pi\sigma}} e^{-\frac{1}{2} \frac{(t-\tau)^2}{\sigma^2}}. \quad (2.82)$$

The acoustic disturbances at the burner exit will now propagate into the flame zone according to a mean time delay  $\tau$  similar to that in Eqn. 2.77, and if distributed time delay is also included then

$$u'_h(t) = u'_c(t) + n \int \Phi_{\tau, \sigma^2}(t) u'_c(t - \tau) dt. \quad (2.83)$$

With harmonic time dependency the above equation yields

$$u'_h(\omega) = u'_c(\omega) + n u'_c(\omega) \int \Phi_{\tau, \sigma^2}(t) e^{-i\omega\tau} dt. \quad (2.84)$$

The integral term in the Eqn. 2.84 can be written as

$$\int \Phi_{\tau, \sigma^2}(t) e^{-i\omega\tau} dt = e^{-\frac{1}{2}\omega^2\sigma^2 - i\omega\tau} \left( \frac{1}{2} \text{Erf} \left[ \frac{t - \tau + i\sigma^2\omega}{\sqrt{2}\sigma} \right] \right). \quad (2.85)$$

Neglecting the error function term in Eqn. 2.85 and then substituting it into Eqn. 2.84 yields the relation for fluctuating velocity as

$$u'_h(\omega) = u'_c(\omega) + n u'_c(\omega) e^{-\frac{1}{2}\omega^2\sigma^2 - i\omega\tau}. \quad (2.86)$$

With this equation the corresponding heat release fluctuations and thus the FTF for PPM operation can be written as

$$f_Q(\omega) = n \left( \frac{T_h}{T_c} - 1 \right)^{-1} e^{-i\omega\tau} e^{-\frac{1}{2}\omega^2\sigma^2}. \quad (2.87)$$

It will be derived later (in chapter 5) that the value of interaction index will be  $n = f(\tau, \sigma, T_h/T_c)$ . It will be shown how the value of  $n$  is modified to compensate the error in neglecting the term  $\left( \frac{1}{2} \text{Erf} \left[ \frac{t - \tau + i\sigma^2\omega}{\sqrt{2}\sigma} \right] \right)$  in Eqn. 2.85.

Now including the equivalence ratio ( $\phi$ ) fluctuation and its axial dispersion with mean and standard deviation via two additional parameters  $\tau_\phi$  and  $\sigma_\phi$ , respectively, the FTF for more industrially relevant IPM operation can be obtained. But in this case  $\tau_\phi$  and  $\sigma_\phi$  do not necessarily have the same relation with  $n$  as that of  $\tau$  and  $\sigma$ . Thus it would seem more appropriate to use two separate interaction index values ( $n, n_\phi$ ). A similar analysis as for PPM case can be made but with the two additional terms representing the equivalence ratio fluctuations. We obtain:

$$f_Q(\omega) = \left( \frac{T_h}{T_c} - 1 \right)^{-1} \left( n e^{-i\omega\tau - \frac{1}{2}\omega^2\sigma^2} - n_\phi e^{-i\omega\tau_\phi - \frac{1}{2}\omega^2\sigma_\phi^2} \right). \quad (2.88)$$

However, following the work of Schuermans et al. 2004 [89] only one interaction index ( $n$ ) has proven to be fairly well representative of the flames in IPM operation and thus a similar relation as above will be used in the present investigation which is given as

$$f_Q(\omega) = n \left( \frac{T_h}{T_c} - 1 \right)^{-1} \left( e^{-i\omega\tau - \frac{1}{2}\omega^2\sigma^2} - e^{-i\omega\tau_\phi - \frac{1}{2}\omega^2\sigma_\phi^2} \right). \quad (2.89)$$

With the above relations (Eqns. 2.87 or 2.89) a closure for the heat release fluctuations in terms of acoustic variables is obtained. Thus, the FTF  $f_Q(\omega)$  model (Eqn. 2.87) can be substituted into FTM based on the R–H relations (Eqn. 2.76) to yield the acoustic relations for PPM operation as

$$\begin{pmatrix} \frac{p'}{\rho c} \\ u' \end{pmatrix}_h = \begin{pmatrix} \beta & -\beta M_c \left( \left( \frac{T_h}{T_c} - 1 \right) + n e^{-i\omega\tau - \frac{1}{2}\omega^2\sigma^2} \right) \\ -\left( \frac{T_h}{T_c} - 1 \right) \gamma M_c & 1 + n e^{-i\omega\tau - i\frac{1}{2}\omega^2\sigma^2} \end{pmatrix} \begin{pmatrix} \frac{p'}{\rho c} \\ u' \end{pmatrix}_c \quad (2.90)$$

and the FTF model (Eqn. 2.89) with the presence of equivalence ratio fluctuations can be substituted to get the acoustic relations for IPM operation as

$$\begin{pmatrix} \frac{p'}{\rho c} \\ u' \end{pmatrix}_h = \begin{pmatrix} \beta & -\beta M_c \left( \left( \frac{T_h}{T_c} - 1 \right) + n \left( e^{-i\omega\tau - i\frac{1}{2}\omega^2\sigma^2} - e^{-i\omega\tau_\phi - \frac{1}{2}\omega^2\sigma_\phi^2} \right) \right) \\ -\left( \frac{T_h}{T_c} - 1 \right) \gamma M_c & 1 + n \left( e^{-i\omega\tau - \frac{1}{2}\omega^2\sigma^2} - e^{-i\omega\tau_\phi - \frac{1}{2}\omega^2\sigma_\phi^2} \right) \end{pmatrix} \begin{pmatrix} \frac{p'}{\rho c} \\ u' \end{pmatrix}_c. \quad (2.91)$$

With the above approach the complex interaction between the flame and the acoustics can be described analytically as a function of frequency and the free flame parameters  $n$ ,  $\tau$ ,  $\sigma$ ,  $\tau_\phi$  and  $\sigma_\phi$ . In order to implement this approach, in the first place, the flame model has to be verified for its capability to represent the flame characteristics in terms of free parameters. Due to complexity these flame free parameters are generally obtained by fitting the model FTF (Eqns. 2.87 and 2.89) to the measured FTF. Also, these parameters can be obtained

by fitting them to a directly measured FTM. This has the advantage of being independent of the OH\*–chemiluminescence measurements representing the heat release fluctuations.

## 2.6 Reflection coefficient and impedance

The other important element in network modelling is the boundary element which specifies the acoustic boundary condition. This is usually done using the *reflection coefficient* or the *impedance* at the inlet and/or exit of the acoustic system considered. The acoustic *reflection coefficient*,  $R(\omega)$  is defined as the ratio between the backward travelling wave  $g(x)$  and the forward travelling wave  $f(x)$ . For the downstream ( $R_d$ ) end it is defined as:

$$R_d(\omega) = \frac{g(\omega)}{f(\omega)} \quad (2.92)$$

and similarly for the upstream ( $R_u$ ) end, it is the ratio between the forward travelling wave and the backward travelling wave

$$R_u(\omega) = \frac{f(\omega)}{g(\omega)}. \quad (2.93)$$

The reflection coefficient is a complex valued frequency dependent function. For instance, at the end of a duct of length  $L$ , when it is an open end, a pressure node appears with  $p'(L, t) = 0$  and when it is a closed end a velocity node is present with  $u'(L, t) = 0$ . Substituting these conditions in Eqns. 2.21 and 2.22, the value of the *reflection coefficient* is obtained as  $R = -1$  at open end and  $R = 1$  at closed end. In general the  $R$  values lie between -1 and 1. The particular case  $R = 0$ , represents the anechoic end where there is no reflected wave.

The *acoustic impedance* is the measure of the amount by which the motion induced by a pressure wave applied on to a surface is being impeded. Analogous to the reflection coefficient, the acoustic impedance  $Z(x, \omega)$  is defined

as the ratio of acoustic pressure to the acoustic velocity. Here the acoustic velocity is taken normal to the surface pointing outwards of the volume under consideration:

$$Z(x, \omega) = \frac{p'(x, \omega)}{\bar{\rho} c u'(x, \omega)}. \quad (2.94)$$

Now using the Eqns. 2.92 and 2.94 we get the acoustic impedance expressed in terms of the reflection coefficient for the downstream end as follows:

$$Z(x, \omega) = \frac{f + g}{f - g} = \frac{1 + R_d}{1 - R_d}. \quad (2.95)$$

It is very difficult to measure the acoustic velocity particularly in the presence of flame and high background noise. Therefore, it is derived from the measured acoustic pressure field (e.g. multi microphone method). It is very important to have a low reflecting boundary condition towards the combustor exit. It is in order to avoid pure standing waves. If enough acoustic loss is provided ( $|R| \ll 1$ ) the phase information from the measured pressures can also be used effectively to determine the acoustic velocity. The importance of the reflection coefficient will be more obvious from the results and discussion in chapter 4.

Having defined relevant acoustic elements it will be now convenient to describe how these elements are interconnected leading to a low order network model. This is also useful to know actually how the acoustic information propagating within the system can be extracted at any chosen location, thus simulating an experiment, as discussed in the following section.

## 2.7 Low order network model

Complex thermo-acoustic systems such as in gas turbines can be represented by network models consisting of individual elements like supply duct, bur-

ner, flame, choked exit etc.. Each of these elements is characterized acoustically by determining the acoustic variables such as pressure and velocity up and downstream of the element. As mentioned previously the acoustic pressure and density perturbations are treated as small compared with their mean quantities. These acoustic variables are coupled across each element using linearized acoustic equations. The pressure field is treated as harmonic with respect to time and it is represented by means of forward and backward traveling waves in terms of "Riemann invariants"  $f$  and  $g$ , respectively. These variables are linked across each element with their respective transfer matrices. For example the transfer matrix of an element as function of frequency  $\omega$  in terms of  $f$  and  $g$ s can be represented as

$$\begin{pmatrix} f \\ g \end{pmatrix}_d = \underbrace{\begin{pmatrix} T_{11} & T_{12} \\ T_{21} & T_{22} \end{pmatrix}}_{\text{TM}(\omega)} \begin{pmatrix} f \\ g \end{pmatrix}_u \quad (2.96)$$

where the subscripts  $u, d$  represent the up- and downstream end of the element.

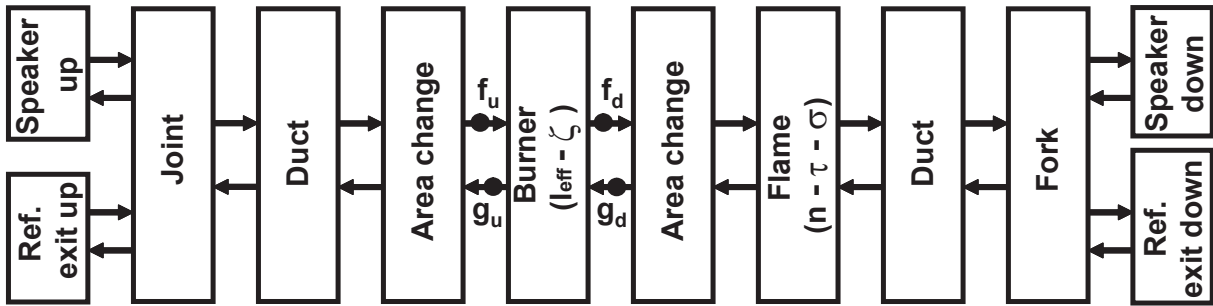


**Figure 2.3:** 1-D acoustic network model representing the single burner test rig (chapter 3)

The schematic of the 1-D low order network model for the single burner test rig is shown in Fig. 2.3. The elements duct, burner, flame and area change represent the connecting elements while the speaker and reflecting ends represent the boundary conditions. The burner and flame are treated as compact elements as discussed in previous sections with the free parameters  $l_{eff}-\zeta$  and  $n-\tau-\sigma$ , respectively. The network model consists of speakers placed up- and

downstream for acoustic excitation along with respective measured reflective boundary conditions. In order to represent the flow field appropriately a joint and fork element (nodes) are implemented to form a junction between the reflecting ends, the speakers and the ducts. The plenum and combustion chamber are modeled as simple ducts. The acoustic response in terms of  $f$  and  $g$ s or in terms of  $p'$  and  $u'$  can be obtained at selected “nodes” within the system (shown as dark points of the burner element in Fig. 2.3). Each element is represented by two ports, one upstream and the other downstream with four unknown variables, i.e.  $(f, g)_u$  and  $(f, g)_d$ . Therefore, the total number of unknowns of the system with  $N$  connecting nodes will be equal to  $4N$ . A system of equations can be obtained, which can be generally represented in matrix notation for  $M$  elements (for more details see Polifke et al. 1997 [73]) as follows:

$$\begin{pmatrix} \text{Coefficient} \\ \\ \text{matrix with} \\ \\ (\text{M} \times \text{N}) \text{ elements} \end{pmatrix} \begin{pmatrix} f_i \\ g_i \\ \vdots \\ f_N \\ g_N \end{pmatrix} = \begin{pmatrix} v_i \\ \vdots \\ v_M \end{pmatrix}. \quad (2.97)$$

The coefficient matrix on left side of the Eqn. 2.97 is known as the *system matrix* and can be formulated in terms of geometric and physical parameters (length  $l$ , density  $\rho$ , speed of sound  $c$ , burner and flame parameters  $l_{eff}-\zeta$  and  $n - \tau - \sigma$ ). The vector on the right side of Eqn. 2.97 known as *system vector*, contains few non zero values (inhomogeneous system with excitation) or only zeros (homogeneous system). For an inhomogeneous system, the characteristic equation can be solved directly for the unknown variables  $f$  and  $g$  whenever the determinant of the *system matrix* is non zero. For a homogeneous system, the solution of the characteristic equation  $Det|A| = 0$  delivers the eigenfrequencies  $\omega_m$  for the modes  $m$ .

In this work the thermoacoustic network tool  $ta^2$  package written in Mathematica has been used to generate the system matrix and to solve for the unknowns  $f_i$  and  $g_i$  at any chosen location (nodes). The input arguments like the geometric details and flow parameters are to be given by the user. The output

can be visualized as e.g. acoustic pressure spectrum or can be saved into a data file according to the user choice. As discussed previously, the influence of damping on the wave propagation (see section 2.2.2) can be simulated by implementing damped ducts in the network model. Here the isentropic ducts can be replaced by damped ducts using the additional input according to Eqn. 2.38. A large influence of damping can be observed in the presence of combustion, an effect that is discussed in chapter 4.

## 3 Test Rig and Measurement Techniques

### 3.1 Single burner test rig

The experimental investigation was performed on a single burner atmospheric test rig as shown schematically in Fig. 3.1. The test rig was originally designed for investigating a self-excited combustion instability known as "Rumble" which is usually observed in the aero-engines [18, 19]. The test facility mainly consists of an air and a fuel supply unit, an acoustic excitation unit, the burner and combustion chamber and finally the exhaust unit with flexible acoustic boundary condition. A detailed description of the test rig along with its components is presented by Eckstein, 2004 [18]. Here only the essential components/units, which are key to the present investigation, will be discussed.

**Air and fuel supply unit:** The compressed air is taken from a reservoir at 12 bar for both combustion and cooling purposes. The air for combustion is fil-

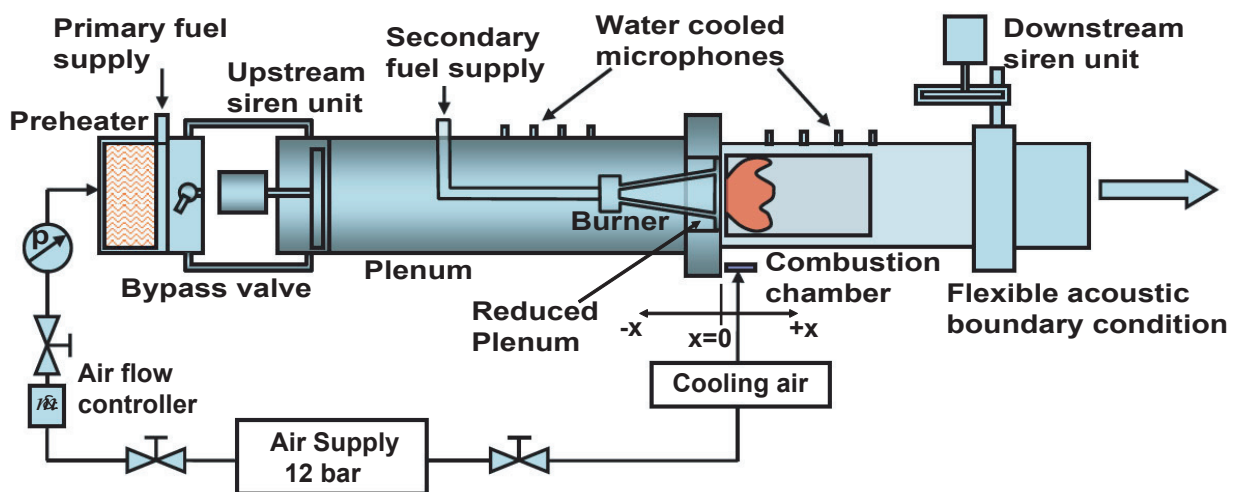


Figure 3.1: Schematic of the single burner test rig

tered and passed through a thermal mass flow controller<sup>1</sup> providing the desired air mass flow rate. The cooling air is directly taken from the reservoir to cool the hot components combustion chamber, siren unit etc.. As the present investigation is focused on the gas turbine application, an electrical preheater (32 kW) is used for preheating the air up to 500°C which is close to the compressor exit conditions. The fuel used for this investigation is natural gas with 98.04 Mol.% methane. Two gas flow meters were installed for monitoring the fuel flow rate in PPM<sup>2</sup> and IPM<sup>3</sup> operation independently. In PPM operation the fuel is injected into the main air stream using small venturi nozzles positioned far upstream of the combustor. For the more industrial relevant IPM operation, the fuel is being injected directly inside the burner unit. An operating range up to 100 kW of thermal power can be achieved with the present configuration.

**Acoustic excitation unit:** For acoustic excitation of the flow field, speed controlled sirens are placed up- and downstream of the burner to provide two source location forcing. The siren unit consists of a combination of rotor-stator discs with fixed number of holes (6) equally distributed on each of them as shown in Fig. 3.2.

The shapes of the holes are made such that a sinusoidal excitation (wave form) is generated with sufficient amplitude and large signal to noise ratio. This is, in particular, a pre-requisite for implementing the multi microphone technique which is discussed in the following sections. The velocity of the siren shaft mounted with rotating disc determines the frequency of excitation. As the upstream siren directly modulates the fresh gas mixture, a bypass valve placed upstream of the siren is used to control the level of acoustic excitation. The valve and the siren are connected by four flexible steel hoses, which also provide an acoustic decoupling of air and the primary fuel supply unit. As the siren is operated with preheated air, ball bearings holding the siren shaft are located outside the hot siren chamber and are air cooled internally as shown in Fig. 3.2. The siren shaft is rotated by means of a AC motor<sup>4</sup> and the rota-

---

<sup>1</sup>Type Bronkhorst F206BI-FBD-99V, max. air flow rate 150 g/s

<sup>2</sup>PPM fuel flow meter: Type Bronkhorst F-202AC-AAB-44V, max. gas flow rate 190 l/min (CH<sub>4</sub>)

<sup>3</sup>IPM fuel flow meter: Type Bronkhorst F-113C-HB-00V, max. gas flow rate 5 g/s (CH<sub>4</sub>)

<sup>4</sup>Type KIMO Motor Master MM215-EMC, nominal torque 3.7 Nm

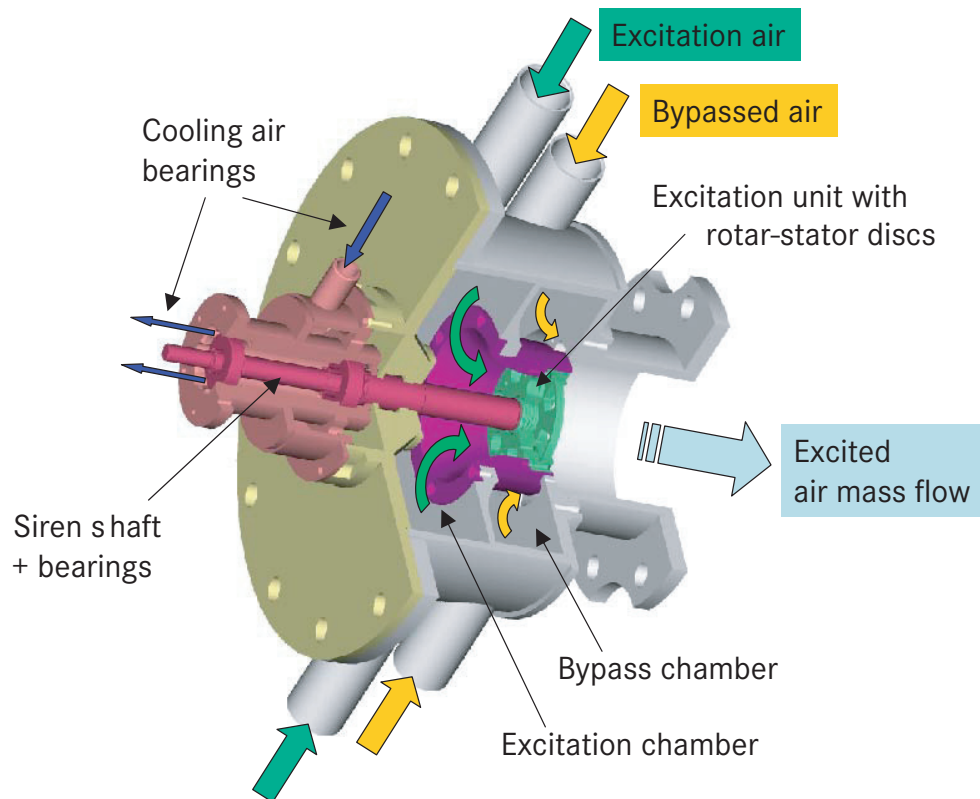


**Figure 3.2:** Assembly drawing of the siren unit (courtesy Eckstein, 2004 [18])

tional speed is controlled by a frequency converter to provide stable frequencies ( $f_{ref}$ ) of excitation up to 800 Hz. A reference signal is generated using a profiled disc, being mounted on the siren shaft, and a photo sensor. The reference signal is used for phase resolved measurements and also to evaluate the Fast Fourier Transformed (FFT) vectors of all dynamic signals at the frequency of excitation  $f_{ref}$ .

**Plenum and burner unit:** A thermally insulated and segmented plenum pipe with diameter 124 mm and 1300 mm length is used as acoustic resonator for higher excitation amplitudes and it provides a homogeneous flow field. The siren unit is mounted on one end of the plenum and the burner unit is mounted on the other end (reduced plenum). In order to achieve a pure 1-D axial acoustic field without transverse modes, the diameter of the duct has been chosen as suggested by Munjal, 1987 [53]. An influence of higher order

modes usually occur beyond a specific cut-off frequency ( $f_{co}$ ). For the given geometry it can be calculated as:

$$f_{co} = \frac{1.84 c}{\pi d} \quad (3.1)$$

with  $d$  the diameter of the duct and  $c$  the speed of sound. In the present investigation with preheated air up to 300°C ( $c \approx 480 \text{ m/s}$ ) the cut-off frequency is about 2200 Hz, well beyond the highest frequencies of interest ( $< 800 \text{ Hz}$ ). Although the plenum is designed for variable length (850 to 1450 mm) with different segments [18], only the standard configuration (1300 mm) has been used for the present investigation with the first resonance mode around 185 Hz (with 300°C preheating). The plenum is provided with several ports to accommodate the dynamic pressure transducers and also the thermocouples to measure the mean temperature inside the plenum.

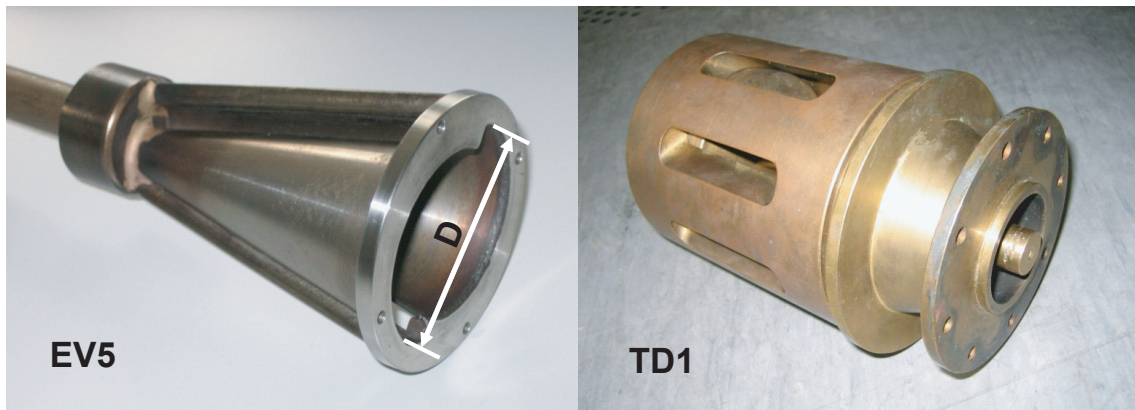


**Figure 3.3:** Pictures of the EV5 and TD1 burner used in the present study

The test rig was designed to investigate different types of burners with very easy adaptability. The burners which are of particular interest for this study are the EV5<sup>5</sup> and TD1<sup>6</sup> burners as shown in Fig. 3.3. The EV5 burner [82] consists of two slightly shifted cones providing slots to allow and generate swirl for the air fuel mixture and has a nominal burner exit diameter ( $D$ ) of 50 mm as indicated in Fig. 3.3. Optionally, the entire fuel can be injected through the nozzles provided along the slots in IPM operation.

<sup>5</sup>EV5: A scaled down model of the Environmental Burner for low emission from Alstom, Switzerland

<sup>6</sup>TD1: A generic swirl stabilized burner developed at Lehrstuhl für Thermodynamik, TU-München

### 3.1 Single burner test rig

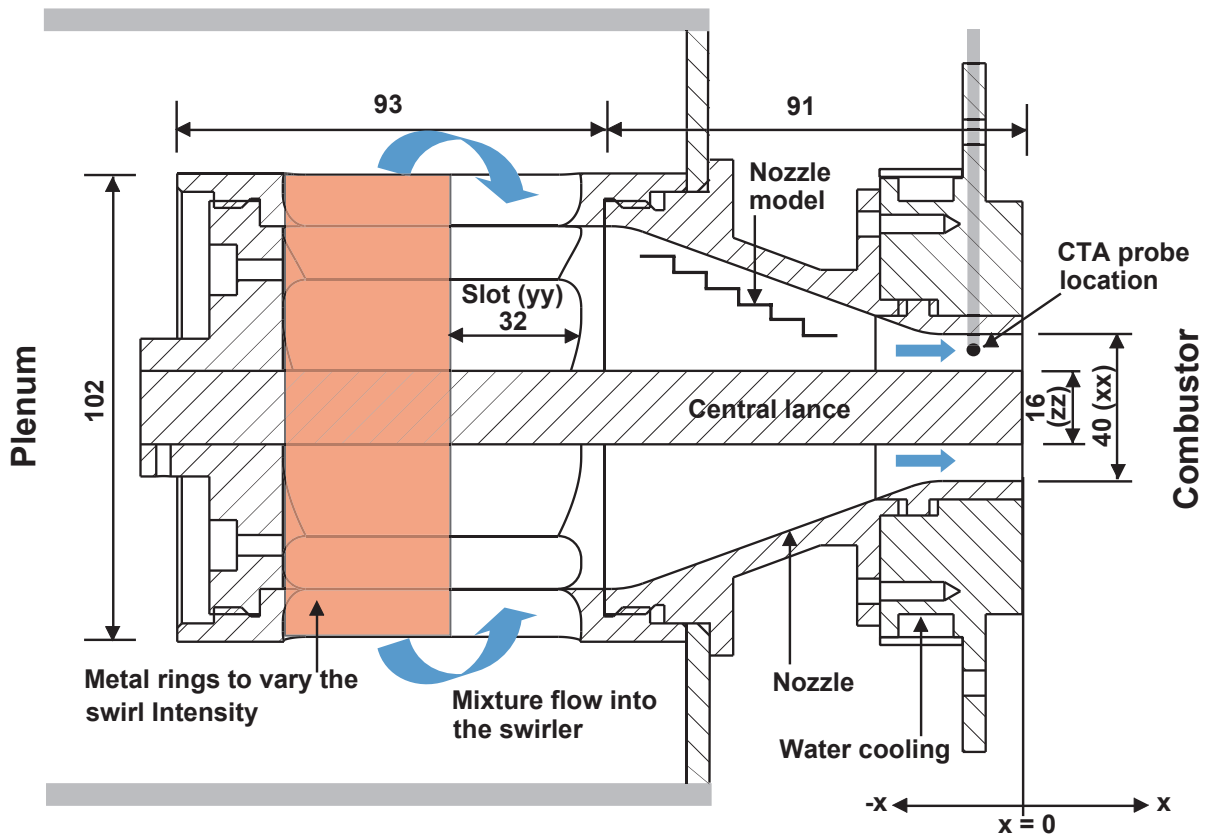


**Figure 3.4:** Schematic of the TD1 burner with geometric details. CTA probe location is about 10 mm upstream of the burner exit plane. For acoustic network modelling the nozzle is represented as a sequence of duct–area change–duct elements.

In the TD1 burner the flow enters radially through the slots providing the desired swirl as shown in Fig. 3.4 [22]. The intensity of the swirl can be selected by changing the amount of blockage using metal rings. The swirling flow is then accelerated in the nozzle before exiting into the combustion chamber. The geometric configuration is encoded as “xxyyzz”. i.e. a configuration with 40 mm nozzle exit diameter, 32 mm swirl slot length and 16 mm lance diameter will be represented as 403216. The CTA probe was located about 10 mm upstream of the burner exit plane as shown in the figure. This position was considered to be the optimum location for measuring the acoustic velocity close to the burner exit plane and it also avoids damage to the probe in the presence of combustion. The TD1 burner can also be operated in piloted mode with pilot

fuel (from the IPM fuel flow meter) being injected at the tip of the lance. The additional details in the figure are useful for modelling this burner and will be discussed in chapter 4.

**Combustor and exhaust unit:** The combustor unit consists of a 90 mm square combustion chamber of 300 mm length, which is air and water cooled. Its cross section is comparable to the dimensions of a single sector of the annular combustion chamber used in a parallel study [20, 43]. Quartz glass windows (air cooled) on two opposite sides provide optical access. The other two side walls are water cooled and provide igniter (bottom) and microphone ports. Optionally, the combustor walls can be interchanged to provide an additional laser sheet accessibility, such as for PIV measurements. An air cooled combustion chamber extension with the same cross sectional area was used in particular for dynamic pressure measurements in the presence of the flame. By placing the pressure sensors partly in the combustor extension the large axial temperature gradients associated with the flame are avoided. Both, the combustor and the extended combustion chamber were equipped with several equidistant microphone ports.

The downstream siren port is placed between combustor extension and the combustor exit. A low reflection or even anechoic boundary condition is desirable for making precise acoustic measurements. For this purpose a perforated end plate has been designed. The design rules were obtained using the linearized continuity and momentum equations (Eqns. 2.53 and 2.61). Consider an area change across the combustor exit as shown in Fig. 3.5.

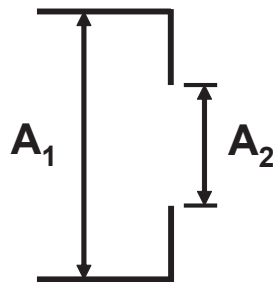


**Figure 3.5:** Area change across the combustor exit

Now applying the simplified continuity and Bernoulli equations across the area change after neglecting the effective length  $l_{eff}$  we get:

$$\bar{u}_1 A_1 = \bar{u}_2 A_2 \quad (3.2)$$

$$u'_1 A_1 = u'_2 A_2 \quad (3.3)$$

$$\frac{p'_1}{\rho c} + M_1 u'_1 = \frac{p'_2}{\rho c} + M_2 u'_2. \quad (3.4)$$

At location 2, with  $p'_2 = 0$ , the Eqn. 3.4 becomes:

$$\frac{p'_1}{\rho c} = M_2 u'_2 - M_1 u'_1 \quad (3.5)$$

$$\frac{p'_1}{\rho c} = M_1 u'_1 \left( \left( \frac{A_1}{A_2} \right)^2 - 1 \right). \quad (3.6)$$

Using the relations for acoustic impedance (Eqns. 2.94 and 2.95) together with Eqn. 3.6 yields

$$Z = \frac{p'_1}{\rho c u'_1} = \frac{1 + R_d}{1 - R_d} = M_1 \left( \left( \frac{A_1}{A_2} \right)^2 - 1 \right) \quad (3.7)$$

$$1 + R_d = M_1 \left( \left( \frac{A_1}{A_2} \right)^2 - 1 \right) (1 - R_d). \quad (3.8)$$

For an anechoic end, the value of the reflection coefficient is zero. Substituting  $R_d = 0$  in Eqn. 3.8 we get

$$\sqrt{\left( \frac{1}{M_1} + 1 \right)} = \frac{A_1}{A_2}. \quad (3.9)$$

For low Mach number approximation,  $M \ll 1$ ,  $\sqrt{\left( \frac{1}{M_1} + 1 \right)} = \sqrt{\frac{1}{M_1}}$  and the Eqn. 3.9 reads as

$$\frac{A_2}{A_1} = \sqrt{M_1}. \quad (3.10)$$

The above analysis are applicable only if the downward travelling wave originating from the orifice ( $A_2$ ) propagates into the “environment” and is not reflected back ( $p'_2 = 0$ ). But, in reality we use a confinement such as exhaust chamber downstream of the disk that bears the risk of recovering the 1-D acoustic wave field again. So, in this situation the relation derived above (Eqn. 3.10) may not be valid for attaining an **anechoic** end and some other relations would be required. Nevertheless, an attempt has been made to use the above analysis to attain a **low** reflecting boundary condition in the present setup. With preheated air upto 300°C and in presence of the flame the exit area was calculated (using Eqn. 3.10) to be six holes of diameter 15 mm each. The same end plate has been used for all cold and hot measurements. The amplitude and phase values of the measured reflection coefficient with and without flame using the perforated plate at the end of the combustor are shown in Fig. 3.6.

In the very low frequency limit the amplitude values are measured to be around one and phase values of  $-\pi$ . This indicates that in the low frequency limit the orifice acts as an open end boundary condition. With increase in frequency the amplitude values, in both cases, initially drops almost to a value of zero and then gradually increase to a value of 0.6. But, with increase in frequency the phase values converges to zero in the case of without flame and a small drop in phase is observed in the case with flame. As the measurements indicate a low but frequency dependent reflection coefficient this data was used directly in the network model to represent the suitable boundary condition as a function of frequency (chapter 4). As pointed out earlier, these results also reveal that an anechoic end cannot be achieved in practice.

**Microphones and calibration unit:** Up to four water cooled pre-amplified condenser microphones<sup>7</sup> which have a large dynamic range and frequency response are mounted both up- and downstream of the burner. A microphone along with its water cooling jacket is shown in Fig. 3.7.

The maximum operating temperatures of the microphone and preamplifier are 150°C and 70°C, respectively. For this reason a thermostat controlled water cooling unit is used for cooling the microphones (up to 10 microphones) at

---

<sup>7</sup>Type G.R.A.S 40BP - 1/4- inch with preamplifier type 26AL 1/4 - inch

### 3.1 Single burner test rig

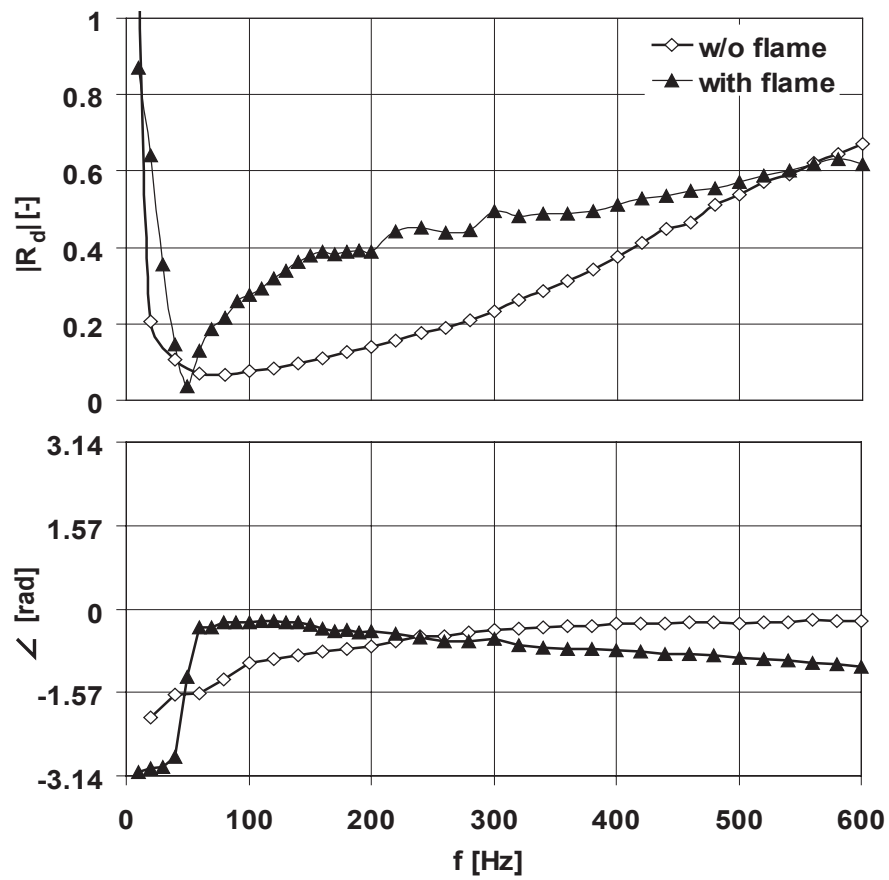


**Figure 3.6:** Amplitude and phase values of the measured reflection coefficient using the perforated plate at the exit of the combustor

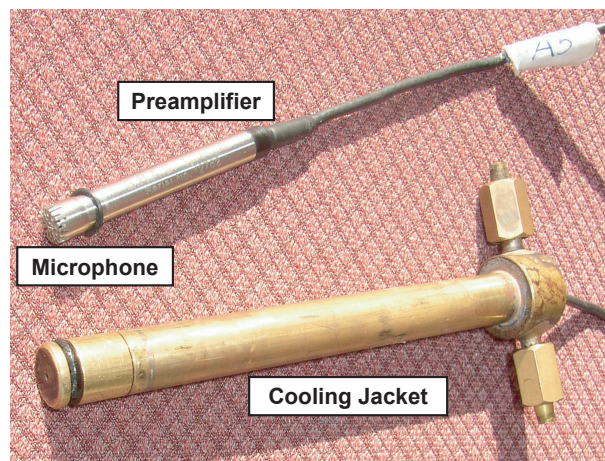


**Figure 3.7:** 1/4" Condenser microphone and cooling jacket

65°C. This is a compromise temperature, as excessive cooling may lead to condensation of the water vapor present in the combustion gases on the membrane of the microphones mounted in the combustion chamber [43].

The absolute calibration of the individual microphone has been made using a pistonphone<sup>8</sup>, where as calibration of all microphones with respect to a reference microphone was made using the calibration tube as shown in Fig. 3.8. This is quite important to minimize the relative amplitude and phase errors between the microphones. The inner diameter of the calibration tube is 25 mm and it has a length of about 200 mm. The calibration is performed by speaker excitation controlled by a signal generator<sup>9</sup>. The microphones were connected to a four channel signal conditioning amplifier<sup>10</sup>. The amplification factor has been varied from 1mV/Pa to 10 mV/Pa, depending on various operating conditions.

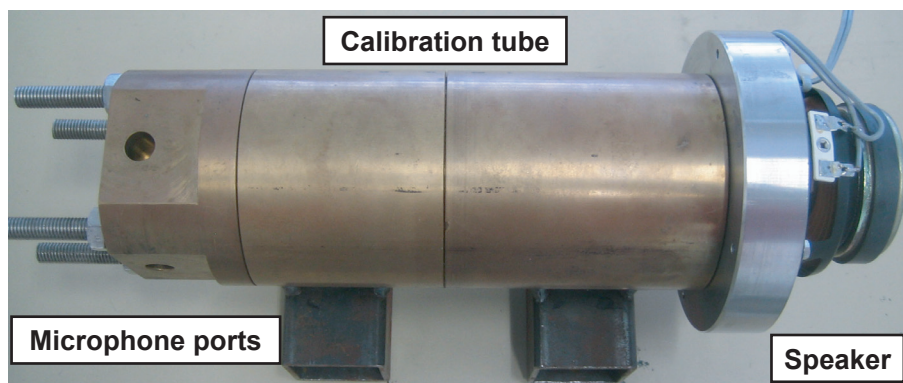


**Figure 3.8:** *Microphone calibration unit*

The static and dynamic signals from various sensors mounted on the test rig are measured using a sample and hold data acquisition system with a multichannel-I/O Board<sup>11</sup> at a sampling rate of 10 kHz. Usually 10000 samples were made per each measurement loop. The data acquisition procedure is controlled using the commercial software package *LabView*. A similar measurement procedure and on-line post processing as outlined by Eckstein, 2004 [18] has been implemented. To measure the static pressure drop across the

<sup>8</sup>Type G.R.A.S 42 AA

<sup>9</sup>Type Agilent 33220A LXI

<sup>10</sup>Type Nexus 2692C by Brüel & Kjær

<sup>11</sup>Type Meilhaus ME-2600i PCI, 333 kHz and 12 Bit

burner a differential pressure gauge has been mounted on the test rig connecting two ports just upstream (inside the plenum) and downstream of the burner (in the combustion chamber). This is in particular, important to calculate the static pressure loss coefficient which is used to cross check the loss coefficient obtained from the burner models (more in chapter 4).

## 3.2 Measurement techniques

In this section the measurement techniques will be explained in detail. Also the advantages and limitations of each procedure will be discussed in parallel, with respect to their application to the annular test rig, which is the main motivation to investigate alternative methods [2, 21].

### 3.2.1 Direct acoustic transfer matrix measurement

In order to acoustically characterize an element like a burner, duct etc. its response (output, on downstream side) to a given acoustic perturbation (input, on upstream side) and vice versa has to be known. This is done by determining the transfer matrix of an element which links the acoustic variables pressure and velocity linearly across the element. Because the 1-D acoustic field is described generally by two state variables, i.e. the acoustic pressure and velocity, the acoustic element can be represented by a  $2 \times 2$  transfer matrix. The mathematical description of transfer matrix is given by Eqn. 2.96, which is repeated here

$$\begin{pmatrix} \frac{p'}{\rho c} \\ u' \end{pmatrix}_d = \underbrace{\begin{pmatrix} T_{11} & T_{12} \\ T_{21} & T_{22} \end{pmatrix}}_{TM(\omega)} \begin{pmatrix} \frac{p'}{\rho c} \\ u' \end{pmatrix}_u. \quad (3.11)$$

To calculate the four elements of the transfer matrix, four equations are needed. For a given excitation of the system, Eqn. 3.11 provides only two equations. Therefore, the acoustic variables on both sides of the element must be

determined in two different experiments at the same frequency. The experimental and theoretical determination of acoustic transfer matrices are presented by Abom (1992), Munjal and Dodgie (1990) [1,54]. Following their work, the transfer matrix can be determined experimentally from Eqn. 3.12 as

$$\begin{pmatrix} \frac{p'_a}{\rho c} \\ u'_a \\ \frac{p'_b}{\rho c} \\ u'_b \end{pmatrix}_d = \begin{pmatrix} \frac{p'_a}{\rho c} & u'_a & 0 & 0 \\ 0 & 0 & \frac{p'_a}{\rho c} & u'_a \\ \frac{p'_b}{\rho c} & u'_b & 0 & 0 \\ 0 & 0 & \frac{p'_b}{\rho c} & u'_b \end{pmatrix}_u \cdot \begin{pmatrix} T_{11} \\ T_{12} \\ T_{21} \\ T_{22} \end{pmatrix}. \quad (3.12)$$

The two independent test states are achieved by measuring first the response of the acoustic system to an excitation by the upstream siren (index "a") and then by a downstream siren (index "b"). To solve the above equation the pressure and velocity upstream and downstream of the element has to be measured. As it is almost impossible to measure the acoustic velocity in a high temperature turbulent flow field with reasonable effort and accuracy, a different method is needed which is based only on the measured acoustic pressures.

**Multi microphone method:** It is known from the 1-D acoustic wave propagation how the wave propagates through ducts (Eqn.2.35). Therefore, both the acoustic pressure and velocity can be calculated just upstream and downstream of the acoustic element by measuring only the pressure. In principle, the acoustic perturbations can be obtained at any position by only two microphones placed on either side of the element [1, 54]. But, to minimize the impact of errors induced due to turbulent flow noise, methods were developed that incorporate a higher number of microphones on each side of the test element. This procedure is known as *Multi Microphone Method*, MMM. More details of this method are presented in the literature [22,23,60,63,79,87]. As more than two microphones are used (up to four microphones) on either side the system is over determined. For that reason, the MMM implements a nonlinear least square fit<sup>12</sup> of the measured pressures ( $p'_k$ ) at multiple microphone positions ( $x_k$ ) to evaluate the complex amplitude and phase of the

<sup>12</sup>Levenberg-Marquardt algorithm has been implemented

plane waves traveling up ( $g$ ) and downstream ( $f$ ) along the measurement locations according to

$$\sum_{k=1}^N [ |p'_k| - \bar{\rho}c (f \cdot e^{-ik_+x_k} + g \cdot e^{ik_-x_k}) ]^2 \rightarrow \min. \quad (3.13)$$

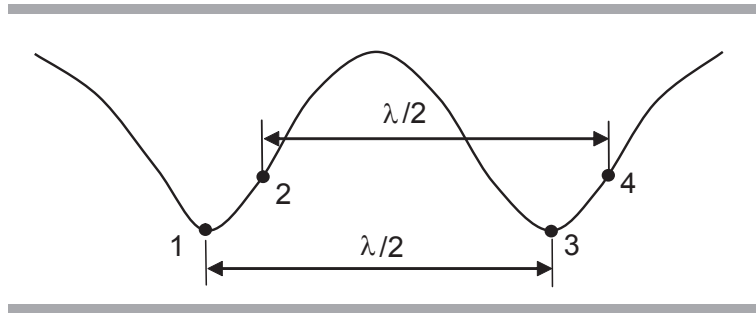


**Figure 3.9:** Schematic of the wave field in a simple duct showing the singularity effect due to microphone positioning at a distances equal to multiple of half a wavelength  $\lambda/2$

The microphone positions must be chosen non equidistant to avoid the effect of singularities which occur when the distance between the microphones approaches the multiple of half a wavelength [23]. Consider an acoustic pressure field measured by 4 microphones as shown in Fig. 3.9. If the microphones are placed such that the distance between the microphone pairs (1,3) and (2,4) becomes half of the wave length as shown in Fig. 3.9 the system becomes singular, as there is no additional information in using either pair to reconstruct the wave field. For e.g. 600 Hz on combustor side with a temperature of the flow field around 1500 K, the value of the half wave length will be  $\lambda/2 = 650$  mm. But this will not cause singularity problem as all the microphones are placed within the distance of 600 mm (length of the combustor is 700mm). However, on the plenum side with a temperature of the flow field around 500 K and at 600 Hz the value of the  $\lambda/2 = 370$  mm, may cause a singularity problem as the microphones can be placed in this domain (plenum length 1300mm). In particular, for the low frequency limit ( $< 60$  Hz) significant improvements were observed in amplitude and phase values during the reconstruction of the wave field by selecting the microphones with large distances between them.

An important issue with data acquisition using microphones is that they measure the response to the excitation from the siren along with a considerable amount of back ground noise from turbulence. To minimize these stochastic contributions stemming from other sources than the siren excitation a pure tone method is implemented [22, 87]. Here the Fast Fourier Transform (FFT) of the signals are evaluated exactly at the discrete forcing frequency  $f_{ref}$

$$\hat{p}(f_{ref}) = \frac{2}{N} \sum_{n=1}^N p_n \cdot e^{\frac{i2\pi f_{ref}n}{N}} \quad (3.14)$$

where  $N$  is the number of samples. Hence, the amplitude and phase response corresponding only to acoustic forcing from the siren ( $f_{ref}$ ) are determined from the Fourier transform using a Hanning window for each microphone signal. Only these transformed data are stored separately without any further post processing to reduce the volume of raw data and as well the time needed for processing them at a later stage. Over one period of the cycle all the measured pressure vectors at their respective microphone locations revolve around the origin of the complex plane. All these pressure vectors  $p'_i$  are rotated by the negative phase angle ( $-\phi_{ref}$ ) of the siren reference signal ( $U'_{ref}$ ) as shown in Fig. 3.10.

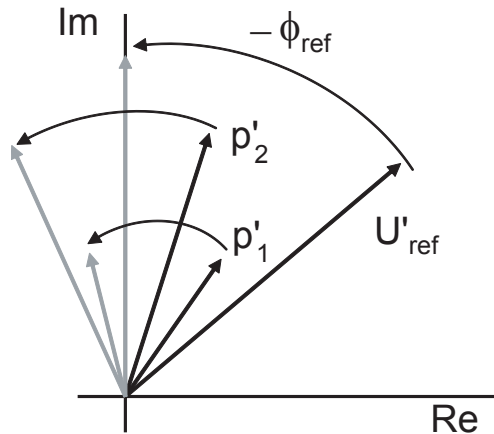


**Figure 3.10:** *Averaging of multiple measurements. The microphone pressures  $p'_i$  are rotated by the negative phase angle  $-\phi_{ref}$  of the reference signal (reproduced from Fischer et al. 2006 [23])*

Next, the rotated pressure vectors are averaged for each frequency. For this in-

investigation the frequency range from 20 to 600 Hz was covered in steps of 20 Hz. Depending on the frequency, 15 (> 200 Hz) to 25 (< 200 Hz) time series of one second duration each of all signals were recorded with a sampling frequency of 10 kHz. With the two independent data sets obtained the transfer matrix of a chosen element (e.g. burner) as the function of frequency can be evaluated using Eqn. 3.12. The direct measurement of transfer matrices needs precise measurements of the acoustic variables in a rather hostile environment. Besides large calibration effort, it requires at least two source forcing with sufficient authority which may be difficult to provide in e.g. a high pressure test rig. In spite of this limitation, the method is well established and often applicable in the single burner atmospheric test rigs with 1-D acoustic field. However, in the case of more complex acoustics, like in an annular test rig, an exponential growth of the number of sensors ( $\approx 30$ ) required to resolve the acoustical modes restricts the use of this method [20]. For this reason alternative methods are required in such cases.

**Determination of the flame transfer matrix (FTM):** A similar procedure, as explained above can be applied to evaluate the FTM. The transfer matrix of the burner (BTM) and burner together with flame (BFTM) are obtained separately. Using the inverse matrix multiplication the desired FTM can be obtained as

$$FTM = BFTM \cdot BTM^{-1}. \quad (3.15)$$

Here, the basic assumption is made that the BTM remains constant even in the presence of flame. This assumption is justified in the present work (more in chapter 4) and is also in agreement with previous work [87].

### 3.2.2 Constant temperature anemometer

If an essentially 1-D flow field can be assumed, a hot wire anemometer is a simple conventional method to measure the velocity fluctuations from the mass flow fluctuations. In this work a constant temperature anemometer CTA<sup>13</sup> with a 10  $\mu m$  Pt-Ir hot wire has been used to measure the time re-

---

<sup>13</sup>Type DISA 55D01

solved velocity fluctuations just upstream of the burner exit plane. The hot wire probe heated by electrical current is connected as a Wheatstone bridge. During operation, the resistance of the probe decreases due to convective cooling and a servo amplifier applies a proportional voltage to increase the resistance thus balancing the bridge. The bridge voltage  $V$  is correlated non-linearly with the continuously changing fluid velocity (convective heat transfer). The calibration coefficients ( $C_i$ ) are obtained by making a polynomial fit of the measured voltage to the mean flow velocity (mass flow rate) as follows:

$$u = C_0 + C_1 \cdot V + C_2 \cdot V^2 + C_3 \cdot V^3 + C_4 \cdot V^4. \quad (3.16)$$

Thus the local velocity at a given probe location can be obtained by interpolating at the measured voltage. The CTA has been calibrated before every measurement. During the ignition in the test rig, the CTA is pulled out partially to avoid the damage of the fragile hot-wire in case of a flashback. This procedure becomes very critical if the flow field inside complex geometries like EV5 burner is investigated with air preheating. Due to high pressure and velocity gradients inside the slots, the response of the CTA probe was very sensitive to its exact positioning in the flow field. Therefore the reproducibility and hence reliability of the measurement was very poor. However, in the case of TD1 burner with relatively simple exit geometry the CTA has been applied successfully.

A detailed analysis of the acoustic flow field inside the EV5 burner was carried out by using an Acoustic *Finite Element Method*, FEM model<sup>14</sup> (the details of this model are presented in the Appendix). The results have shown (next chapter) clearly the significant pressure and velocity gradients at the entrance of the slots as expected. This has indicated that the application of the CTA method in complex geometry like EV5 is not suitable, albeit applicable for relatively simple exit geometries like in the TD1 burner.

---

<sup>14</sup>From Commercial software package, COMSOL Multi Physics Inc.

### 3.2.3 OH\*–chemiluminescence

It has become a standard practice in the field of thermoacoustics to assume that the heat release rate of PPM flames is proportional to the OH\*–Chemiluminescence emitted from the flame [31, 33, 39, 44]. Haber et al. 2000 [31] have made an experimental investigation on the relationship between the light emissions and heat release rate under non adiabatic conditions. They found that the OH\*–Chemiluminescence is a better indicator of heat–release rate than the CH\*–chemiluminescence. Still the absolute value of the heat release rate cannot be obtained from this method. However the assumption that the OH\*–chemiluminescence is linearly dependent on the heat release rate seems justified. This is also supported by work of Price et al. [74].

In the present study the heat release fluctuations are measured via the OH\*–chemiluminescence emitted from the flame using an UV filtered photomultiplier. A UV–filter<sup>15</sup> was mounted to detect the OH\*–chemiluminescence which peaks at a wavelength of 308 nm. The photomultiplier was positioned 100 mm downstream of the burner exit and perpendicular to the optical window at a radial distance of 200 mm which was sufficient to view the entire flame zone. The calibration of the photomultiplier is performed by measuring the photomultiplier intensity ( $I$  in volts) at several static operating points of varying thermal power with a constant air excess ratio  $\lambda$ . Using this procedure a calibration curve can be obtained between the the mean heat release rate ( $\bar{Q}$ ) and the photomultiplier intensity ( $\bar{I}$ ), which can be used later to correlate the dynamic heat release rate with the measured photomultiplier intensity in relative terms, according to

$$\frac{\dot{Q}'}{\bar{Q}} \approx \frac{I'}{\bar{I}}. \quad (3.17)$$

For optical characterization of the flame, i.e. flame structure and flame length, a high speed intensified CCD camera<sup>16</sup> has been used. An UV lens<sup>17</sup> (105 mm

---

<sup>15</sup>Type DUG11, 50 × 50 mm, supplier: SCHOTT AG

<sup>16</sup>Type APX intensified camera

<sup>17</sup>Nikon Inc.

and 1.4 aperture) has been mounted along with the same interference filter as mentioned above. A sequence of five hundred images with a resolution of  $1024 \times 512$  px are taken to get an ensemble averaged image that is used to characterize each static operating point.

### 3.2.4 Particle image velocimetry

PIV is an optical non-intrusive technique to effectively measure the velocity field in flows. The principle of PIV along with some applications are given by Raffel et al, 1998 [75] and Stella et al. [95]. For PIV the flow is seeded with tracer particles. It is then illuminated in a plane of the flow field at least twice within a short interval of time. The light scattered by the particles is recorded on a single frame or a sequence of frames. Using these frames the displacement of the particle images between the light pulses is determined. The digital PIV data evaluation uses small interrogation areas, in which the displacement vector of tracer particles between the first and second illumination is determined by means of statistical methods (auto or cross correlation - using a FFT algorithm). Given the displacement the velocity vector is calculated taking into account the time delay between the two illuminations and magnification factor of the imaging system.

In the present investigation the PIV measurements were made to obtain the flow field in the single burner combustor and an annular combustor. These measurements revealed substantial differences of the flow field in both cases and explained the differences observed in the dynamic flame parameters between the two test rig configurations [21].

A picture of the PIV set up in the single burner combustor is shown in Fig. 3.11. The flow direction is from left to right. Two side plates are provided with extended slits that allow the light sheet to pass through the combustion chamber. Placing the windows at the slit ends minimizes scatter and reflections. The measurements are made in the meridional plane of the EV5 burner covering a region of  $100 \times 80$  mm.  $TiO_2$  particles with an average diameter of 5–10

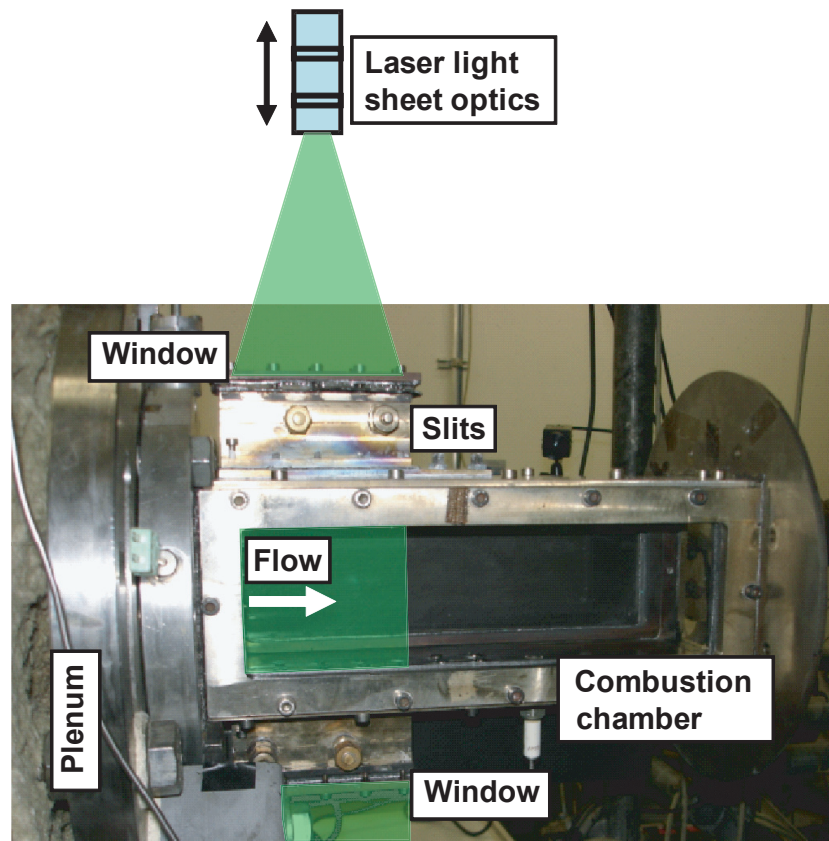


**Figure 3.11:** *The PIV set up for single burner combustor*

$\mu\text{m}$  are used as seeding. The high speed two component PIV system<sup>18</sup> used in the present study consists of a double pulsed Nd–YAG laser system with a repetition rate of 1 kHz. The laser is synchronized with a high speed camera equipped with a 85 mm lens and an interference filter of  $532\text{ nm} \pm 20\text{ nm}$ . The camera is placed perpendicular to the laser light sheet plane (not shown). The images were taken at a sampling rate of 2 kHz, to get 1 kHz pairs of images with a resolution of  $1024 \times 578$  px. Depending on the flow field conditions, the time delay between the laser pulses is varied between  $15 - 30\mu\text{s}$ . For post processing of the images an interrogation area of  $16 \times 16$  px with a overlap of 50% was used. Mean flow field characteristics were obtained for various mass flow rates with and without combustion. Also the turbulent quantities like RMS velocities, turbulent intensity, vorticity, normal– and shear–stresses can be obtained optionally from postprocessing of the images.

<sup>18</sup>ILA Intelligent Laser Applications GmbH

## 4 Experimental Results and Discussion

This chapter presents the experimental results obtained from the atmospheric single burner test rig. First the operating domain and static flame characteristics at various operating conditions are presented. Then the comparison of alternative methods to determine the thermo–acoustical characteristics of lean premixed flames in gas turbine systems as given by their flame transfer matrix (FTM) is discussed. As introduced in chapter 3 these are the direct acoustic transfer matrices obtained from the multi microphone method (MMM), the hybrid method which is based on Rankine–Hugoniot (R–H) relations and the experimental flame transfer function (FTF) and finally the model based regression method (MBRM) where an analytical flame model ( $n-\tau-\sigma$ ) based on classical  $n-\tau$  formulation along with the low order network model has been applied to extract the dynamical flame characteristics. The comparison of all these methods against each other showed a very good consistency providing a global check between the measurements and modelling. Towards the end some results obtained with PIV measurements which are useful in developing the scaling rules (chapter 5) will be presented.

### 4.1 Operating domain

An operating domain of the single burner test rig with varying thermal power, preheat temperature and air excess ratio ( $\lambda$ ) has been obtained for PPM operation as shown in Fig. 4.1. The operating domain is basically divided into three regions for qualitative understanding. The rich limit zone is defined as the point where the flame just tries to enter into the burner before flashback occurs and the microphone measurements indicated a distinct peak. The rich limit seems to be less sensitive to preheat temperature and thermal power and stays almost constant.

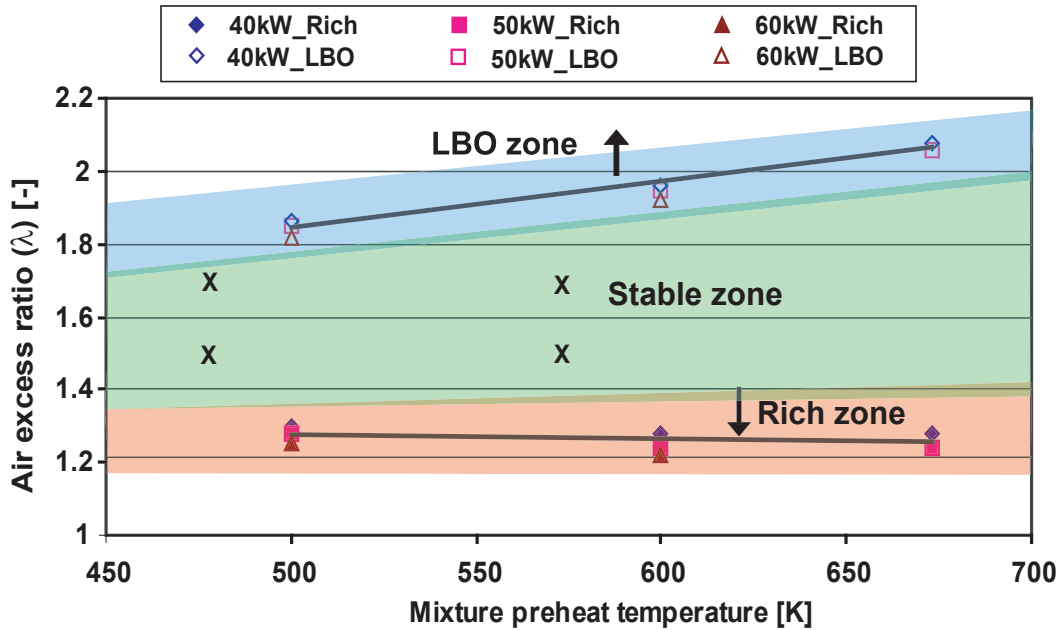


**Figure 4.1:** Operating domain of the single burner test rig with EV5 burner. The  $\times$  marks represents the location of acoustic measurements

The LBO limit zone is defined as the point where the flame becomes too long with rigorous fluctuations in the inner recirculation zone (IRZ) before it blows off. The weak trend can be observed that the increase in thermal power (throughput) actually decreases the LBO limit given by their  $\lambda$  values. This trend also has been observed in the work of Hoffmann et al. 1997 [35]. This can be due to the fact that with increase in mass flow rate, the turbulence intensity increases, which reduces the characteristic residence time  $\tau_t$  for almost a constant characteristic chemical time  $\tau_c$  and thus lowering the Damköhler number ( $Da = \tau_t/\tau_c$ ). However, the relative heat losses decrease with increasing power, since for fixed  $\lambda$  the heat released from the flame ( $\dot{Q}_{flame} \approx \dot{m}$ ) and the heat lost to the walls ( $\dot{Q}_{wall} \approx \dot{m}^{0.8}$ ) has a different proportionality factor to the mixture flow rate. This counteracts the decreasing turbulent time scale. The LBO limit shows a clear increasing trend with increasing preheat temperature. The region between rich and LBO limits is defined as stable region where all the static and dynamic flame characteristics have been measured. The points of acoustic measurements are indicated by  $\times$  for two different preheat temperatures and  $\lambda$  values.

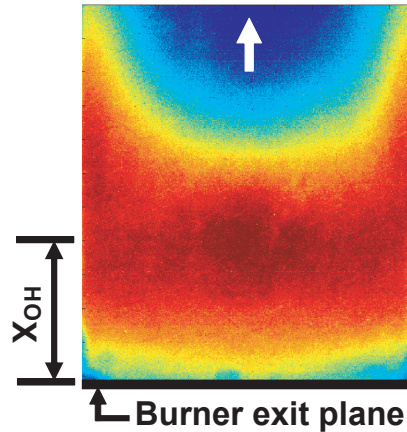


**Figure 4.2:** *OH<sup>\*</sup>-chemiluminescence image obtained at 50kW/1.7/300°C with EV5 burner*

Before performing the dynamic measurements (FTM), the static (unforced) flame behavior was investigated. The flame characteristics such as flame length and flame structure are obtained using the ensemble averaged OH<sup>\*</sup>-chemiluminescence flame images as mentioned in section 3.2.3. As an example the mean OH<sup>\*</sup>-chemiluminescence image taken at 50 kW thermal power, air excess ratio ( $\lambda$ ) of 1.7 and preheating temperature of 300°C (denoted as 50kW/1.7/300°C) in PPM operation is shown in Fig. 4.2. The burner exit plane is located on the bottom side of the image. The position of the maximum OH<sup>\*</sup>-chemiluminescence ( $X_{OH}$ ) is obtained by performing an integration of the OH<sup>\*</sup>-chemiluminescence images in longitudinal direction.

The flame lengths ( $\approx X_{OH}$ ) obtained at several operating points are plotted as a function of  $\lambda$  in Fig. 4.3. The flame lengths are normalized with the nominal burner diameter ( $D$ ). A clear trend of increase in  $X_{OH}$  with increase in  $\lambda$  is observed. For a given  $\lambda$  the  $X_{OH}$  is observed to increase with thermal power and decrease with preheat temperature. Two regions can be observed. A slower transition zone where the slope of the flame length curves is small and linear until some critical value where the slope changes rapidly. There the flame stabilization point moves downstream and the flame becomes longer. The slope of the flame length curve increases drastically making it a fast transition zone before the flame is blown off.

A close analysis of the flame length data provided in the higher air excess ratio

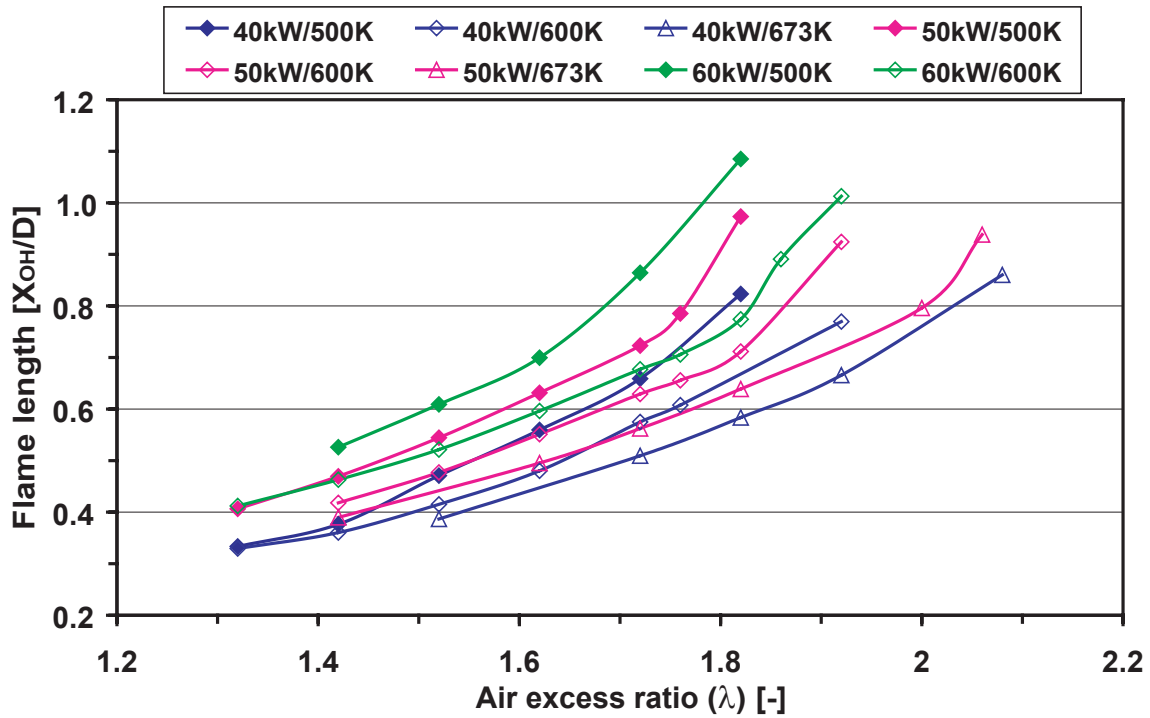


Figure 4.3: Flame lengths obtained at several operating conditions

region in Fig. 4.3 reveals that for the case of 40 kW there is no rapid change of slope compared to that of the other two thermal powers. The idea here is to check whether the LBO scales with the  $Da_t$ . From the experience and also looking at the  $\text{OH}^*$ -chemiluminescence image (Fig. 4.2) it is assumed that the 40 kW flame has less interaction with the walls compared with the other two cases. So, once a critical Damköhler number  $Da_{t,crit}$  is reached LBO occurs. For the 50/60 kW cases the flame is assumed to have stabilized even further at the stagnation point on the side walls which could be around  $x = 0.8D$  where low velocity and high turbulence is present. In this case the LBO behavior may not be straight forward. With this notion an attempt is made to develop some simple correlations based on  $Da_t$  to scale the LBO limits of the PPM flames which are investigated in the present work. From the simplified theories as presented by Turns, 2000 [97] the following correlations are used to represent the critical Damköhler number  $Da_{t,crit}$  [86] associated with the LBO limit:

$$Da_{t,crit} = 0.09 \frac{l_t}{u'} \cdot \frac{s_l^2}{\nu} \quad (4.1)$$

Here  $l_t$  the turbulent length scale,  $u'$ , the RMS velocity,  $s_l$  the laminar flame speed, and  $\nu$  the kinematic viscosity. These terms can be further simplified and represented in terms of the operating parameters as

$$s_l \propto (\alpha MW_f \bar{\omega} / \rho_c)^{\frac{1}{2}} \quad (4.2)$$

$$\bar{\omega} \propto \text{Exp}\left(\frac{-T_a}{T_{ad}}\right) \quad (4.3)$$

$$u' \propto U \propto \lambda \cdot T_c \cdot P_{th} \quad (4.4)$$

$$l_t \propto X_{OH} \quad (4.5)$$

with  $\alpha$  the thermal diffusivity,  $MW_f$  the molecular weight of the fuel,  $\rho_c$  the density of the cold unburnt mixture,  $\bar{\omega}$  the mean reaction rate using one-step reaction mechanism which is strongly dependent on the activation energy,  $T_a$  the activation temperature ( $\approx 15000$  K for  $CH_4$  flames),  $T_{ad}$  the adiabatic flame temperature,  $T_c$  the temperature of the unburnt mixture<sup>1</sup>,  $U$  the nominal burner velocity and  $P_{th}$  the thermal power. Now substituting the above relations (Eqns. 4.3 – 4.5) into Eqn. 4.1 a correlation for the  $Da_{t,crit}$  in the close vicinity of LBO is obtained:

$$Da_{t,crit} \propto \frac{X_{OH}}{\lambda \cdot T_c \cdot P_{th}} \cdot \text{Exp}\left(\frac{-T_a}{T_{ad}}\right). \quad (4.6)$$

For geometrically similar flames the LBO is expected to occur at a specific Damköhler number, i.e.  $Da_{t,crit}$ . Now looking at the LBO data for 40kW case in Fig. 4.1 the LBO occurs at 1.86 and 2.08 for the preheating temperatures of 500 K and 673 K respectively. The corresponding flame lengths can be obtained by extrapolating the data provided in Fig. 4.3 as a function of  $\lambda$ . This is done by

<sup>1</sup>for consistency in notation here  $T_c$ , the cold side of the flame, will also represent the unburnt mixture preheat temperature

assuming that the slopes for the 40kW case are not vary strongly compared to that of other two cases. Now substituting these values in Eqn. 4.6 and taking their ratio results in

$$\frac{Da_{t,crit}(40kW/1.86/500K)}{Da_{t,crit}(40kW/2.08/673K)} = 1.17. \quad (4.7)$$

As expected the ratio shows indeed that the  $Da_{t,crit}$  is constant within 20% error. This is satisfactory taking into account the fact that many over simplified assumptions were made. A similar analysis is made now comparing the case 60kW/500/1.82 with that of 40kW/1.86/500 resulting in

$$\frac{Da_{t,crit}(60kW/1.82/500K)}{Da_{t,crit}(40kW/1.86/500K)} = 0.97. \quad (4.8)$$

Once again the result shows that the LBO scales very well with the  $Da_{t,crit}$ . These results are particularly important to understand and develop further the scaling rules which will be presented in chapter 5.

## 4.2 Burner transfer matrices

Here the burner transfer matrices (BTM) without flame obtained from MMM, as described in section 3.2.1 in  $\frac{p'}{\rho c}$ ,  $u'$  notation, will be discussed. Two different burner configurations, the EV5 and the TD1 as presented in chapter 3, were investigated at different preheat temperatures on the single burner test rig. Based on previous studies of EV type burners by Polifke et al. 1997 [73] a  $l_{eff} - \zeta$  model was chosen to represent the measured data. Even though the burner is considered as a compact element (section 2.4.2), it has a finite length (100 mm), thus it is important to choose the exact location of the plane of area discontinuity or in other words the reference plane. For this burner configuration it was observed that the best results are obtained by choosing a reference plane 15 mm upstream of the burner exit plane.

The amplitude and phase values of the measured and modelled BTM are plot-

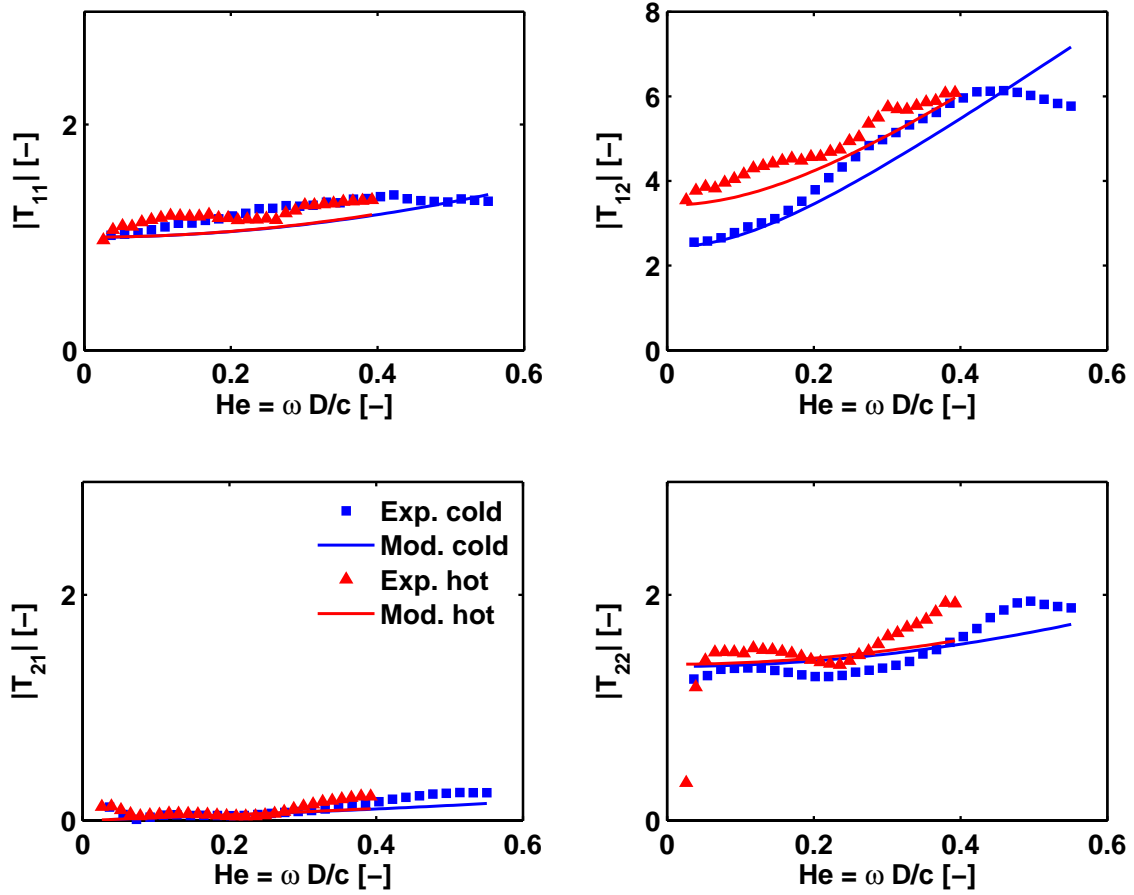


**Figure 4.4:** Amplitudes of the EV5 BTM coefficients with (hot, 300°C) and without (cold, 18°C) preheating

ted in Fig. 4.4 and Fig.4.5, respectively, for an air mass flow rate of 30 g/s. The frequency on the x-axis is normalized and represented as Helmholtz number,  $He = \omega D/c$ . This is done in order to compare the BTM obtained at various preheat temperatures. Since the ideal  $l_{eff} - \zeta$  model is expected to follow this scaling, the observed differences between the model and experiments may be indicative of missing physics in the model. In the figure a comparison between air temperature of 18°C and 300°C is shown. As seen from the plots, a very good agreement between the measurements and the model is obtained for almost entire frequency domain both with and without preheating. This confirms that this burner can be modeled as a compact element with losses as represented in Eqn. 2.62. The value of the  $l_{eff}$  ( $=0.1$ ) and  $\zeta$  ( $=1.8$ ) depends

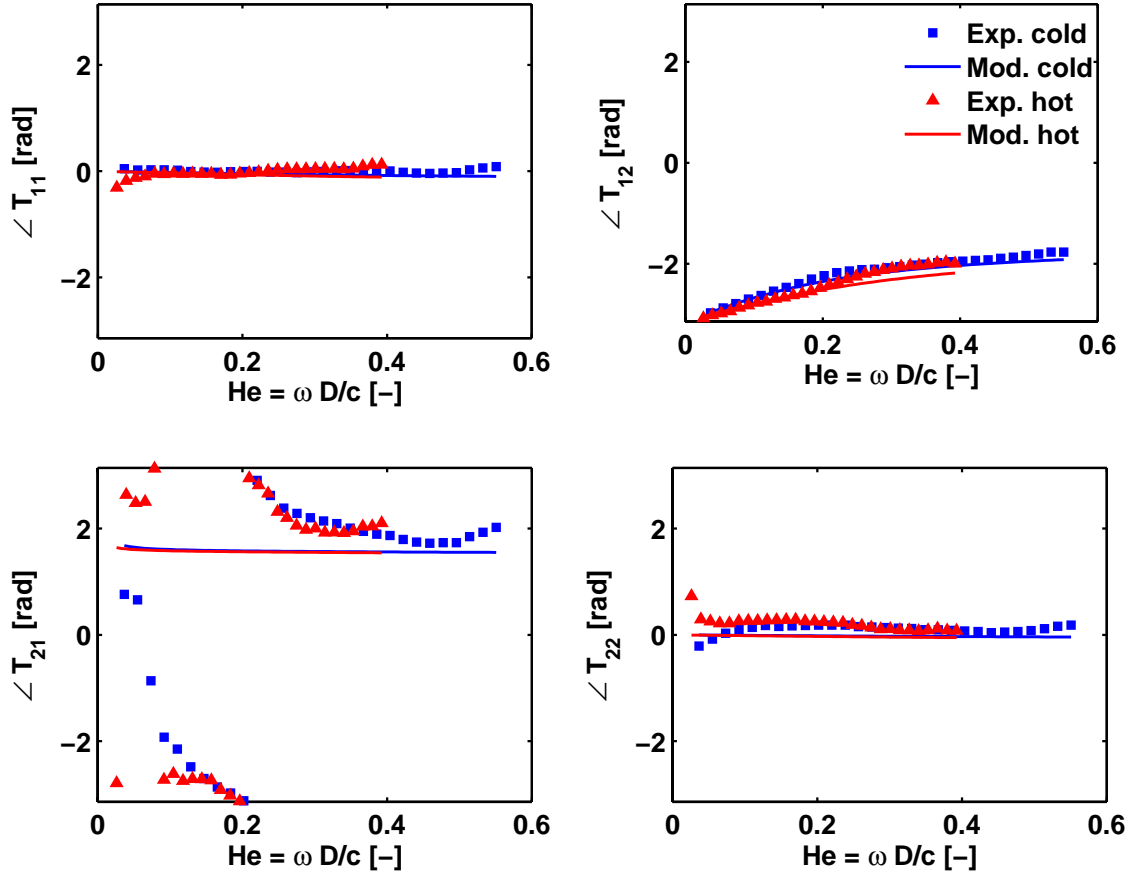


**Figure 4.5:** Phase values of the EV5 BTM coefficients with (hot, 300°C) and with out (cold, 18°C) preheating

on the cross sectional area (burner slot area =  $2 \times (80 \times 5) \text{ mm}^2$ ) chosen across the burner. The influence of these parameters can be observed from the amplitude values of the  $T_{12}$  element of the BTM. The  $l_{eff}$  which takes into account inertial effects, governs the slope of the curve. The value of the loss coefficient  $\zeta$  and the Mach number of the flow effect the offset of the curve from zero in the low frequency limit. Ideally, the model should produce identical results for any preheating, if the Mach number and pressure loss terms are neglected. Indeed this model was tested without mean flow ( $M = 0$ ) which reproduced the curves by normalizing the frequency with  $He$ . Therefore the observed differences between the two cases is clearly due to losses and Mach number difference. The influence of the reduced length  $l_{red} = 0.05$  (see Eqns. 2.52 and 2.62) on the  $T_{21}$  element has been checked and it was found to have a negligible ef-

fect. But, the small gain in this element has shown a rather weak dependency on the chosen reference plane. The phase value of this element shows a irregular trend as its amplitude is close to zero.

The quality of the measured transfer matrices can be checked by comparing the  $\zeta$  values obtained from the model ( $=1.8$ ) and the measured ( $=1.96$ ) mean loss flow coefficient from the static pressure drop across the burner. These values should be equal as the acoustic loss stems from the linearization of the mean flow. Indeed the ratio of these two quantities is observed to be around 0.92, showing that the loss coefficients obtained from the fit to the measured BTM and from the static pressure difference are similar. On the other hand the differences, if any, may stem from the entrance loss at the transition from plenum to the reduced plenum (see Fig. 3.1 chapter 3). This loss is acoustically not felt as it does not create a separated jet flow at the entrance. But, this loss is accounted in the static pressure drop measurements and as a result the  $\zeta$  values are slightly larger than that given by the model.

In contrast to the EV5 burner the TD1 burner (see Fig. 3.3) has a complicated flow path which contributes to some complexity in the acoustic behavior. The model for the TD1 should take into consideration how the flow adapts through the eight swirler slots, accelerating in the converging nozzle before being exited from a straight duct (see Fig. 3.4 in chapter 3). A detailed acoustic model for the TD1 burner is presented by Fischer et al. 2006 [23]. Here only the outline of this model consisting of different elements will be given:

- An area change without losses representing the transition of the plenum cross section to the restricted plenum cross section due to the presence of the burner.
- A duct element with 116 mm length representing the wave prorogation within the restricted length of the plenum.
- A pressure loss element considering the pressure loss across the burner. This value is obtained from the pressure drop measurements across the burner ( $\zeta = 1.4$ ).
- The nozzle is represented as a set of five discretized duct–area change

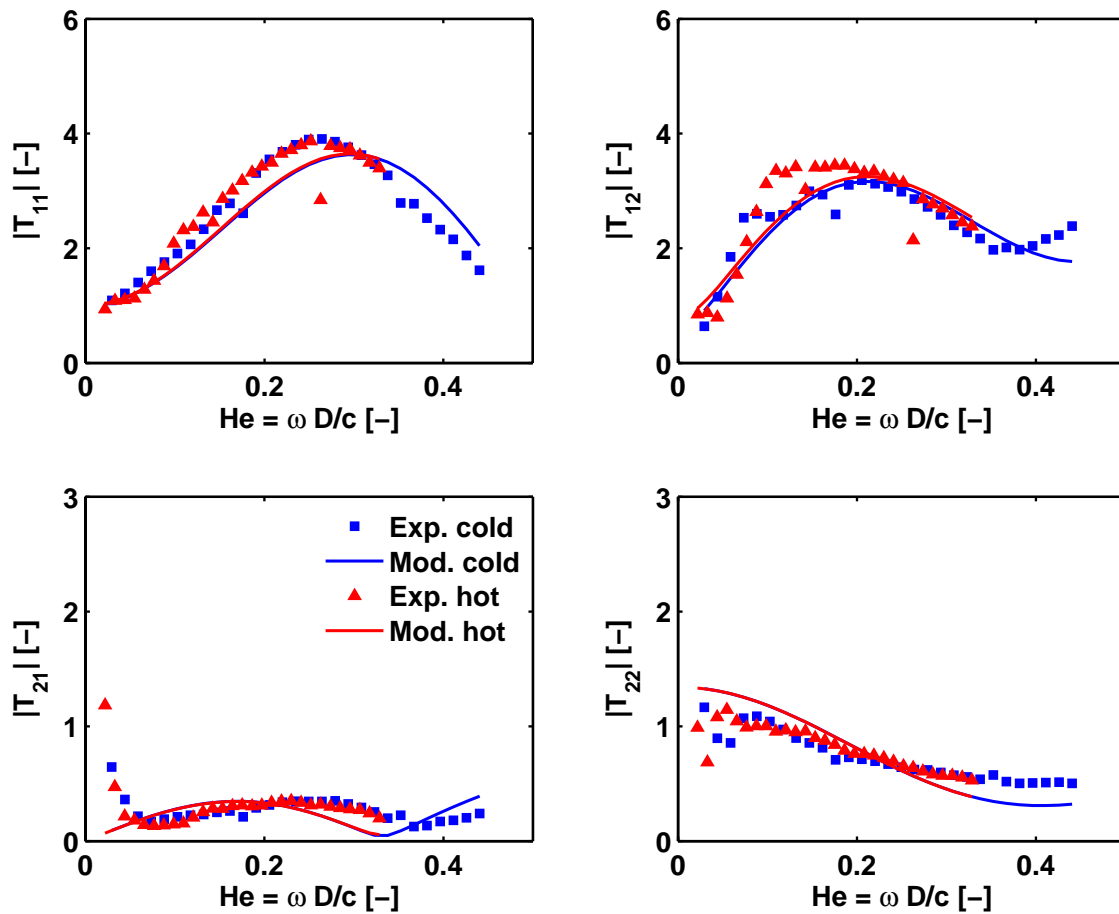


**Figure 4.6:** Amplitudes of the TD1 BTM coefficients with (hot, 250°C) and without (cold) preheating

elements with a total length of 52 mm.

- Duct element of 30 mm length.
- An area change element without losses due to sudden area change, representing the transition between the burner exit and the combustor. This element has a significant effect on the burner model.
- Finally a duct element with length -150 mm has been included to shift the upstream reference plane to a common reference plane at  $x = 0$  i.e., the burner exit plane. This distance is approximately equal to the distance between the center of the slot and the burner exit plane. With this the burner becomes formally an element with zero length which can be

placed at combustor front panel in a complex acoustic network model representing the entire combustion system.

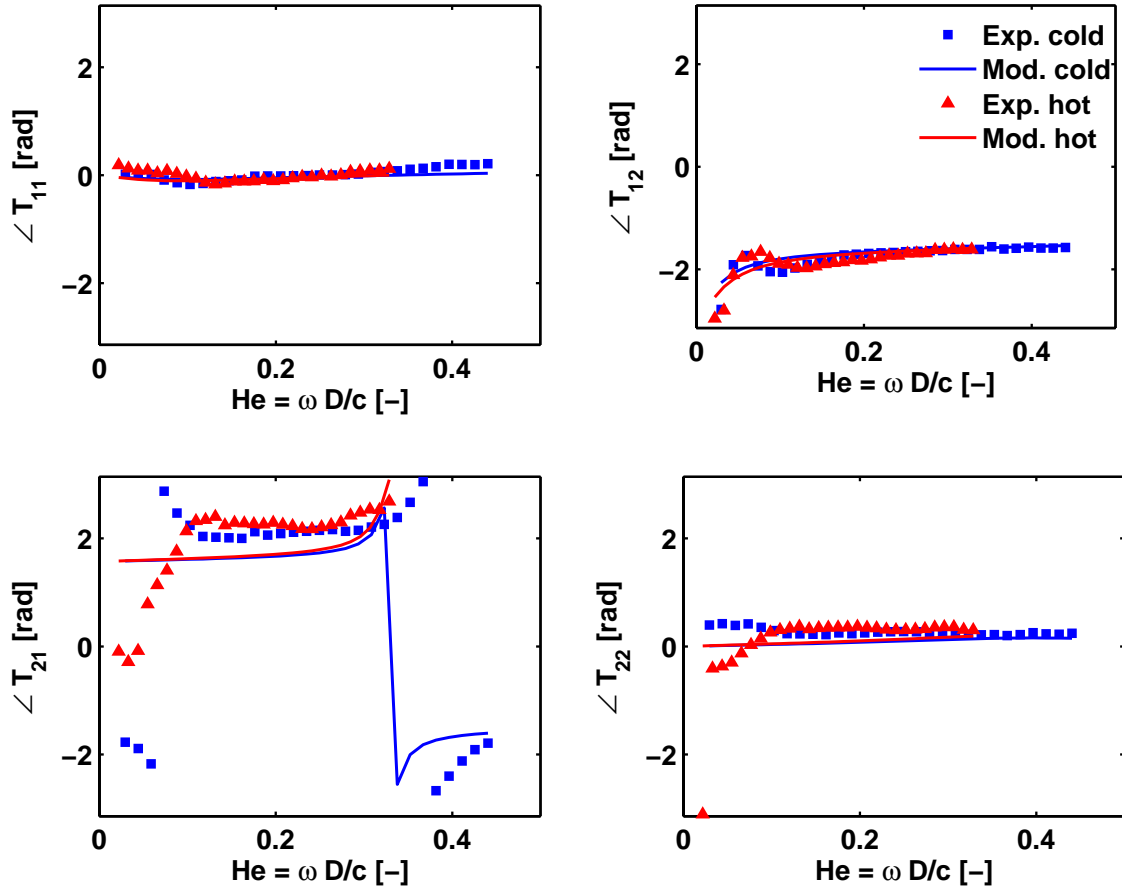


**Figure 4.7:** Phase values of the the TD1 BTM coefficients with (hot, 250°C) and without (cold) preheating

A comparison between measured and modelled BTM for the cases without preheating and with preheating of 250°C at same air mass flow rate of 30 g/s is shown in Figs. 4.6 and 4.7. The burner configuration investigated was 401616 as denoted in chapter 3. The comparison shows that the low order model predictions are in good agreement with the measurements. In particular, dynamics of the elements  $T_{11}$  and  $T_{12}$  with high gain compared to the other elements are closely captured by the model. The deviations from the model predictions can be attributed to the complex acoustic losses due to the mean flow effects. It was observed that the huge acoustic losses due to the sudden expansion at

the interface of burner exit and combustion chamber are to be considered in the analytical model for proper predictions. Also the phase values obtained with the model in Fig. 4.7 show very good consistency with the measurements throughout the frequency range investigated.

A close comparison between the EV5 and TD1 BTM results, in particular the amplitudes of the  $T_{12}$  element, show qualitative similarities in the low frequency domain. It seems that the EV5 burner reproduces (See Fig. 4.4, until  $He = 0.4$ ) the low frequency part of the TD1 burner (see Fig. 4.6, but until  $He = 0.2$ ). For both the cases the burner nominal diameters (50 and 40 mm, respectively) are used to normalize the frequency on x-axis. As only the axial waves are considered, it is motivated to use the burner physical length  $l_b$  for normalizing the frequency on x-axis. The TD1 burner is about twice (200 mm) as long as the EV5 burner (90 mm). For this reason, both the burners would have the peak in amplitudes of the  $T_{12}$  element near the same  $He$  number. A comparison of BTM is made between both the burners but now using  $He = \omega l_b / c$  for the same mass flow rate of 30 g/s as shown in Fig. 4.8.

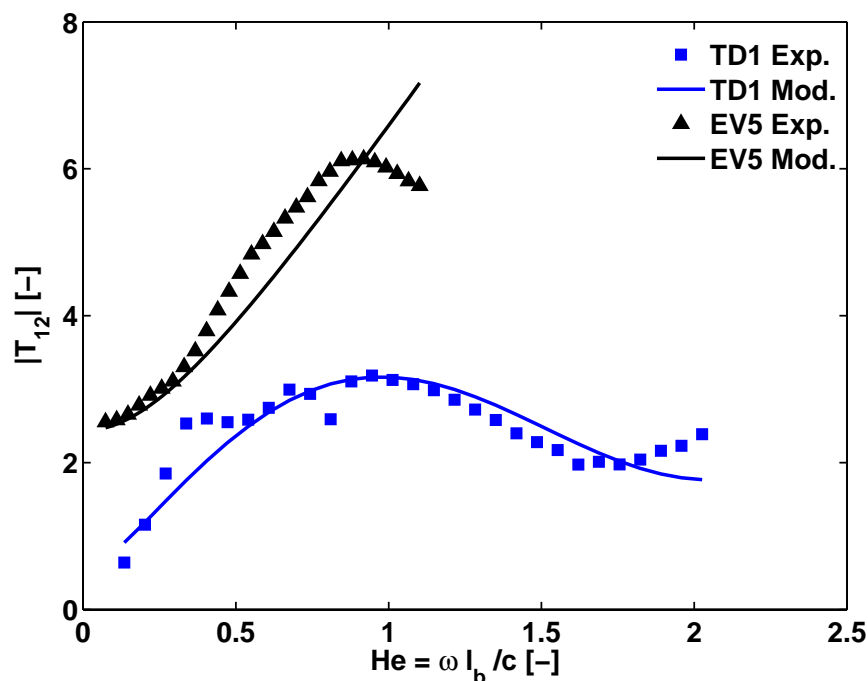


**Figure 4.8:** Amplitudes of the  $T_{12}$  element of the EV5 and the TD1 BTM

As expected the EV5 has reproduced qualitatively the behavior of TD1 burner with peak values around  $He = 0.9$  in both the cases. This implies that the EV5 burner with small physical length can very well be treated as an acoustically compact element and can be represented as a simple  $l_{eff}-\zeta$  model within the frequency range of interest ( $<600$  Hz or  $He < 0.9$ ). But, above a certain critical frequency this model may not hold anymore. This is because, the simple  $l_{eff}-\zeta$  model linearly increases the amplitudes of the  $T_{12}$  element with increase in frequency ( $He$ ), although the experimental data show a decreasing trend after  $He > 0.9$ . On the other hand, the low order model for the TD1 burner is very well in agreement with the experimental data even above its critical frequency ( $He > 0.95$ ). It indicates that this simple  $l_{eff}-\zeta$  model is not alone capable enough to predict the acoustic behavior of complex geometries. As a consequence, a successful mapping of the geometric details into a low order model is required in the high frequency regime. It can be concluded from the above analysis that the combined approach of low order modelling with some experimental inputs to optimize the free parameters lead to a precise 1-D acoustic model representing even complicated geometries.

### 4.3 Flame transfer matrices

As mentioned earlier, the present work has been carried out as a part of research project sponsored by ALSTOM as industrial partner. Consequently, the EV5 burner has been investigated more in detail. Hereafter, until otherwise stated only the results obtained with **EV5** burner will be discussed.

Flame transfer matrices (FTM) were obtained from the measured burner transfer matrices with flame (BFTM) and without flame (BTM) by using the Eqn. 3.15:  $FTM = BFTM \cdot BTM^{-1}$ . The FTM were obtained for several operating conditions both in PPM and IPM operation by varying the thermal load,  $\lambda$  and preheat temperatures. First a comparison will be made between the calculated FTM in  $(\frac{p'}{\rho c}, u')$  notation at 50kW/1.7/300°C with the measured BTM (30 g/s) with and without flame in the PPM operation. The amplitude and phase values of the transfer matrices are plotted over the frequency domain as shown in Fig. 4.9 and Fig. 4.10, respectively.

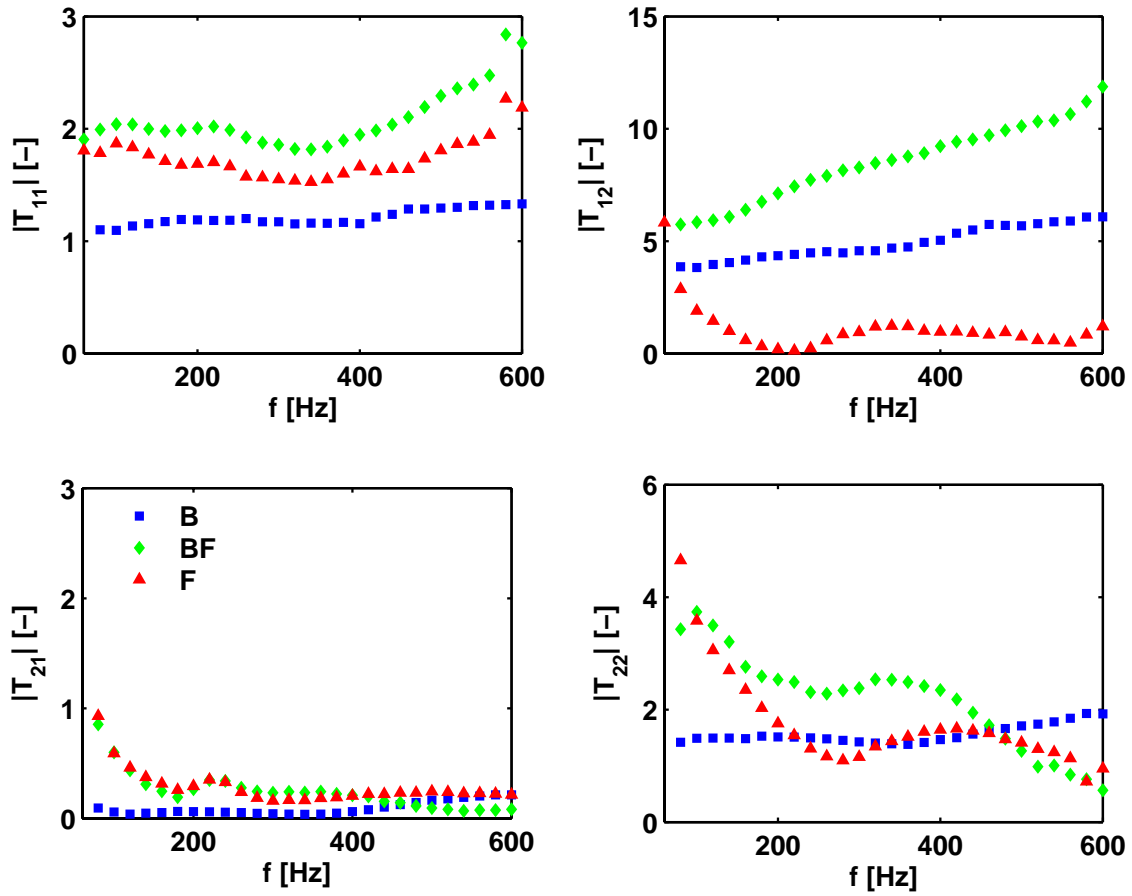


**Figure 4.9:** Amplitudes of the burner and flame transfer matrices

The data for the burner alone (B) and burner with flame (BF) shows the expected similarity in both amplitude and phase values for the  $T_{11}$  and  $T_{12}$  element. The  $T_{11}$  element which relates the pressures across the burner and flame has zero phase. This indicates that for a low Mach number flow the flame dynamics is not strongly influenced by the pressure and the scaling is given by the ratio of specific impedances up and downstream of the flame ( $\beta = (\bar{\rho}c)_c / (\bar{\rho}c)_h$ ). Thus the offset between the  $T_{11}$  element of burner and burner with flame leads to a value of approximately 1.73. The  $T_{12}$  element relates the pressures downstream to the velocity upstream of the burner and flame. This element is typically characterized by a linear increase of the absolute value and a phase value from  $-\pi$  to  $-\pi/2$  with increasing frequency. This element is not strongly influenced by the presence of the flame, hence the

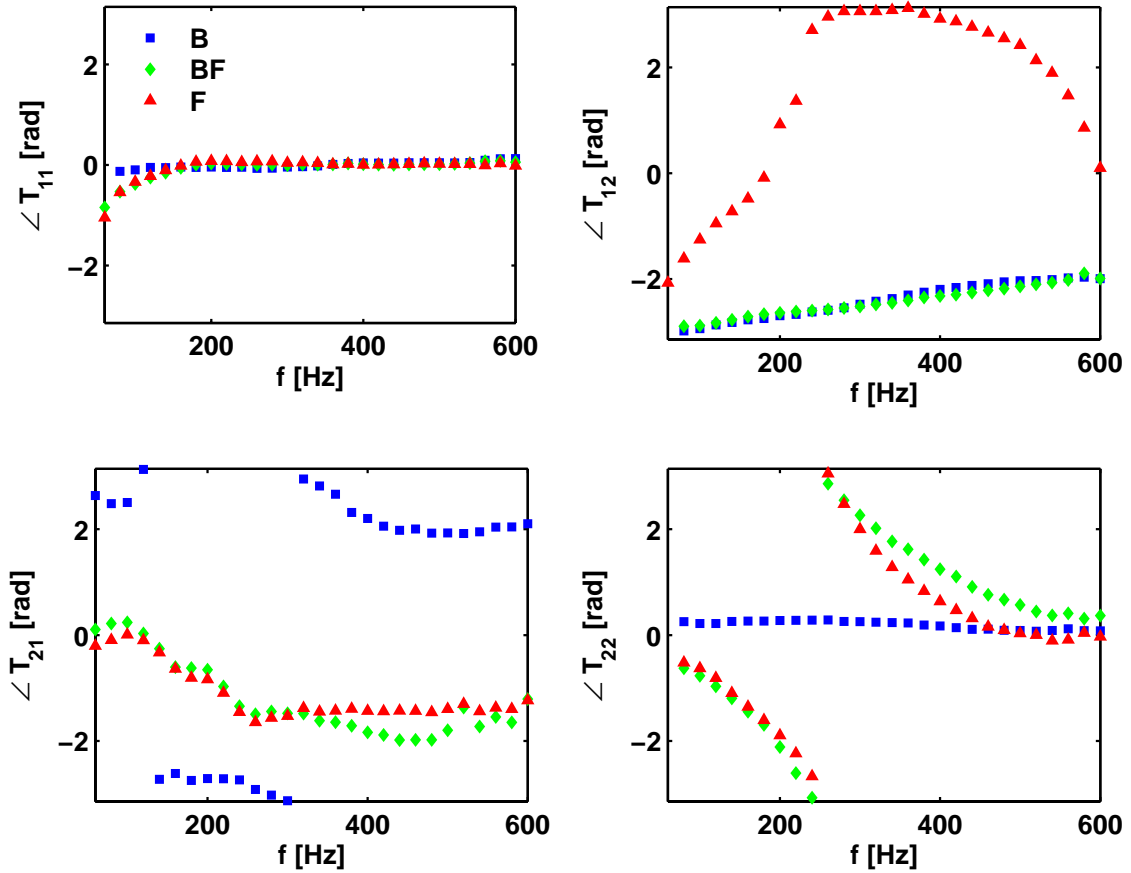


**Figure 4.10:** Phase values of the burner and flame transfer matrices

$T_{12}$  element of the flame alone can be observed with an absolute value of almost zero and with an irregular trend in phase [87]. The  $T_{21}$  element which relates the velocity downstream to the pressure upstream has very small amplitudes compared to the other elements. This is also reflected in the phase values with large discrepancies. Finally the  $T_{22}$  element relating the acoustic velocities up- and downstream of the flame represents the most important dynamics present in it. The phase values drops almost linearly in the low frequency domain. This is characteristic for the convective time delays. In the high frequency domain the absolute and phase values of the  $T_{22}$  element converges to unity and zero, respectively, indicating a damping of the dynamic behavior.

The  $T_{22}$  element of the FTM is greatly influenced by  $\lambda$ , preheat temperature

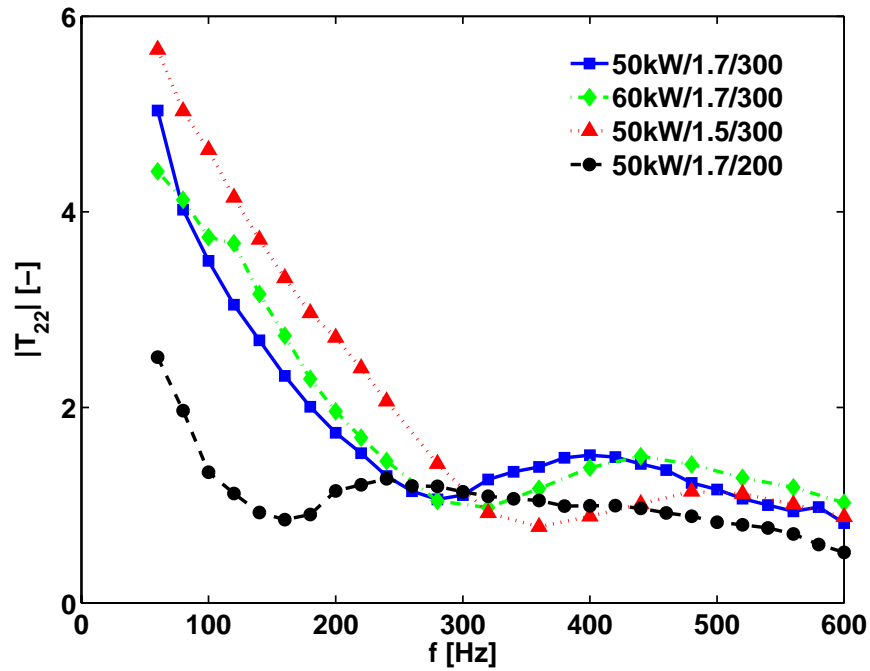


**Figure 4.11:** Amplitudes of the  $T_{22}$  element of the FTM in PPM operation

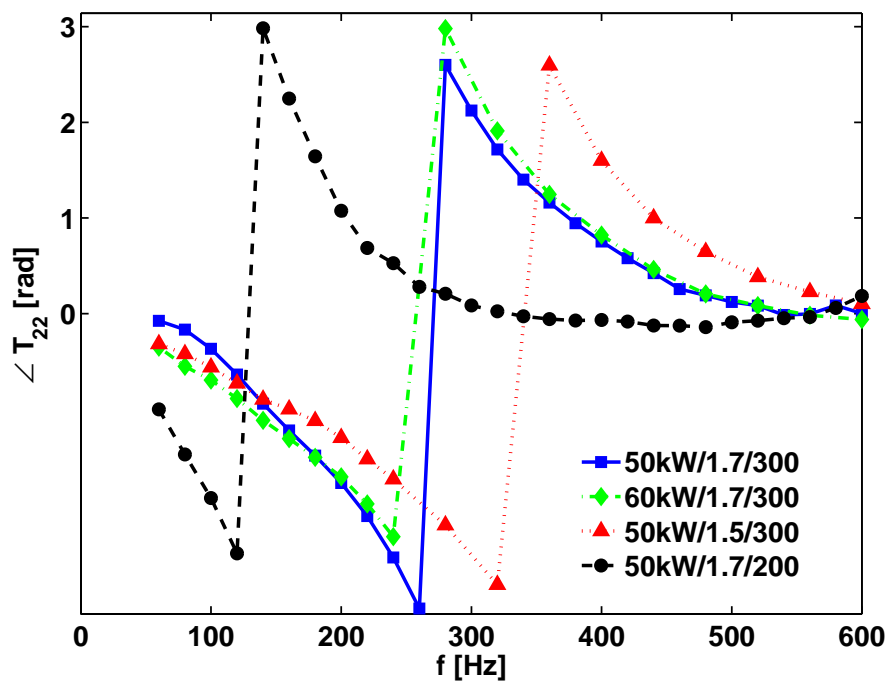


**Figure 4.12:** Phase values of the  $T_{22}$  element of the FTM in PPM operation

and to some extent by thermal load. For this reason, only the  $T_{22}$  element amplitude and phase values for different operating conditions are plotted in Fig. 4.11 and Fig. 4.12 respectively. From these plots it can be observed that the FTM is not much influenced by varying thermal load from 50kW to 60kW. However, it is very much sensitive to the preheat temperature and the  $\lambda$  values which directly effect the flame temperature and thus the turbulent flame speed. From the phase plots we can see clearly that with increasing  $\lambda$  from 1.5 (red triangles) to 1.7 (blue squares), the phase drops steeply. This is due to the decrease in adiabatic flame temperature, the turbulent flame speed decreases shifting the flame front position further downstream of the burner and thus the convective delay times increase. Also a similar behavior with decrease in mixture preheat temperature from 300°C (blue squares) to 200°C (black circles) can be observed. But, in this case the amplitudes show a strong deviation towards the low frequency limit. This is due to the fact that at low preheating and high  $\lambda$  value the flame structure and its behavior was different from other operating points. This behavior is also confirmed from the static flame measurements.

The dynamics of the FTM as discussed above are highly dependent on the operating conditions and frequency. Following the work of Lohrmann and Büchner, 2004 [48] the FTM ( $T_{22}$  element) behavior for a given burner geometry can be made independent of the operating condition if the frequency is normalized and represented as *Strouhal number*  $Str = f X_{OH}/U$ , with  $X_{OH}$  defined the position of the maximum OH\*-chemiluminescence measured and  $U$  the nominal burner exit velocity.

A comparison is made between the amplitude and phase values of  $T_{22}$  element after the frequency is normalized and represented by Strouhal number as shown in Figs. 4.13 and 4.14. The amplitude now shows a same behavior independent of the operating point. In particular, the phase function (Fig. 4.14) of the  $T_{22}$  element shows a characteristic time delay which is almost independent of the preheating temperature, thermal power and  $\lambda$ . As observed from the plots, the individual time delay ( $\tau \propto X_{OH}/U$ ) for each set of operating conditions obviously is the key for the normalization of the measured flame dynamics. This is a very important finding in order to develop scaling rules

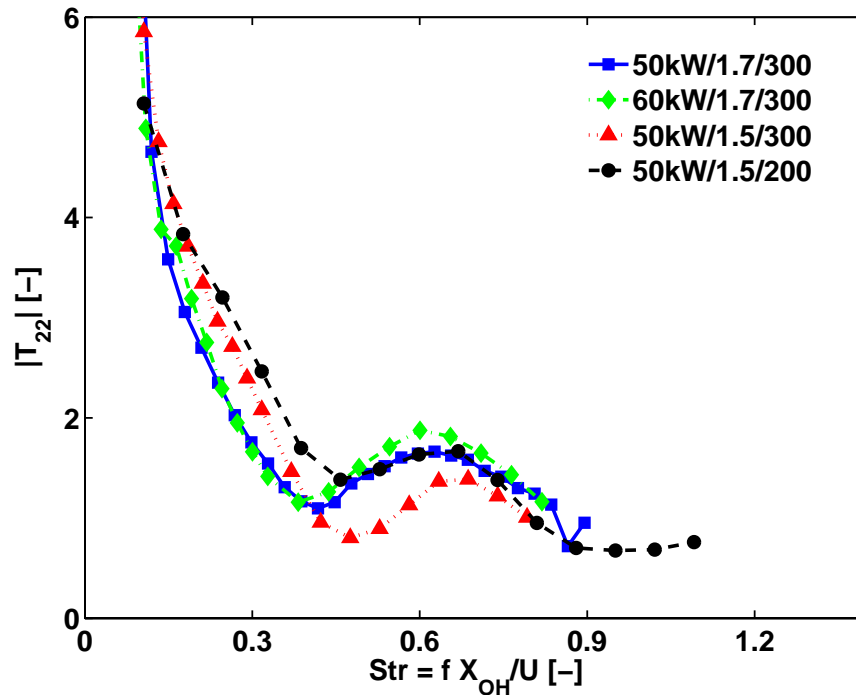


**Figure 4.13:** Amplitudes of the  $T_{22}$  element of the FTM in PPM operation with frequency normalized and represented as Strouhal number

(physical models) which are useful to calculate the time delay and its distributions for a set of operating points as will be discussed in chapter 5. Overall the quality and repeatability of the measurement technique can be observed from the smoothness in the curves, qualifying these results as benchmark data to validate other alternative methods and the network model which will be presented in the following sections.

#### 4.4 Flame transfer function - hybrid method

Here the desired FTM is obtained from the measured FTF and using the R–H relations making it a hybrid method [22]. The FTF is defined as the ratio of heat release fluctuations to the acoustic velocity fluctuation at the burner exit plane (Eqn. 2.75). This is the most conventional method, where heat release fluctuations are measured from the  $\text{OH}^*$ -Chemiluminescence releases from the flame using an UV-photomultiplier (see section 3.2.3) and velocity fluc-

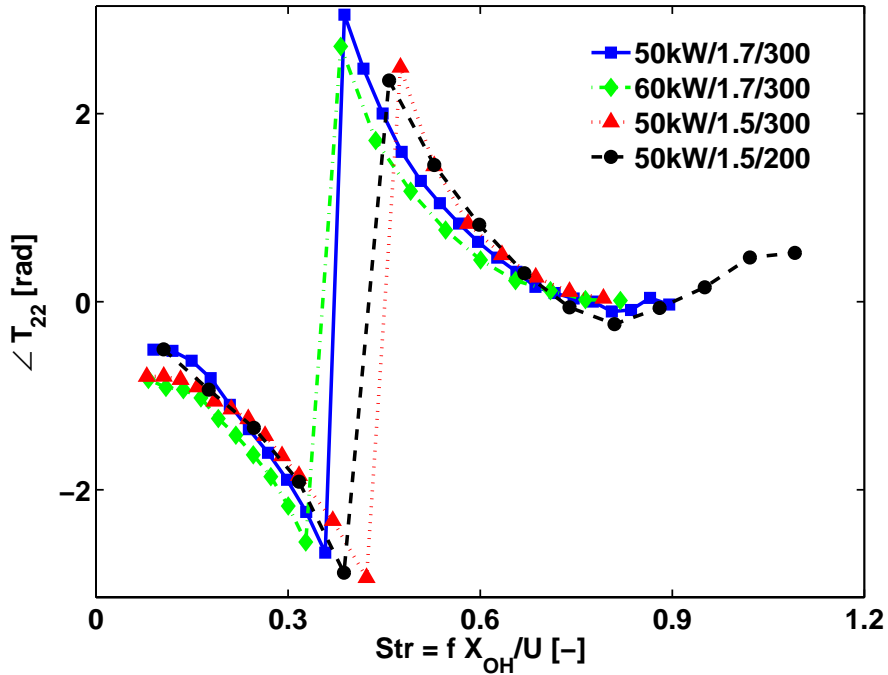


**Figure 4.14:** Phase values of the  $T_{22}$  element of the FTM in PPM operation with frequency normalized and represented as Strouhal number

tuations using a constant temperature anemometer (CTA) (see section 3.2.2). This method is simple and faster from the experimental point of view. Alternatively, the burner exit velocity fluctuations were calculated from the simultaneously measured pressure field upstream of the burner using 1-D network theory. From the MMM, as explained earlier, the upstream Riemann invariants  $f_u$  and  $g_u$  ( $p'_u, u'_u$ , inside the plenum) are multiplied with the known cold BTM to get the downstream  $f_d$  and  $g_d$  ( $p'_d, u'_d$ , inside the combustion chamber). The velocity fluctuations at the burner exit can then be obtained after scaling with an appropriate area ratio ( $A_{cc}/A_b$ ).

A comparison is made between the FTF obtained by the CTA method (black squares) and the network method (blue triangles) as shown in Fig. 4.15. The left side of the plot shows the FTF amplitude and phase values obtained with TD1 burner. Here, with a relatively simple exit geometry the CTA can be positioned properly just upstream of the burner exit plane. The acoustic velocity obtained by the CTA method and the network approach is normalized with the mean flow velocity. This quantity together with the normalized heat re-

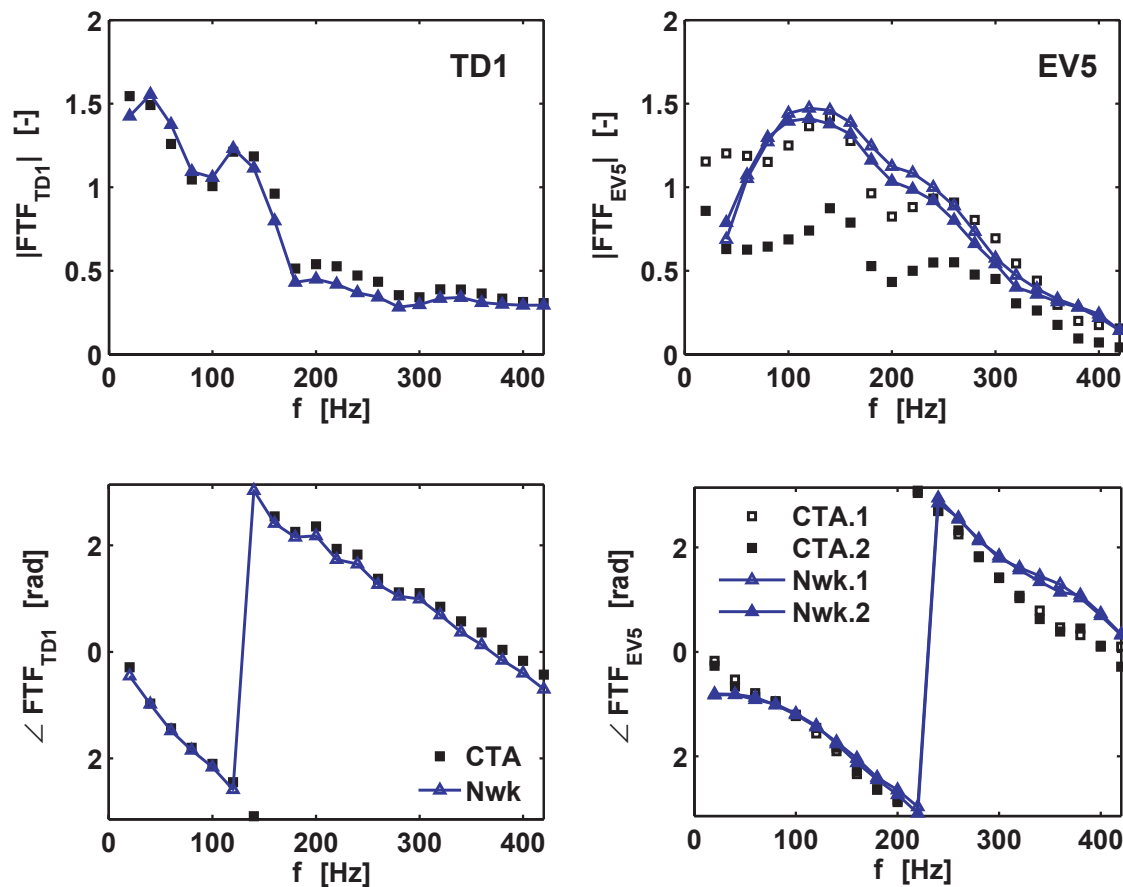


**Figure 4.15:** *FTF comparison obtained from conventional CTA method (black) and with network based method (blue) measured on different days 1 and 2*

lease fluctuation from the photomultiplier allows to calculate the FTF  $f_Q(\omega)$  as represented in Eqn. 2.75. As seen from the figure, both these methods are proven to be equivalent in the case of TD1 burner for entire frequency domain.

On the right side of Fig. 4.15, the FTF amplitude and phase values measured with the EV5 burner using both the methods on two different days (1 and 2) are presented. In the case of network method (blue triangles) a good reproducibility both in amplitude and phase can be observed throughout the frequency domain. The phase values show good consistency almost in the entire frequency domain for both these methods. However, the amplitude measured on two different days deviate strongly with the CTA method (black squares). This

can be attributed to difficulties from CTA positioning in complex geometries like EV5. During the measurement campaign with preheated air, the response from the CTA was found to be varying and reproducibility was not achievable. The CTA response was very much sensitive to its location and the orientation inside the burner slots.

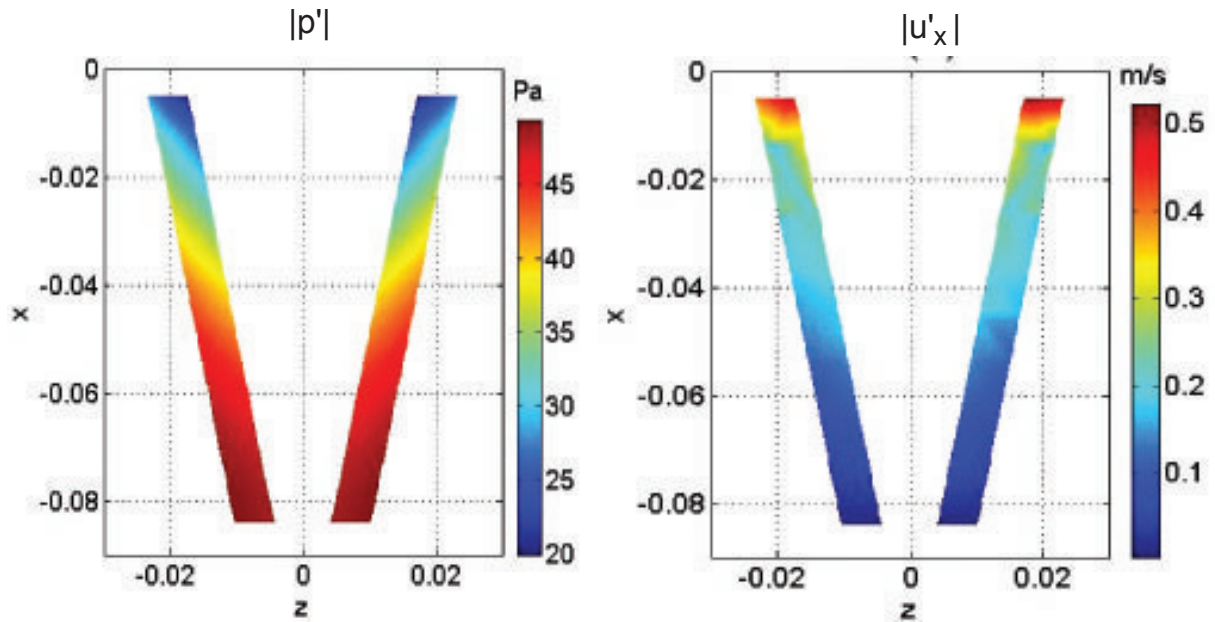


**Figure 4.16:** Amplitudes of the acoustic pressure and velocity (axial) inside the EV5 burner slots obtained using an acoustic FEM model at 350Hz

In order to understand the acoustic flow field, analysis was performed using a 3-D acoustic finite element model (FEM) from a commercial software (COM-SOL 3.2). The details of FEM model are presented in the Appendix. The amplitudes of acoustic pressure and velocity obtained as an example at 350 Hz are plotted in Fig.4.16. The results clearly indicate large acoustic pressure and velocity gradients across the burner slots, both in radial ( $z$ -axis) and axial direction ( $x$ -axis). This explains that a suitable position for the CTA measurements was not achievable for this burner configuration. From the above analysis it is concluded that the network method as compared to the CTA method is more reliable and reproducible for measuring the acoustic velocity fluctuations for the burner type investigated here. Finally, substituting this experimental FTF ( $f_Q(\omega)$ ) into the acoustic R-H relations and rearranging the equations we get the FTM as shown in Eqn. 2.76 making it a hybrid method.

## 4.5 Analytical flame transfer matrix

The flame is treated as a compact element or discontinuity at a single plane. From the conservation laws it was shown in chapter 2, how the acoustic relations across this plane can be derived (Eqns. 2.71 & 2.72). To get the closure for the flame transfer matrix given by Eqn. 2.76, the heat release fluctuations are modeled in terms of the FTF ( $f_Q(\omega)$ ) with free parameters ( $n, \tau, \sigma$ ) as shown in Eqn. 2.87 for PPM operation. Using this distributed time lag model the complete transfer matrix can now be described analytically. However, these free parameters require a fit to the directly measured FTM.

### 4.5.1 Global check

Here the FTM obtained with MMM directly is compared with those obtained from hybrid and analytical methods. The amplitude and phase values of the FTM as an example at 60kW/1.7/300°C are plotted in Figs. 4.17 and 4.18.

The amplitudes of the  $T_{12}$  and  $T_{21}$  elements are very small compared to the other elements and hence the phase values show an arbitrary behavior. The most dynamic element  $T_{22}$ , shows a high interaction between the flame and acoustic velocity in the low frequency domain, which can also be observed in the phase values. A very good agreement between the pure acoustically determined direct FTM (black) and the OH\*–chemiluminescence based hybrid method (blue) provides a check on either method. An analytical description of the flame model using  $n, \tau, \sigma$  parameters was also consistent with the measured data. This indicates that the flame model with distributed time lags is very much capable of representing the flame under investigation. These results also prove the applicability of the three different methods to obtain the dynamic flame parameters in PPM operation.

However, the same procedure of global check may not be possible in the case of IPM operation where we expect high equivalence ratio fluctuations which are discussed in the following section.

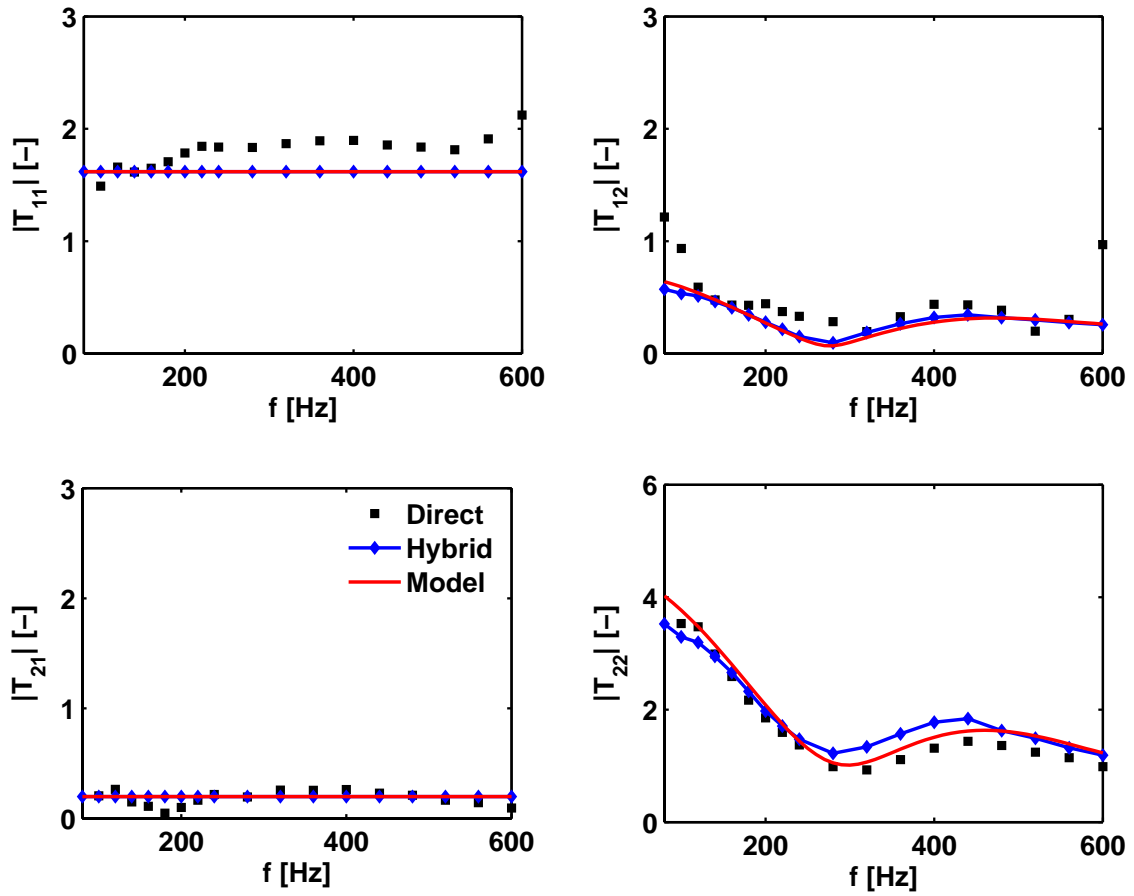


**Figure 4.17:** Global check showing the consistency between the directly measured, the hybrid  $\text{OH}^*$ -chemiluminescence method and the analytical Rankine-Hugoniot approximation for a PPM operation

## 4.6 Injector premixed mode operation (IPM)

In this mode the mixture is generated by fuel injectors within the burner. This results in temporal as well as spatial mixture inhomogeneities which are overlaid on the turbulent and acoustic velocity fluctuations. The observed sensitivity of the heat release fluctuations to equivalence ratio fluctuations in the lean [37] regime indicates that in a lean premixed gas turbines, fuel concentration fluctuations cause a very strong feed back mechanism. Several theoretical models have been proposed [25, 81] to simulate the interaction between heat release and fuel concentration fluctuations based on the time lag approach

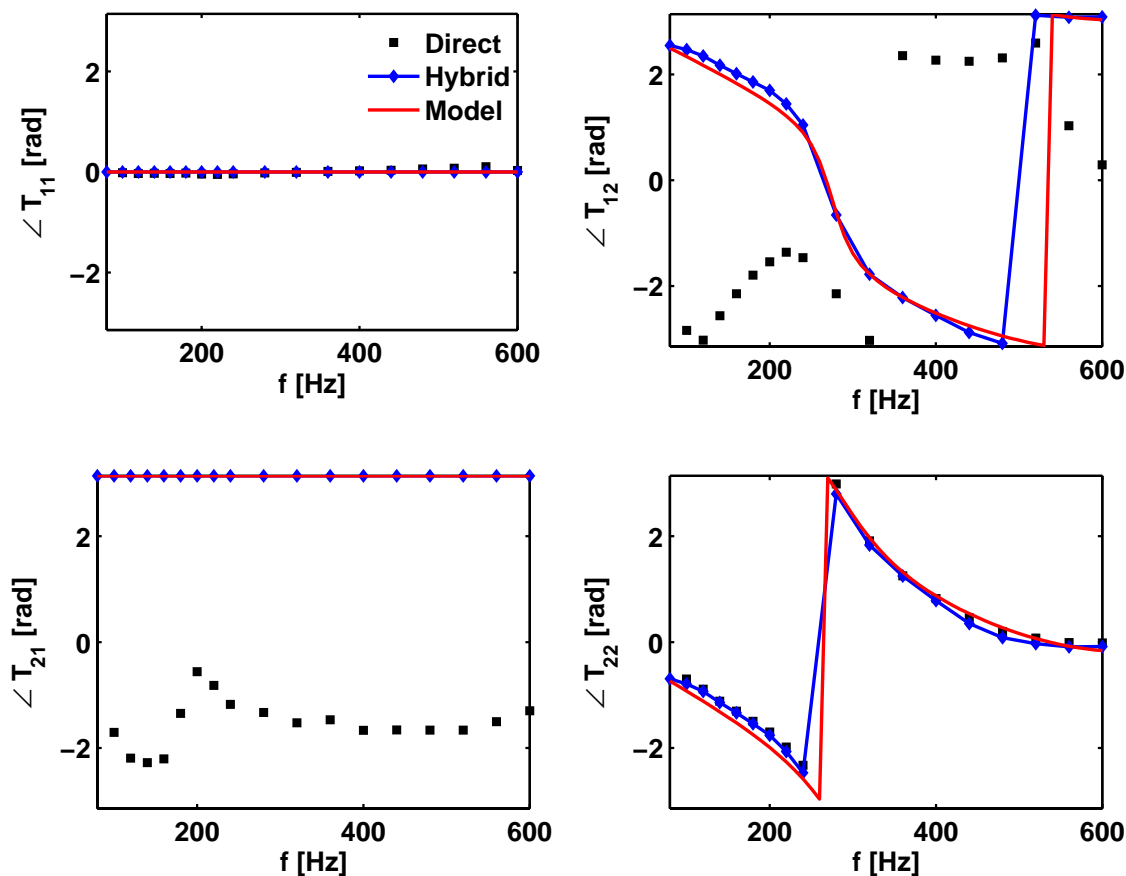


**Figure 4.18:** Global check showing the consistency between the directly measured, the hybrid  $\text{OH}^*$ -chemiluminescence method and the analytical Rankine-Hugoniot approximation for a PPM operation

where the fuel concentration fluctuations are caused by acoustic fluctuations at fuel injector location. These fuel concentration fluctuations are convected downstream towards the flame, with a convective time delay depending on the flow field interaction between injector and flame front.

The FTM in IPM are measured at several operating conditions using MMM. The absolute and phase values of the most dynamic  $T_{22}$  element are plotted in Figs. 4.19 and 4.20. Particularly the amplitudes of the  $T_{22}$  element in the low frequency limit ( $f \rightarrow 0$ ) shows a strong decay followed by a rise around 200 Hz and again a strong decay converging to a value of unity. In the very low frequency limit the heat release due to the velocity fluctuations at the burner exit (flame speed fluctuations) are out of phase with the heat release fluctuations

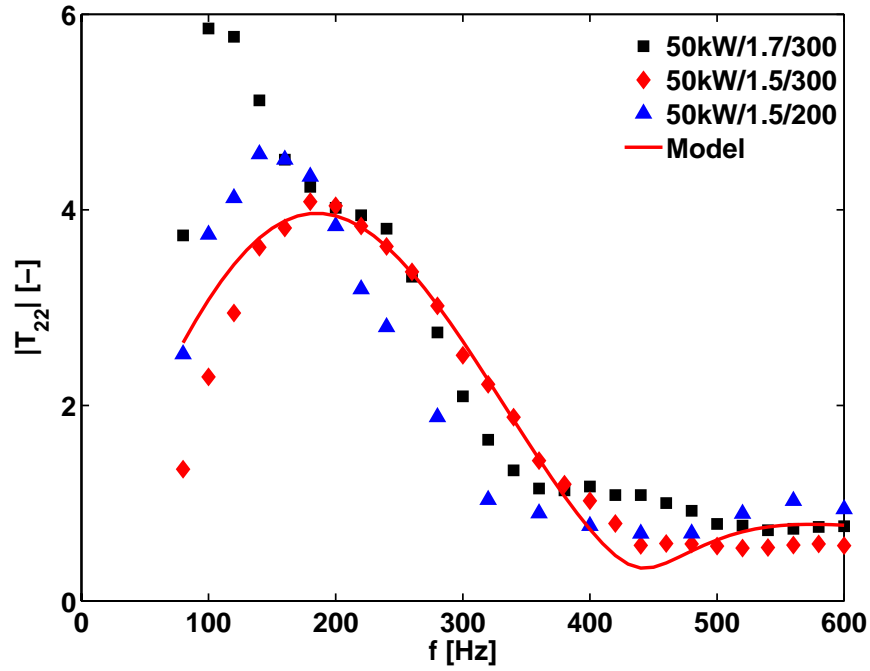


Figure 4.19: Amplitudes of the  $T_{22}$  element of the FTM for IPM operation

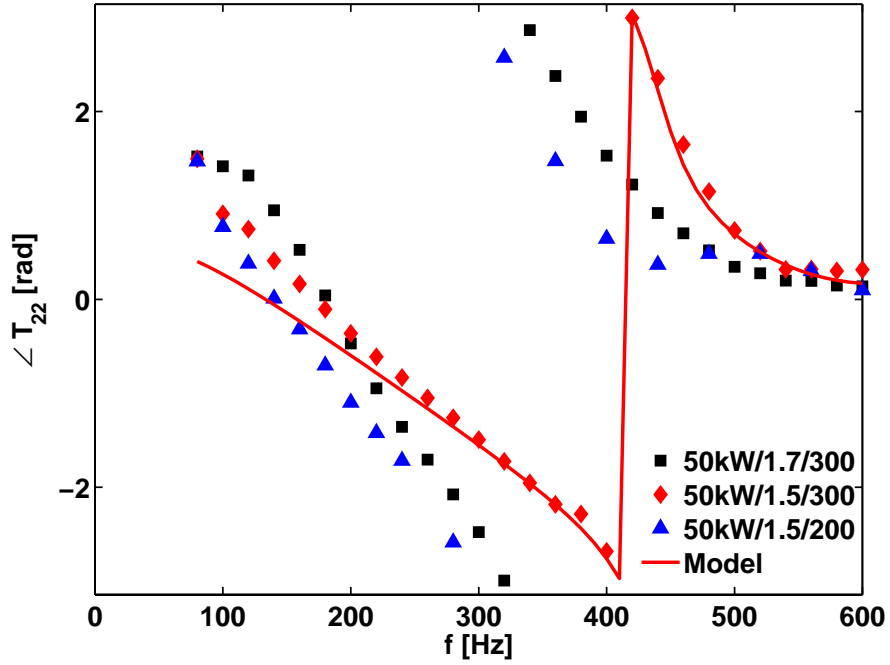


Figure 4.20: Phase values of the  $T_{22}$  element of the FTM for IPM operation

due to the fuel concentration fluctuations. Therefore according to the Eqn. 2.91 we see that the amplitude of the  $T_{22}$  element tends to a value of unity. This effect is also clearly visible from the phase values plotted in Fig. 4.20, where it tends to a value of  $\pi$ . This is a characteristic of a “fuel stiff” system also observed prominently in previous investigations by Auer et al. 2005 [3] and Lohrmann et. al. 2003 [49]. For instance within a pulsating period with increasing air mass flow (increase in  $u'$ ) at the burner exit the air equivalence ratio decreases, causing a decrease in flame temperatures (decrease in  $\dot{Q}'$ ). The resulting phase shift between the velocity fluctuation at the burner exit plane and photomultiplier signal converges to a value of  $\pi$ . The plot also shows the generally expected behavior: with increase in air excess ratio (from 1.5 to 1.7) or decrease in the preheat temperature (from 300°C to 200°C) the phase delay increases. Towards the high frequency domain the amplitude and phase values decay strongly to unity and zero respectively indicating an axial dispersion of equivalence ratio fluctuations and follow the same behavior as in the PPM operation. Care should be taken while interpreting the amplitude gain in the low frequency region (<100Hz, 50kW/1.7/300) as the measurements here were quite sensitive to the excitation amplitude with the upstream siren. As this siren acts as a mechanical shutter directly modulating the air flow for a fixed fuel flow rate, significant heat release fluctuations were observed.

As discussed in section 2.5.4 the FTM including the equivalence ratio fluctuations can be obtained from Eqn. 2.91. Once again the model free parameters in this case ( $n$ ,  $\tau$ ,  $\sigma$ ,  $\tau_\phi$ ,  $\sigma_\phi$ ) are obtained by fitting these to directly measured FTM as shown in Fig. 4.19 and Fig. 4.20. The model fit to the experimental data obtained at the operating point 50kW/1.5/300 (red diamonds) is shown with a solid line. The result indicate a good agreement with the measured FTM above 100 Hz.

## 4.7 Interpretation of flame parameters

A summary of the dynamic flame parameters obtained at several operating points are provided in Table. 4.1. The mean and standard deviations of convective time delay are normalized (represented with \*) such that  $\tau^* = \tau U/D$ .

Where  $U$  and  $D$  are the nominal burner exit velocity and burner diameter. The mean time delays due to the velocity fluctuations at the burner exit in the PPM operation are slightly larger compared to the IPM operation at their respective operating points (compare columns 3 and 7). This is also revealed to some extent in the flame lengths ( $X_{OH}$  compare columns 5 and 11) obtained from the time averaged  $OH^*$ -chemiluminescence images as shown in Fig. 4.2. Care should be taken while interpreting the  $OH^*$ -chemiluminescence images (or intensity  $I$ ) taken in IPM operation. Due to unmixedness in this mode, the proportionality factor between the heat release and the chemiluminescence emitted from the flame may not be the same as in the PPM and generally the chemiluminescence intensity is over predicted [4, 90]. For this reason the hybrid method, which uses the  $OH^*$ -chemiluminescence to determine the heat release fluctuations ( $\dot{Q}'$ ) was not applicable for the IPM operation. Nonetheless, in preheated lean flames with small equivalence ratio fluctuations it is assumed that the sensitivity of intensity with equivalence ratio is fairly small at least in the **static** operation. Consequently, the images taken in static operation were still used to represent the location of maximum  $OH^*$ -chemiluminescence intensity.

**Table 4.1:** Summary of mean and standard deviation of the convective time delays. The values are normalized as  $\tau^* = \tau \cdot \frac{U}{D}$ ;  $n^* = n / (T_h / T_c - 1)$ .  $X_{OH}/D$  is the flame length normalized with the nominal burner diameter

Operating point [kW/ $\lambda/T_c$ ]	PPM				IPM					
	$n^*$	$\tau^*$	$\sigma^*$	$X_{OH}/D$	$n^*$	$\tau^*$	$\sigma^*$	$\tau_\phi^*$	$\sigma_\phi^*$	$X_{OH}/D$
40kW/1.7/300°C	1.67	0.84	0.33	0.68	-	-	-	-	-	-
50kW/1.7/300°C	1.39	0.93	0.29	0.75	1.53	0.69	0.29	1.44	0.41	0.67
60kW/1.7/300°C	1.54	1.04	0.37	0.81	-	-	-	-	-	-
50kW/1.5/300°C	1.55	0.62	0.27	0.59	0.91	0.45	0.20	1.20	0.24	0.54
50kW/1.5/200°C	1.46	0.76	0.31	0.65	0.90	0.52	0.21	1.33	0.28	0.60
50kW/1.7/200°C	1.06	1.46	0.46	0.84	-	-	-	-	-	-

The time delay values show a strong dependency on  $\lambda$  and preheat temperature and rather a weak dependency on thermal power. This is due to the Strouhal scaling, as the burner diameter  $D$  instead of  $X_{OH}$  was used. The stan-

dard deviation of the time delays ( $\sigma^*$ ) show more or less a constant behavior with values around 30% of their respective mean time delays. This can be due to the flame structure and hence, the distribution of the flame surface is very similar with only the mean position varying for all the operating points investigated. The only exception is the case with 50kW/1.7/200°C (low preheat and high  $\lambda$ ) that has different flame parameters also consistent with its larger flame length. In IPM operation the mean and standard deviation of the time delays due to velocity fluctuations at the burner exit ( $\tau^*$  and  $\sigma^*$ , columns 7 and 8), as expected, are slightly smaller than their respective values obtained from equivalence ratio fluctuations ( $\tau_\phi^*$  and  $\sigma_\phi^*$ , columns 9 and 10). This is because the equivalence ratio fluctuations commence from the position of fuel injectors which are located upstream of the burner exit plane.

In PPM operation the interaction index ( $n$ ) which gives the coupling between the flame and acoustics, should tend to a value equal to the temperature ratio across the flame in the low frequency limit as per Eqn. 2.87. i.e.,  $n^* = 1$ . But from the table we find that this value is more than unity for almost all the operating points. This excess value in the interaction index can be attributed to the error function in assuming the flame shape to take a Gaussian distribution with mean and standard deviation (see section 2.5.4). As the area under the integral of Gaussian curve should be equal to one, the clipped area has to be accounted with some multiplication factor. This multiplication factor is assumed to be included in the value of  $n^*$  and hence its value becomes larger than one. Here only a qualitative treatment of the interaction index is discussed and more on this will be presented in chapter 5 where it is shown how the value of interaction index scales depending on the values of  $\tau$  and  $\sigma$  for several operating points.

## 4.8 Network model validation

The 1-D acoustic network model presented in section 2.7 (see Fig. 2.3) has been verified in two steps. First its principal capability to reproduce the experimental data without flame is carried out. Here the valid  $l_{eff} - \zeta$  model for the burner presented in section 4.2 has been implemented into the net-

work model. Now simulating the experiment, the acoustic forcing at the upstream and/or downstream end can be made using the speaker element. The response to this forcing at a location corresponding to one of the microphone positions in the experiment can be obtained.

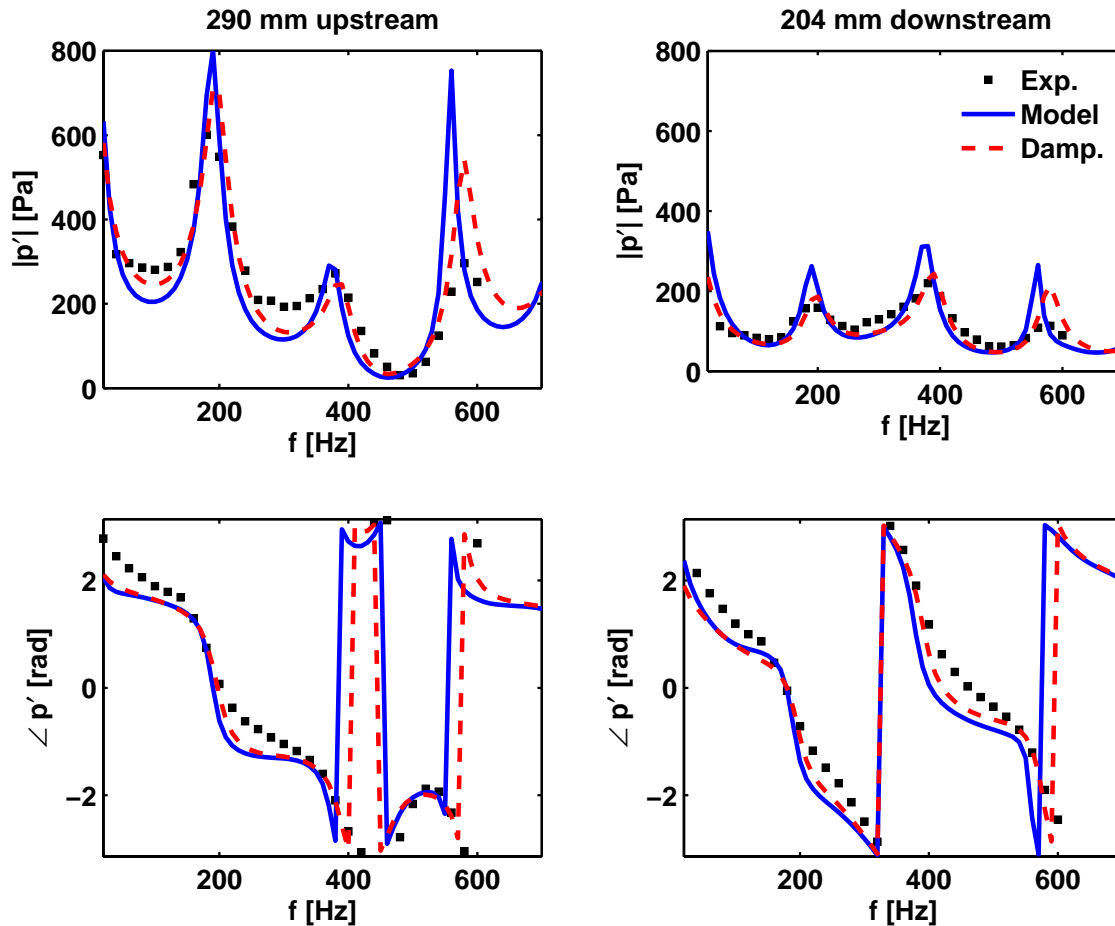


**Figure 4.21:** Comparison of the measured and simulated pressure spectrum upstream (290 mm) and downstream (204 mm) of the burner exit plane *without* combustion

The measured and simulated pressure spectrum for the case with upstream excitation and without combustion are plotted in Fig. 4.21. On the left side the amplitude (top) and phase (bottom) values correspond to a microphone position at 290 mm upstream of the burner, while on the right side correspond to a microphone location at 204 mm downstream. The spectra are in very good agreement both in amplitude and phase for almost the entire frequency

domain. The amplitudes measured in the upstream (plenum) side are larger than in the downstream (combustion chamber) which is due to large acoustic losses introduced by the burner. This is also well captured by the model. Especially the measured peaks from both microphone locations correspond very well with the simulation. To have a suitable acoustic boundary condition the experimentally determined reflection coefficient as a function of frequency has been provided to the network model. By doing so, the predictions were improved especially in the low frequency domain (<100 Hz). Some discrepancies can be seen at the resonance frequencies where the model has over predicted the amplitude due to lower damping. This can also be seen from the phase plots where the phase drops more sharply in the simulation compared to a smooth phase drop in the experiments.

To address this issue, the model sensitivity to damping has been checked by implementing the damped ducts as discussed in section 2.2.2. Apart from losses at burner and area changes additional losses due to visco-thermal damping of acoustic waves in plain ducts has been implemented [63] in the same network model. The simulated pressure spectra with damping included are shown with broken lines in the same plot (Fig. 4.21). A closer agreement with measured amplitudes, particularly, at the resonance frequencies was obtained. The value of the damping coefficient ( $C_d = 2.0$ ) has been chosen such that a best fit is obtained with the measured data. Although the improvements seems to be minor in the case without combustion, these will become very obvious with combustion.

Next, the flame element represented by  $n-\tau-\sigma$  model ( see section 2.5.4) is included into the network model. The same validation procedure as in the case without flame was carried out. The measured and simulated pressure spectra corresponding to the two microphone locations are plotted over the frequency domain as shown in Fig. 4.22. Once more a very good comparison has been obtained between the measurements and the simulation. Again, the results with damping have shown a significant improvement in the predictions especially at eigenfrequencies of the rig. This can also be observed in the phase plots where a sharp drop in phase occurs without damping, whereas it follows the measurements closely in the case with damping around 400 Hz in the

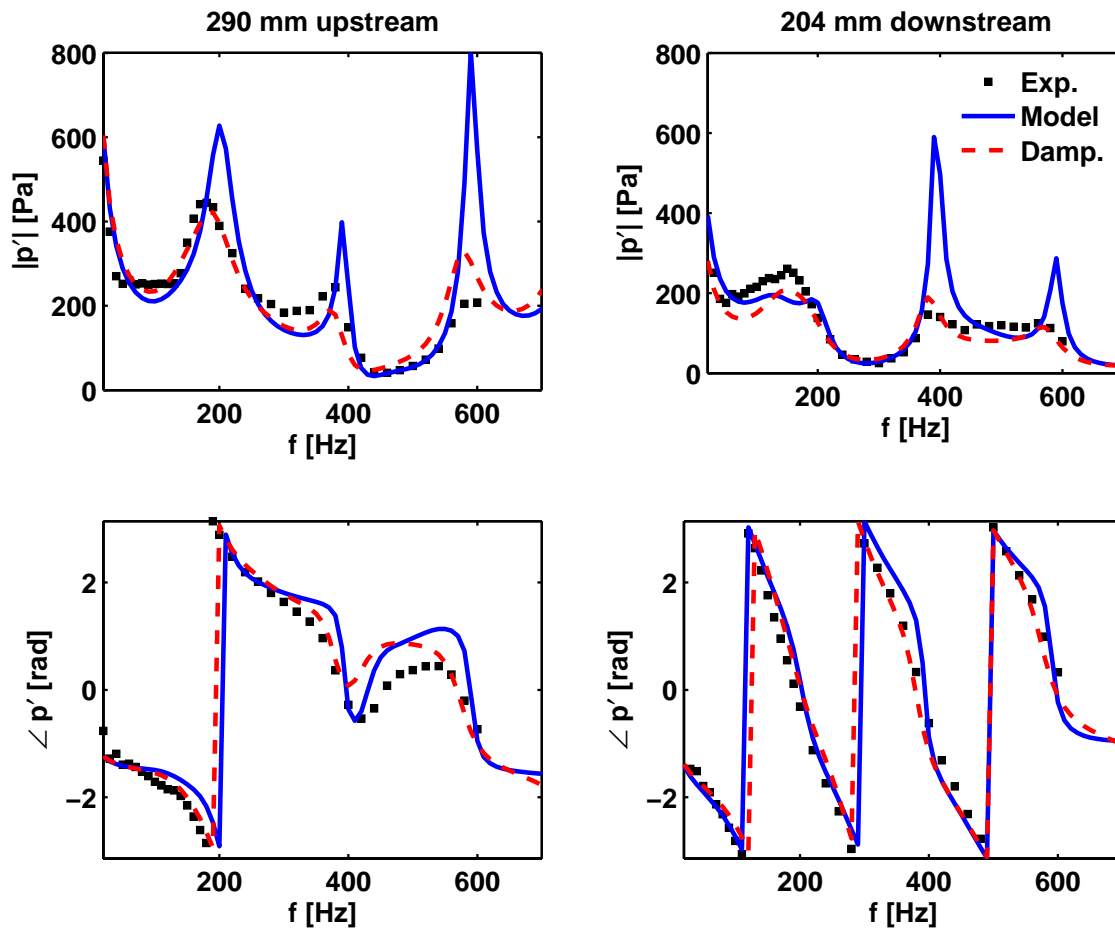


**Figure 4.22:** Comparison of the measured and simulated pressure spectrum upstream (290 mm) and downstream (204 mm) of the burner exit plane *with* combustion

downstream side. The value of damping coefficient  $C_d = 15$  is observed to give the best fit to the measurements with flame. Usually the value of the damping coefficients are small ( $C_d \approx 1$ ). But, as in this case  $C_d = 15$  indicates that some other source (s) of damping exists that is (are) not known. The network model has performed even better in the presence of combustion compared to the case without combustion. In particular, in the downstream side with relatively higher temperatures and thus a higher Mach number, the model has shown a very good agreement with the measurements. This is because with increase in the temperature the acoustic boundary layer thickness increases ( $\delta_{ac} > \delta_l$ , see section 2.2.2) which increases the damping linearly [63, 79].

## 4.9 Model based regression method

Here a method/principle to determine the FTM with only one test state by using a network model based regression (MBRM) with free parameters is presented. This method is very much useful in complex geometries like annular test rig where it is very difficult to achieve two acoustically independent test states for measuring the burner and flame transfer matrices directly. The procedure is explained schematically in Fig. 4.23.

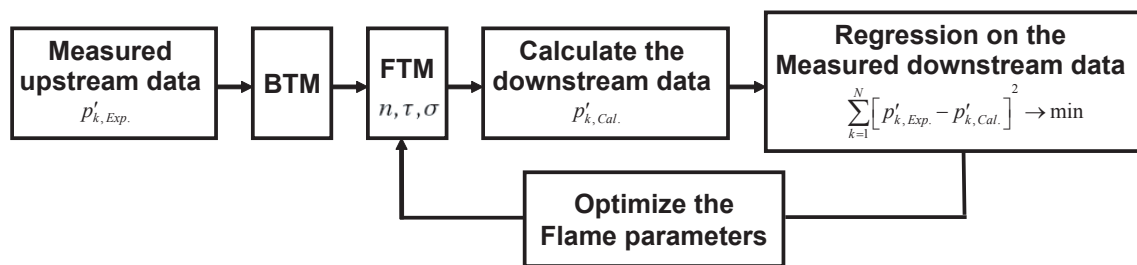


**Figure 4.23:** Model based regression method (MBRM) to determine the flame parameters from only one measurement

A measurement with upstream excitation is carried out with a row of microphones positioned upstream and downstream. From the 1-D acoustic theory  $p'_u, u'_u$  are obtained at a chosen reference plane using the measured pressures at several locations (e.g. from the MMM). The data is then multiplied with the known BTM and FTM model to calculate the pressure and velocity field downstream ( $p'_d, u'_d$ ). With this a regression analysis is performed to match the measured downstream data for several frequencies, such that the error is minimized. Finally, the optimized flame parameters are obtained. This procedure can also be applied in other direction and also with downstream excitation.

The results obtained with this procedure at 60kW/1.7/300°C with upstream excitation are plotted in Fig. 4.24. The amplitude (top) and phase (bottom) values of the  $T_{22}$  element of the FTM obtained from the MBRM (solid line) are compared with those of the MMM (black squares). The left side of the plot corresponds to upstream excitation, making the fit to downstream microphone data and then using regression to deduce the optimized flame parameters. On the right side, the downstream measured data is used to calculate the up-

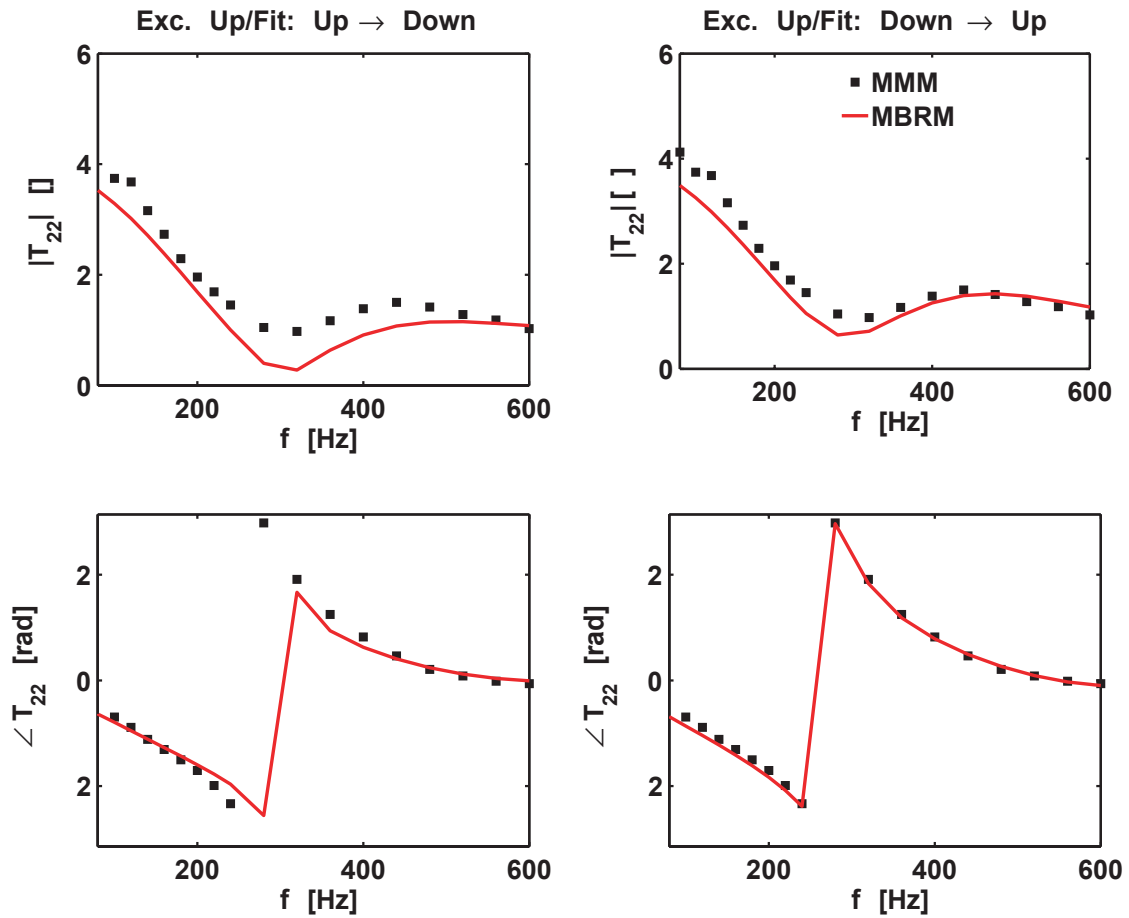


**Figure 4.24:** Comparison of the FTM obtained with the direct MMM and the MBRM with **upstream** excitation. Left side: Regression made to match the downstream data. Right side: Regression made to match the upstream data

stream pressure data and then make regression to fit the measured upstream data to get the optimized flame parameters. The latter works better as the amplitudes on the forcing side are higher. As a consequence, performing a regression on that side yields a better results as can be seen in the plot.

The same procedure was also applied with downstream excitation as shown in Fig. 4.25. Once again a very good consistency between the model based regression procedure and the directly measured FTM is obtained. As compared to the results from the downstream excitation, the upstream excitation results yielded superior agreement with the direct method. This can be attributed to

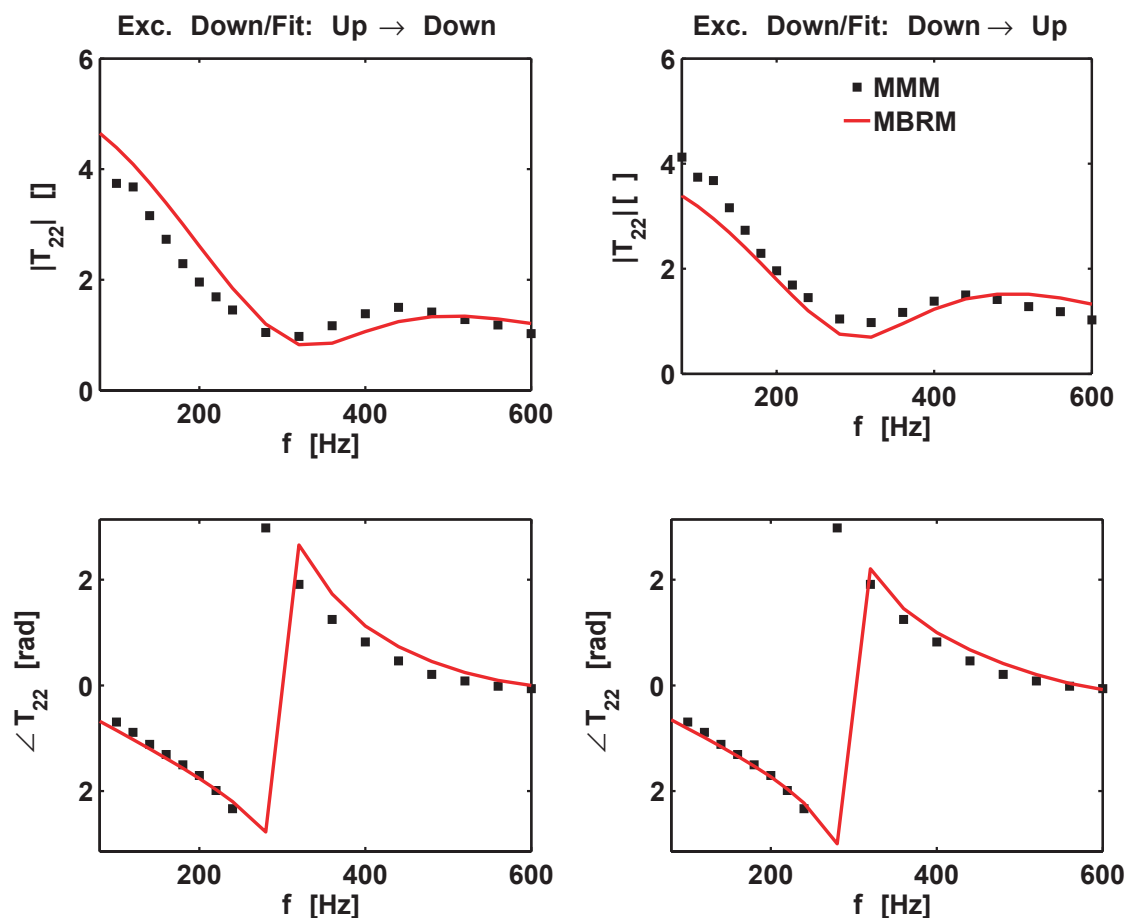


**Figure 4.25:** Comparison of the FTM obtained with the direct MMM and the MBRM with **downstream** excitation. Left side: Regression made to match the downstream data. Right side: Regression made to match the upstream data

the fact that the second siren excitation from downstream end has a lower excitation level than the upstream siren. Nevertheless, a good agreement between both methods demonstrate the potential advantage of the model based method to obtain the dynamic flame parameters with only one measurement, i.e. forcing only at one end. A similar analysis can be made even to obtain the optimized BTM parameters ( $l_{eff}, \zeta$ ) without flame.

Finally, a comparison is made between the flame parameters determined at an operating point of 50/1.7/300°C using direct and model based regression methods as shown in table 4.2. The first row corresponds to the flame param-

eters determined from the  $n - \tau - \sigma$  model fit on to the directly measured FTM (i.e., using MMM as presented in table 4.1). Remaining all other rows shows the flame parameters deduced from the MBRM. The data is shown for all the combinations using up- and downstream excitation and their corresponding regression analysis.

**Table 4.2:** Summary of mean and standard deviation of the convective time delays obtained using direct MMM and MBRM at 50/1.7/300°C. The values are normalized as  $\tau^* = \tau \cdot \frac{U}{D}$ ;  $n^* = n / (T_h / T_c - 1)$

Method	PPM			IPM				
	$n^*$	$\tau^*$	$\sigma^*$	$n^*$	$\tau^*$	$\sigma^*$	$\tau_\phi^*$	$\sigma_\phi^*$
Direct (MMM)	1.39	0.93	0.29	1.53	0.69	0.29	1.44	0.41
MBRM: Exc.Up/Fit:Up->Down	1.56	0.86	0.39	2.13	2.51	0.55	1.49	0.35
MBRM: Exc.Up/Fit:Down->Up	1.64	0.97	0.33	4.77	0.98	0.85	1.47	0.41
MBRM: Exc.Down/Fit:Up->Down	1.35	0.96	0.30	2.31	264	46.74	16.02	308.7
MBRM: Exc.Down/Fit:Down->Up	1.49	0.99	0.31	1.53	0.64	0.20	1.63	0.245

The results indicate a very good overall consistency with each other method in the PPM operation. Whereas, in the case of IPM operation large deviations from the direct method (MMM) and against each other methods in MBRM can be observed. This can be due to the fact with increased number of free parameters (up to 5) the performance of the fit function is low and sometimes even delivers unphysical values for these parameters (e.g. row six). This problem can be solved by using more robust algorithm with user interface, where some physical constrains based on experience can be implemented to obtain the optimized flame parameters.

## 4.10 PIV results

The cold and hot mean velocity flow field measurements using PIV were carried out on both single and annular test rig configurations<sup>2</sup>. The primary mo-

<sup>2</sup>As mentioned in chapter 1 the author has investigated the EV5 burner in an annular test rig as well. For more information on the annular test rig investigation the reader is referred to Fanaca et. al. [20,21], Kunze, 2004 [43].

tivation was to address the differences observed in the dynamic flame characteristics for a similar operating point in both the configurations. Furthermore, the PIV results can be used to determine the flow angle and velocity profiles which feed into developing scaling rules presented in chapter 5. First the results concerned with the single burner test rig will be presented. The PIV setup details were discussed in section 3.2.4.

#### 4.10.1 Cold flow field

The result of the PIV measurement in the single burner test rig for a mass flow rate of 35 g/s is shown in Fig. 4.26.

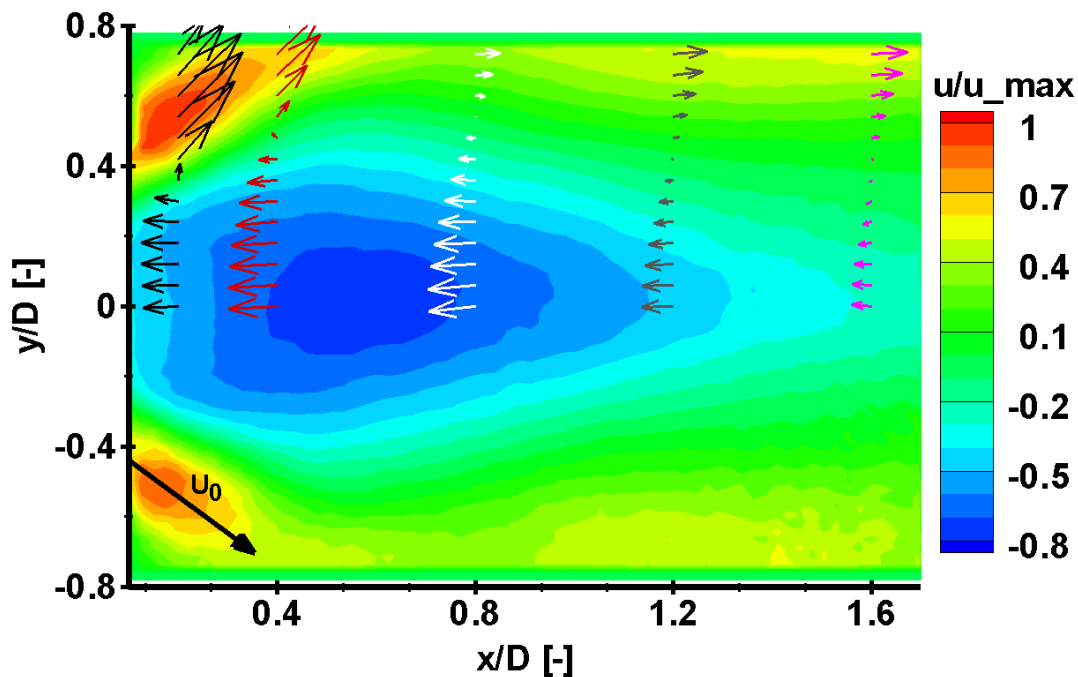


**Figure 4.26:** Contour of the mean axial velocity in the meridional plane of the combustion chamber for an isothermal flow (35 g/s). The vectors on the top half side of the plot represent the amplitude velocities at five selected cross sectional planes. The arrow on the bottom corner of the plot indicates the direction of the jet center line velocity exiting from the annulus of the EV5 burner

The colored contours show the axial velocity flow field. It can be seen that the

recirculation velocity reaches about 65% of the peak jet velocity exiting from the burner. The flow jet half angle is  $50^\circ$  and the inner recirculation zone (IRZ) width is almost  $0.8D$  with a length of  $1.8D$ . The flow field in the combustor exhibits a wall jet regime, where the flow immediately attaches to the wall with a small corner recirculation zone (CRZ). These findings are very much in agreement with Fu. et. al. 2005 [27], who have demonstrated that the occurrence of this regime depends on the degree of confinement seen by the swirling jet, i.e. the area ratio between the combustor and burner exit  $A_{cc}/A_b$ . According to their experiments a wall jet regime exists for a flow with effective swirl number of 0.45, if the area ratio is below a critical confinement value of 5.88. Fanaca et. al. 2009, [21] showed how to generalize the findings of Fu. et. al. 2005 [27] for other swirl numbers.

PIV measurements have also been made to investigate the mean flow field behavior in the presence of combustion. Here, an attempt to cross check the PIV measurements will be presented. The procedure developed will be first demonstrated using the isothermal measurements.

In Fig. 4.27 the axial velocity profiles ( $u_x(r)$ ) for a mass flow rate of 35 g/s as a function of radial distance at several axial cross sectional planes ( $x/D$ ) are shown. The profiles were extrapolated to the wall. Axial symmetry in the flow field is assumed and only the top half of the velocity field is considered (see Fig. 4.26). Now, the mass flow rate ( $\dot{m}_{PIV}$ ) in a given cross sectional plane can be obtained by performing an integration over the entire cross sectional area using the measured axial velocity profiles as follows:

$$\dot{m}_{PIV} = 2\pi \int_{r=0}^{r=r_o} \rho r u_x(r) dr \quad (4.9)$$

Although a square combustor is used, an equivalent circular cross-sectional area with outer radius  $r_o$  has been used for performing the integration. The result can then be compared with the total mass flow rate actually supplied ( $\dot{m}_{total}$ ). From continuity both must be the same at every cross sectional plane. The comparison is shown in table 4.3. At the axial location  $x/D = 0.2$  very close to the burner exit, where a jet like structure exists, about 93% of mass flow rate is reproduced using the PIV data. However, in the cross sec-

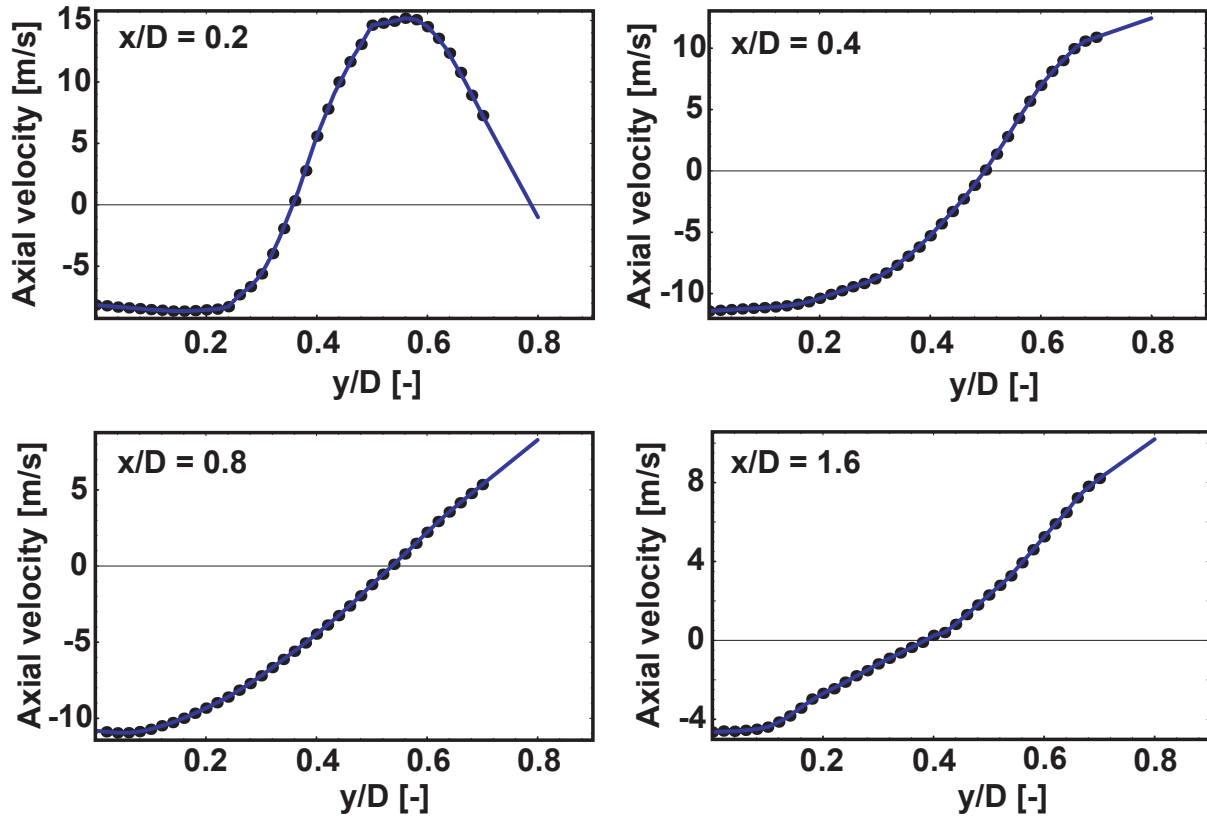


**Figure 4.27:** Axial velocity profiles for calculating the integrated mass flow rate at several axial locations. The dots represent the data from PIV for a mass flow rate of 35 g/s and solid line its corresponding interpolation function

tional plane  $x/D = 0.8$  where the flow expands rigorously and reattaches to the combustor walls, most of the forward flow is near the walls leading to underestimation of the mass flow rates. This is because the PIV data is not available closer to the walls (up to 5 mm) and hence poor results are obtained by extrapolating the data towards that region. Moving further downstream to  $x/D = 1.6$ , the flow reflects from the walls making it more uniformly distributed over entire cross-sectional plane and hence the integrated mass flow reaches about 97% of the total mass flow rate.

Thus, it can be concluded that PIV measurements can be verified from the above procedure in the case of isothermal flow field. The same procedure is now applied to analyze the PIV data in presence of combustion and the com-

**Table 4.3:** Comparison of the mas flow rates obtained using PIV measurements in the isothermal flow field at several axial cross sectional planes

$x/D$	0.2	0.4	0.8	1.2	1.6
$\dot{m}_{PIV}/\dot{m}_{total}$	0.93	0.81	0.27	0.78	0.97

parison is shown in table 4.4.

**Table 4.4:** Comparison of the mas flow rates obtained using PIV measurements in the hot flow field at several axial cross sectional planes

$x/D$	0.2	0.4	0.8	1.2	1.6
$\dot{m}_{PIV}/\dot{m}_{total}$	0.16	0.17	0.37	0.57	0.72

The results showed rather a poor comparison. This is because with combustion two major problems occurred. Firstly, due to rapid hot jet expansion the flow attaches immediately to the walls of the burner front panel with a very small CRZ (wall jet regime). This makes the PIV measurements even more difficult with the restricted field of view and increased laser light sheet reflections from the walls. Thus, the measured PIV data was not satisfactory. Secondly, we need an appropriate temperature/density distribution as a function of the radial and the axial distance in order to apply Eqn. 4.9 which is difficult to obtain. Nevertheless, a qualitative check can be obtained with a rather crude assumption of uniform temperature profiles as a function of the axial distance. By doing so, only the results corresponding to far downstream locations ( $x/D > 1.6$ ) with fairly uniform temperature distribution have shown a better comparison.

#### 4.10.2 Cold and hot flow field comparison

The goal of this section is to develop a relation between the cold and hot jet centerline velocity of the flow field exiting from the annulus of the EV5 burner. This is achieved by expressing the hot jet center line velocity as a function of temperature ratio across the flame and cold jet velocity. Later, this relation is

useful in deriving the expression for convective time delay ( $\tau$ ) as will be discussed in chapter 5.

As pointed out in previous section the PIV measurements with combustion in the single burner test rig were not satisfactory. As they were more consistent PIV measurements made in the annular test rig were used for this purpose. The results obtained there indicated a free jet regime [21]. A simple approach to understand the complex flow behavior is used to develop the scaling rules (e.g. to see how the convective time delay ( $\tau$ ) scales with the burner exit velocity in presence of combustion). For this purpose a comparison of the cold and hot<sup>3</sup> jet center line velocities ( $U_0(x)$ ) is plotted along the x-axis as shown in Fig. 4.28. The values of  $U_0(x)$  are obtained by searching the trajectory of maximum resultant velocity ( $\sqrt{u^2 + v^2}$ ) from the PIV data as shown in Fig. 4.26. The  $U_0$  is normalized with the absolute burner exit velocity  $U_b$  also obtained from the PIV data.

The axial distance  $x$  is normalized with the effective diameter of the jet, which in this case was taken as the hydraulic diameter  $D_{hyd}$  of the jet exiting from the annulus of the EV5 burner<sup>4</sup>. This normalization helps in comparing the velocity profiles with that of a turbulent round jet decay behavior. As expected, the velocity profiles close to the burner exit are observed to be similar for both cold and hot cases. In the cold case it shows a typical free jet behavior with a constant magnitude up to a core axial distance of  $x_{0,c}/D_{hyd} = 1.85$  and then the magnitude decreases as the jet spreads along the axial distance. The same behavior is also observed in the hot case, but the core axial distance  $x_{0,h}/D_{hyd} = 3.42$  is 80% larger than in the cold case. This is because in presence of combustion the jet momentum ratio is high against the hot environment and hence a greater penetration with increasing velocity. The offset between these two points is observed to be  $\approx \sqrt{T_h/2/T_c}$  as shown in the figure<sup>5</sup>. After this core distance, the classical jet decay behaviour can be observed from the plot for both the cases.

---

<sup>3</sup>The mass flow rate (32 g/s) and thermal power (73kW/1.3/no preheat) are calculated per burner assuming a equal flow distribution among the twelve burners in the annular combustion chamber

<sup>4</sup>This is equal to the difference in the outer and inner diameter of the annulus formed by the forward and aerodynamically stabilized recirculated flow.  $D_{hyd} = D(1 - \sqrt{0.6}) = 11.3$  mm

<sup>5</sup>With  $T_h = 1700K$ ,  $T_c = 291K$  the offset is observed to be  $\approx 1.7$

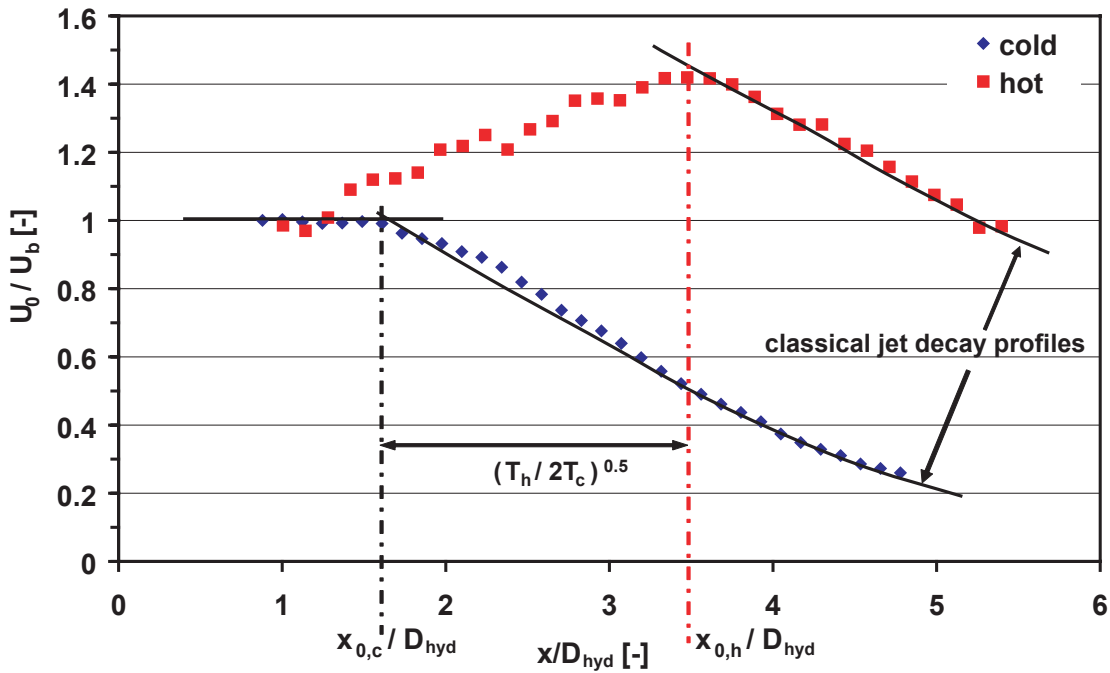


**Figure 4.28:** Comparison of the cold and hot jet center line velocity profiles along the  $x$ -axis

It can be observed from the plot (see Fig. 4.28) that the hot jet centerline velocity increases almost linearly from the burner vicinity ( $x/D_{hyd} = 1.27$ ) to its core distance ( $x/D_{hyd} = 3.48$ ). The convective time delay is depended on the mean velocity of the jet exiting from the burner. Due to the jet expanding into a hot environment, an expression for representing the jet effective velocity can be derived. This is obtained by assuming a linear increase of the jet velocity from the burner exit plane ( $U_{0,c}$ ) to the point of maximum heat release  $U_{0,h}$ . Fig. 4.29 shows the schematic representation of the jet centerline velocity being increased linearly from  $x_1, U_1$  to  $x_2, U_2$ . The  $U_{eff}$  represents the average or effective jet centerline velocity. Here for simplicity of notation it is taken as  $U_1 = U_{0,c}$  and  $U_2 = U_{0,h}$ .

An expression to represent the jet velocity as a function of axial distance can be obtained (from the Fig. 4.29) as

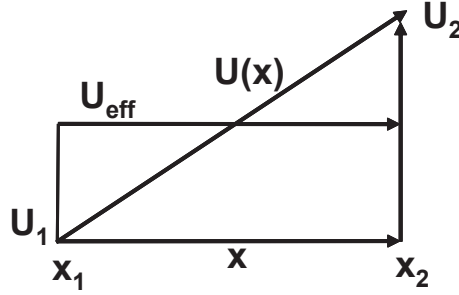


**Figure 4.29:** Effective jet centerline velocity in presence of combustion

$$U(x) = U_1 + \frac{U_2 - U_1}{x_2 - x_1}(x - x_1). \quad (4.10)$$

Integrating the Eqn. 4.10 throughout and dividing by  $U_1$  yields an expression for effective velocity as

$$\begin{aligned} \frac{U_{\text{eff}}}{U_1} &= \frac{1}{x_2 - x_1} \int_{x_1}^{x_2} 1 + \left( \frac{U_2}{U_1} - 1 \right) \frac{x - x_1}{(x_2 - x_1)} dx \\ &= 1 + \frac{1}{2} \left( \frac{U_2}{U_1} - 1 \right). \end{aligned} \quad (4.11)$$

Assuming a linear dependency of the jet expansion on the temperature ratio across the flame with a proportionality constant  $C$  we get

$$\frac{U_2}{U_1} = 1 + C \left( \frac{T_h}{T_c} - 1 \right). \quad (4.12)$$

The value of the  $C = 0.08$  is obtained from the PIV data presented in Fig. 4.29. Now, substituting the Eqn. 4.12 into Eqn. 4.11 and from  $U_{0,c} = U_1$  we get

$$\frac{U_{\text{eff}}}{U_{0,c}} = \left[ 1 + \frac{C}{2} \left( \frac{T_h}{T_c} - 1 \right) \right]. \quad (4.13)$$

The above relation will be useful to obtain the convective time delays as a function of the axial distance, the axial jet velocity and the temperature ra-

tio across the flame. It can be concluded from the above analysis that the PIV data was useful for the understanding of the flow field geometry, particularly, the flow angle and to derive simplified correlations which are further used in developing scaling rules as will be discussed in chapter 5.

## 5 Scaling Rules

The stability analysis of a combustion system may be performed using the acoustic network model and a generalized Nyquist criterion based *open loop gain method* (OLG). As part of the research project (KW-21, GV4) the OLG method was applied to perform a detailed stability analysis of the annular test rig [20, 21, 43] at various operating conditions e.g. varying thermal power, air excess ratio and preheat temperatures [88]. Accordingly, the flame transfer functions, described by their flame parameters ( $n, \tau, \sigma, \tau_\phi, \sigma_\phi$ ), are a prerequisite to represent the flame behavior at several operating points. In this chapter some scaling rules are given that were used to calculate these flame parameters at other operating points starting from a known operating point.

### 5.1 Flame length model

The flame length model is developed basically as a function of thermal load, air excess ratio ratio  $\lambda$ , mixture preheat temperature and flame geometry. An earlier investigation [33] had shown that the mean convective time delays can be computed from a simplified heat release profile exiting from a typical swirl burner. A schematic of the simplified geometric flame length model is shown in Fig. 5.1.

The figure shows the meridional plane of the flow field with a flow jet half angle  $\alpha_0$  and mean radius  $r_0 = (r_i + r_o)/2$ . It is assumed that the flame front has a conical shell surface and anchors at the inner radius ( $r_i$ ) of the annular burner exit. The annulus could be formed also by the recirculation bubble, e.g. with the EV5 burner. Given the recirculation of hot combustion products in the inner recirculation zone the flame ignites in the shear layer between the inner recirculation zone and the cold reactant jet. Also, no reaction is assumed in

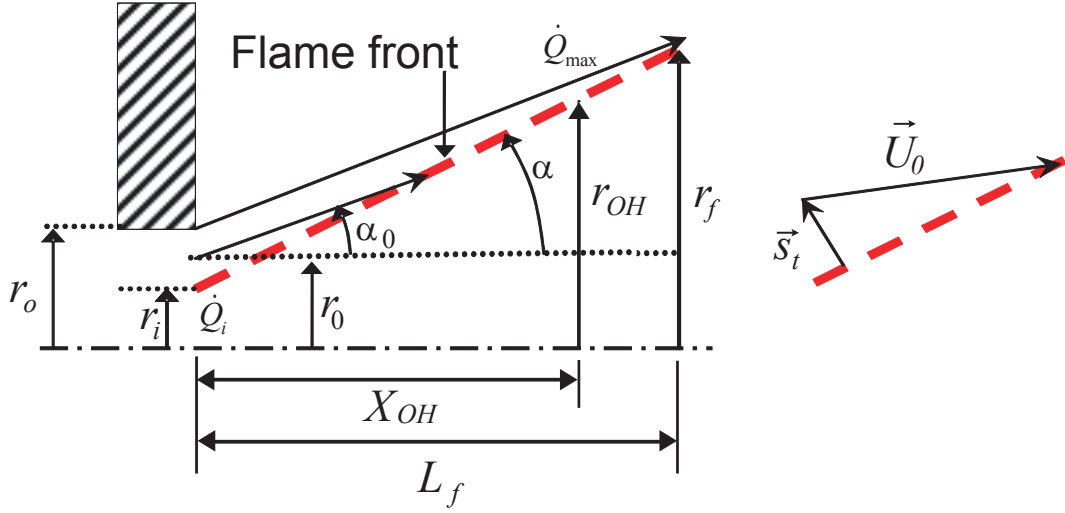


**Figure 5.1:** Schematic of the flame length model

the outer recirculation zone where large heat losses to the walls of the combustor are expected. Due to the high jet velocity the flame front then extends almost tangentially to the streamlines, in the diverging flow field, until the jet velocity has decayed enough to allow steeper angles of the turbulent flame front [33]. Consequently, the flame angle,  $\alpha$  is slightly larger than the flow jet angle. It is represented as  $\alpha = \alpha_0 + \arcsin(s_t/U_0)$  with  $s_t$  the turbulent flame speed and  $U_0$  the nominal jet velocity. The  $L_f$  represents the flame length. From the continuity equation one can relate  $A_0 U_0 = s_t A_f$  between the burner exit and the flame front. Thus the geometric flame length can be obtained after some trigonometry (see Appendix A.2 for derivation) as

$$L_f = \sqrt{\frac{A_0 U_0}{s_t} \frac{\cos \alpha}{\pi \tan \alpha} + \frac{r_i^2}{\tan^2 \alpha}} - \frac{r_i}{\tan \alpha} \quad (5.1)$$

with  $A_0 = \pi \cdot (r_o^2 - r_i^2)$  the effective burner exit area. The turbulent flame speed  $s_t$ , is obtained from the model given by Schmid et al. 1998 [86] as follows:

$$s_t = s_l + u' \cdot (1 + Da_t^{-2})^{-0.25} \quad (5.2)$$

$$Da_t = 0.09 \frac{l_t}{u'} \cdot \frac{s_l^2}{\nu} \quad (5.3)$$

Here  $Da_t$  is the Damköhler number with the turbulent length scale  $l_t$  and the RMS value  $u'$  of the fluctuating velocity,  $s_l$  the laminar flame speed and  $\nu$  the kinematic viscosity. The laminar flame speed is calculated from the correlation proposed by Peters [64]. The turbulent quantities are obtained based on the investigation from Wäsle et al. 2005 [99] as

$$u' = 0.15 \cdot U_0 \cdot \frac{0.8 D_{hyd}}{L} \quad (5.4)$$

and

$$l_t = D_{hyd} \left( 0.002 + 0.005 \cdot \frac{L}{D_{hyd}} \right). \quad (5.5)$$

Here  $D_{hyd} = 2 \cdot (r_o - r_i)$  represents the hydraulic diameter of the annular jet and  $L$  is a representative distance from the burner exit to the place of maximum heat release, which is typically around  $L = 0.66 L_f$  for a swirl stabilized flame [99]. Now by substituting Eqns. 5.2, 5.4 and 5.5 into Eqn. 5.1 we get the desired geometric flame length. The flame lengths calculated with this simplified approach are in good agreement with the measured flame lengths (discussed in next section).

### Improved flame length model:

An attempt has been made to improve this simplified geometric flame length model by taking into account additional parameters which influence the flame structure and flame operating regime. Several authors have performed detailed studies on the highly turbulent premixed flames, e.g. Borghi, 1985, Peters, 1999, Griebel et al. 2003 and Siewert, 2006 [5, 29, 65, 94] to name a few. As a result of all these investigations it can be concluded that the complex interaction between the turbulent flow field and the flame front and resulting flame front structure can be fairly well represented by means of characteristic dimensionless numbers. These are, in addition to turbulent Damköhler number  $Da_t$ , the turbulent Reynolds number  $Re_t = u' \cdot l_t / \nu$  and the Karlovitz number  $Ka = (l_t / \delta_l)^{-0.5} (u' / s_l)^{1.5} = \sqrt{Re_t} / Da_t$ .  $\delta_l$  is the laminar flame thickness. The  $Re_t$  takes into account the influence of the turbulence on the development of the shear layer thickness downstream of the flame holder. The Karlovitz number can be used as a measure of the flame front stretch or corrugation which influences the turbulent flame speed. It is observed from these

investigations that with increasing  $Re_t$  and  $Ka$  the flame front is increasingly corrugated causing local extinctions in the flame. Peters [66] suggests that for  $Ka > 100$  the turbulent premixed flame structures change significantly and even extinguish<sup>1</sup>. As a consequence, these characteristic parameters are included into the geometric flame length model (Eqn. 5.1) to predict the flame lengths (which are based on flame structure) more appropriately. The modified flame length ( $L_f^*$ ) model is obtained as

$$\frac{L_f^*}{D_{hyd}} = 0.247 \cdot \frac{L_f}{D_{hyd}} \cdot Re_t^{0.2} \cdot Ka^{0.076}. \quad (5.6)$$

The modified flame length  $L_f^*$  is normalized with hydraulic diameter  $D_{hyd}$ . The constant factor (0.247) and the exponential coefficients (0.2, 0.076) of the model parameters  $Re_t, Ka$  in Eqn. 5.6 are obtained by a fit to the measured flame lengths at several operating points as will be discussed in the following section.

## 5.2 Flame length comparison

The experimental flame lengths are obtained on the single burner test rig by varying thermal power and  $\lambda$  at two preheat temperatures. A comparison between the flame lengths obtained from measured OH\*–chemiluminescence images and model (Eqn. 5.6) are presented in Figs. 5.2 and 5.3 for 200°C and 300°C air preheat temperatures, respectively.

From the plots we see an excellent agreement between the measurements and modelled flame lengths demonstrating the capability of the model to reproduce the experimental data at several operating points. The trend observed in the experiments is very well captured even with different preheating temperatures. The deviations from the experimental values (relative error) were observed to be around 5% in the case of 300°C air preheat and around 7% in

<sup>1</sup>Typically the flames in the stationary gas turbines are characterized by high  $Re_t > 10^3$ ,  $Da_t > 1$  and  $10 < Ka < 100$ . Therefore these flames belong to the “thin reaction zones” in the Borghi diagram [5]

## 5.2 Flame length comparison

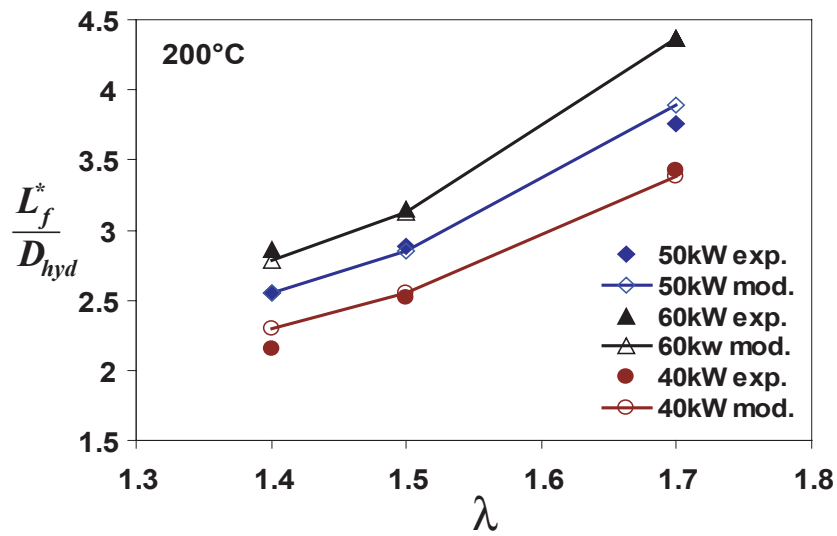


**Figure 5.2:** Comparison of flame lengths at various operating points with air preheating of 200°C in PPM operation

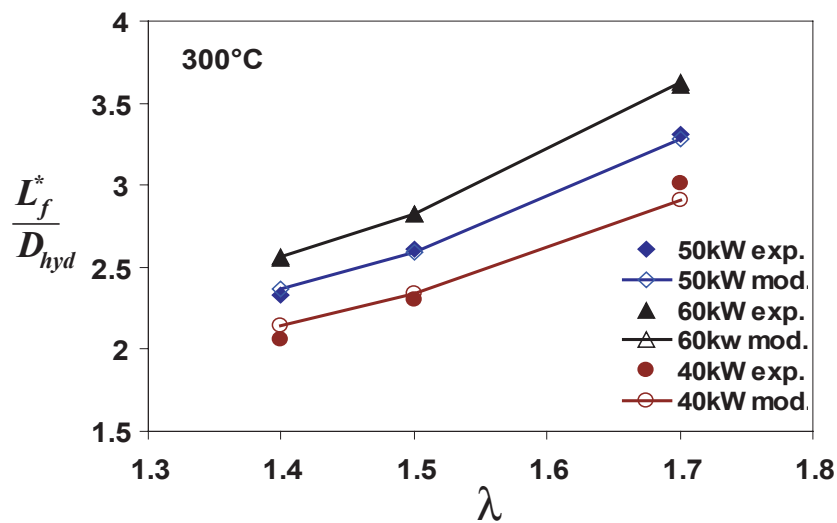


**Figure 5.3:** Comparison of flame lengths at various operating points with air preheating of 300°C in PPM operation

the case of 200°C air preheat. The relative error approximation ( $e$ ) is defined as

$$e = \frac{\sqrt{\sum (L_{mod} - L_{exp})^2}}{\sum L_{exp}}. \quad (5.7)$$

The sensitivity of the model on  $Re_t$  and  $Ka$  has also been verified by neglecting these terms in Eqn. 5.6 (results not shown using this model, i.e., Eqn. 5.1). A similar validation procedure has been implemented. The results indicated a fairly good agreement between measured and predicted flame lengths with a relative error approximation below 8% in the case of 300°C air preheat. But, in the case with lower preheating (200°C), the trend observed in the experiments has not been reproduced well with the model, leading to a relative error approximation up to 14%. This can be due to the fact that with lower preheating the flame structure and correspondingly the flame lengths have changed significantly. These changes may not be captured well by the simplified model (Eqn. 5.1) without the parameters  $Re_t$  and  $Ka$ . Hence, from the above analysis it is understood that the modelling should take the influence of the parameters  $Re_t$  and  $Ka$  into account for a better prediction of the flame lengths covering more operating points.

### 5.3 Scaling of flame parameters

Following the work by Hirsch et al. 2005 [33] and Russ et al. 2007 [80] the mean convective time delay is directly proportional to the ratio of the distance at which the highest reaction occurs and the effective burner exit velocity. Once we have the suitable flame length model (Eqn. 5.6) and combining with the Eqn. 4.13 the mean time delay  $\tau$ , can be obtained as

$$\tau = C_\tau \left[ \frac{L_f^*}{U_{0,c}} \left[ 1 + \frac{C}{2} \left( \frac{T_h}{T_c} - 1 \right) \right]^{-1} \right]. \quad (5.8)$$

Here, the influence of volume expansion due to combustion as a function of temperature ratio across the flame is included according to the Eqn. 4.13. The proportionality factor  $C_\tau = 1.5$  and coefficient  $C = 0.08$  are fixed (calibrated)

by comparing the predicted time delay with that of a measured time delay at a chosen reference operating point (50kW/1.7/300). The temperature in the combustion chamber  $T_h$  is calculated after taking into account appropriate heat losses due to cooling.  $T_c$  is the mixture preheat temperature. Once the model coefficients are fixed, the time delays can be calculated (scaled) at several operating points as a function of thermal power,  $\lambda$  and preheat temperatures.

Next task is to derive an expression for  $\sigma$  as a function of  $\tau$  and flame geometry. Recalling the heat release distribution as discussed in section 2.5.4, the heat release is assumed to take a Gaussian form (probability density function) with mean convective time delay ( $\tau$ ) and standard deviation ( $\sigma$ ). Applying the Eqn. 2.82 to represent the heat release distribution, the values of the heat release rate as a function of time for a given  $\tau$  and  $\sigma$  values can be obtained. Thus, the value of heat release rate ( $\dot{Q}_i$ ) at inner radius  $r_i$ , where the flame anchors, can be obtained by substituting the time  $t = 0$ . Similarly, the maximum heat release rate ( $\dot{Q}_{max}$ ) is acquired by substituting  $t = \tau$  in Eqn. 2.82. Taking the ratio of both the terms yields

$$\frac{\dot{Q}_i}{\dot{Q}_{max}} = e^{-\frac{1}{2} \frac{(-\tau)^2}{\sigma^2}}. \quad (5.9)$$

It was proven in the previous section that the simple geometric flame length model with conical flame shape was successful in predicting the flame lengths at several operating points. With the same analogy, (see Fig. 5.1) the heat release can be assumed to increase linearly from  $\dot{Q}_i$  at inner radius  $r_i$  to  $\dot{Q}_{max}$  at radius  $r_{OH}$ . This assumption can be justified as the turbulent flame speed remains constant, the heat release rate increases with the increase in surface area of the flame ( $Q \propto s_t \cdot A_f$ ). With this assumption and using simple trigonometric relations we get the ratio of heat release between two positions as

$$\frac{\dot{Q}_i}{\dot{Q}_{max}} \approx \frac{r_i}{r_{OH}} \approx \frac{r_i}{r_f} \frac{L_f}{X_{OH}} = \frac{r_i}{(r_i + L_f \cdot \tan \alpha)} \frac{L_f}{X_{OH}}. \quad (5.10)$$

Combining Eqns. 5.9 and 5.10 and rearranging we get an estimate for  $\sigma$  as

$$\sigma = C_\sigma \sqrt{\frac{-\tau^2}{2 \ln \left( \frac{1}{\left(1 + \frac{L_f}{r_i} \tan \alpha\right) \frac{L_f}{X_{OH}}} \right)}} \quad (5.11)$$

with  $C_\sigma = 0.4$  which is an additional factor used to fine tune the model for obtaining a best fit on to the measured  $\sigma$  values. This constant factor may be attributed to the fact that flame shape is approximated with a conical shell (Fig. 5.1) instead of a Gaussian shape (Fig. 2.2).

Finally, a relation to calculate the values of interaction index  $n$  as a function of  $\tau, \sigma$  has to be obtained. It is known from the FTF theory (Eqn. 2.87), in a PPM operation, the amplitude of the FTF should reach unity in the zero frequency limit. This is possible only if the value of  $n = (T_h/T_c - 1)$  is fixed. But looking at the  $n - \tau - \sigma$  model the  $n$  is chosen to be a free parameter since, the model was not able to reproduce the experimental values. As observed from the table 4.1 the values of  $n^* > 1$  indicate that the values of  $n$  were always in excess of its theoretical value. Therefore it is understood that this excess value in  $n$  is simply due to the chosen  $n - \tau - \sigma$  model. Here the problem arises due to the fact that the flame is approximated with a Gaussian distribution (see Fig. 2.2). As the total area under the Gaussian curve should be equal to one, the clipped area (shown with broken lines) has to be accounted with some multiplication factor. This multiplication factor is assumed to be included in the value of  $n$  and hence the value of  $n^*$  becomes larger than one. The multiplication factor can be obtained by integrating the approximated Gaussian function. The error function then gives quantitatively the missing value due to the clipped Gaussian. Let the heat release distribution be represented by Eqn. 2.82. Integrating this equation between the time limits  $t = 0$  where the flame begins to  $t = \tau_{max}$  until the end of the flame (flame length) we get

$$\int_{t=0}^{t=\tau_{max}} \Phi_{\tau, \sigma^2}(t) dt = \frac{1}{\sqrt{2\pi}\sigma} \int_{t=0}^{t=\tau_{max}} e^{-\frac{1}{2} \frac{(t-\tau)^2}{\sigma^2}} dt \quad (5.12)$$

$$= \frac{1}{2} \left( \text{Erf} \left[ \frac{\tau_{max} - \tau}{\sqrt{2}\sigma} \right] + \text{Erf} \left[ \frac{\tau}{\sqrt{2}\sigma} \right] \right). \quad (5.13)$$

From Figs. 5.1 and 2.2 the maximum convective time delay can be approximated as  $\tau_{max} = \tau L_f / X_{OH}$ . Substituting this relation into Eqn. 5.13 yields the desired relation ( $n_c(\tau, \sigma)$ ) for compensating the error in approximating the flame distribution with Gaussian function as

$$n_c(\tau, \sigma) = \frac{1}{\int_{t=0}^{t=\tau_{max}} \Phi_{\tau, \sigma^2}(t)} \quad (5.14)$$

$$= C_n \frac{1}{\frac{1}{2} \left( \text{Erf} \left[ \frac{\tau}{\sigma} \frac{(L_f / X_{OH} - 1)}{\sqrt{2}} \right] + \text{Erf} \left[ \frac{\tau}{\sqrt{2}\sigma} \right] \right)}. \quad (5.15)$$

Once again an additional constant factor  $C_n = 1.36$  has been used in Eqn. 5.15 to fine tune the model so that a best fit to the measured data is obtained. The actual value of interaction index  $n$  can then be obtained by multiplying the  $n_c(\tau, \sigma)$  with the temperature ratio across the flame as

$$n = n_c \cdot \left( \frac{T_h}{T_c} - 1 \right). \quad (5.16)$$

From the above analysis the values of  $n$ ,  $\tau$  and  $\sigma$  can be calculated for geometrically similar flames as a function of flame length, which in turn depends on the thermal power, preheat temperature and  $\lambda$ . A comparison is made between the measured and scaled flame parameters obtained for PPM operation as shown in table 5.1. The overall relative error as defined in Eqn. 5.7 is shown in the last row.

A very good agreement between the measured and scaled flame parameters for almost all the operating points has been obtained. Except in the low preheating case (in particular 50kW/1.7/200CPH) considerable deviation (upto 30%) is observed in the value of  $n$ . The reason for this is, as explained before, at low preheat and high  $\lambda$  value the flame has a different structure compared to the other flames. It can be concluded from this chapter that the overall performance of the scaling rules derived is very satisfactory.

**Table 5.1:** Comparison of the measured and scaled flame parameters at several operating points for PPM operation. The \* symbols represents the ratio of the scaled and the measured values

Operating point [kW/ $\lambda/T_c$ ]	PPM operation			
	$n^*$	$\tau^*$	$\sigma^*$	$L_f^*$
40kW/1.7/300°C	0.85	0.98	0.95	0.94
50kW/1.7/300°C	1.00	0.99	1.12	1.00
60kW/1.7/300°C	0.90	1.04	0.95	1.04
50kW/1.5/300°C	0.93	1.09	1.02	0.90
50kW/1.5/200°C	0.96	1.09	1.00	1.02
50kW/1.7/200°C	1.30	0.83	0.82	1.13
Error Approx. [%]	5.33	5.19	4.87	3.18

## 6 Summary and Conclusions

This thesis presented the experimental and analytical results of an investigation concerned with lean premixed combustion instabilities in gas turbine combustors. The thesis is focused mainly on two aspects.

### **Development of alternative methods to determine the flame characteristics:**

Here alternative ways to determine the thermoacoustical characteristics of lean premixed flames in gas turbine systems, given by their flame transfer matrix (FTM) were investigated. An experimental investigation was performed on an atmospheric single burner test rig with two different burners: ALSTOM's EV5 burner and the generic TD1 swirl burner designed at Lehrstuhl für Thermodynamik. Two gas injection strategies were implemented to investigate the dynamics of thermoacoustic mechanisms. In the **Perfectly Premixed Mode** (PPM) operation, the mixture is generated far upstream of the burner and temporal as well as spatial mixture inhomogeneities are prevented by static mixers, where as in the **Injector Premixed Mode** (IPM) operation the mixture is generated by fuel injectors in the burner. This results in temporal as well as spatial mixture inhomogeneities which are convected by acoustic velocity fluctuations.

It is shown how the acoustic pressure field measured from the two forcing states using a *multi microphone method* (MMM) leads to the determination of the *direct* experimental burner and flame transfer matrices (BTM, FTM). Significant improvements were observed in the measurement technique compared to the previous works by choosing an appropriate reference plane and implementing a low reflecting boundary condition (almost anechoic end) using a perforated plate. This delivered benchmark data at several operating points for validating the theoretical and other alternative methods to de-

termine the dynamic flame characteristics of the premixed flames. But, the MMM requires two independent acoustic test states and a large number of sensors to fully characterize the acoustic field in a more complex system for e.g. in an annular test rig with 3-D acoustic field. Therefore, this method is restricted in principle to a single burner test rig with 1-D acoustic field.

A relatively simpler method investigated is the *hybrid* method, which is based on Rankine–Hugoniot relations and the experimental flame transfer function (FTF) from OH\*–chemiluminescence measurements for heat release fluctuations. The velocity fluctuations were calculated from the measured pressure field upstream of the burner and 1-D network theory. Although this method is simpler from the experimental point of view, it has the limitation that it cannot be applied to flames with high equivalence ratio fluctuations generated in IPM operation. Also, its application may often may not be possible in high pressure test rigs with limited optical accessibility.

An analytical flame model ( $n - \tau - \sigma$ ) based on the sensitive time lag approach has been implemented to determine the flame parameters. In this flame model the heat release fluctuations are assumed to be due to the mass flow fluctuations at the burner exit and fuel equivalence ratio fluctuations at the injector location. A Gaussian distribution of time lags is assumed to represent the distributed flame zone with finite axial extent. The results from the model were compared with the *direct* and *hybrid* methods. These comparison proved the equivalence of alternative methods to obtain the dynamic flame characteristics making it a global check between the measurements and modelling.

A low order network model to simulate the measurements from the single burner test rig has been developed. The burner and flame are treated as *compact elements* with free parameters which are obtained from the fit to the measurements. The influence of thermo viscous damping on the wave propagation in the ducts has been simulated by implementing damped ducts in the network model. The network model has been validated for both with and without combustion and with and with out the presence of damping. A good correspondence has been achieved between the measured and simulated pressure spectra's corresponding to the chosen microphone locations.

---

Finally a novel *model based regression method* which greatly reduces the experimental effort and therefore enables to provide the flame characteristics for many more operation points than previously possible was developed and validated. Here the FTM is determined using the network model based on Rankine-Hugoniot relations and an FTF model representing the flame by regression analysis of the acoustical measurements. The user can choose the range of model parameters to be optimized and perform the regression analysis such that the error is minimum. The dynamic flame characteristics are determined using only one test state in contrast with the *direct* method where two acoustically independent test states are required. This method is particularly advantageous for systems with 2-D acoustic fields e.g. annular combustion chambers.

#### **Development of scaling laws:**

After having measured benchmark data at several operating points, scaling rules that can be used to predict the dynamic flame characteristics were developed. A simplified geometric flame length model has been developed to calculate the flame length as a function of preheat temperature, burner exit velocity depending on thermal power and air excess ratio  $\lambda$ . The PIV measurements provided the basic flow field structure which is used to determine the flame geometry e.g. flow angle. The predicted flame lengths compared with the measurements showed a good consistency proving the capability of the model to calculate the flame lengths at several operating conditions.

The convective mean time delay ( $\tau$ ) and its axial distribution ( $\sigma$ ) has been obtained as directly proportional to the predicted flame lengths. A new correlation for calculating the interaction index ( $n$ ), which couples the flame and acoustics as a function of  $\tau, \sigma$  and the temperature ratio across the flames, has been proposed. Finally the comparison between the measured and scaled dynamic flame characteristics in terms of  $n, \tau$  and  $\sigma$  indicates a very good consistency validating the whole procedure of scaling the flame parameters in the present investigation. With these scaling rules in hand and using a low order network model, a detailed thermoacoustic stability analysis of gas turbine combustion systems can be performed at various operating conditions.

# A Appendix

## A.1 Acoustic FEM model

An acoustic FEM model<sup>1</sup> has been developed to better understand the complex acoustic field inside the EV5 burner, across the area jump and the physical boundaries of the test rig. In particular, the FEM model has proved to be very effective in illustrating the large acoustic velocity gradients present at the inlet of the burner slots. These explain the observed problems with CTA measurements (see chapter 4). A Schematic of the FEM model representing the single burner test rig is shown in Fig. A.1.

The FEM model mainly consists of three sub-domains representing plenum unit, burner unit and combustion chamber unit. The characteristics of each sub-domain is listed in table A.1. All the sub-domains are discretized into tetrahedral elements whose size is dependent on the geometric complexity. The minimum mesh quality factor<sup>2</sup> ( $QF$ ) around 0.3 was obtained by refining the mesh. The acoustic simulation was carried out without mean flow and without combustion, i.e., isentropic relations are valid. The problem is solved in the frequency domain using the time-harmonic acoustics application mode. The model equation is a slightly modified Helmholtz's equation for the acoustic pressure,  $p$ .

$$\nabla \cdot \left( -\frac{\nabla p}{\rho} \right) - \frac{\omega^2 p}{c^2 \rho} = 0 \quad (\text{A.1})$$

---

<sup>1</sup>using 3D acoustics mode of the COMSOL Multiphysics commercial software, Version 3.2

<sup>2</sup>The mesh element quality factor is related to the aspect ratio, which means that anisotropic elements can get a low quality measure even though the element shape is reasonable. Its value lies in between 0 and 1. For tetrahedral elements, COMSOL Multiphysics computes the mesh quality with the formula:  $QF = \frac{72\sqrt{3}V}{(h_1^2+h_2^2+h_3^2+h_4^2+h_5^2+h_6^2)^{3/2}}$  where  $V$  is the volume, and  $h_1, h_2, h_3, h_4, h_5, h_6$  are the edge lengths of the tetrahedron. If  $QF > 0.1$  the mesh quality should not effect the quality of the solution [8]

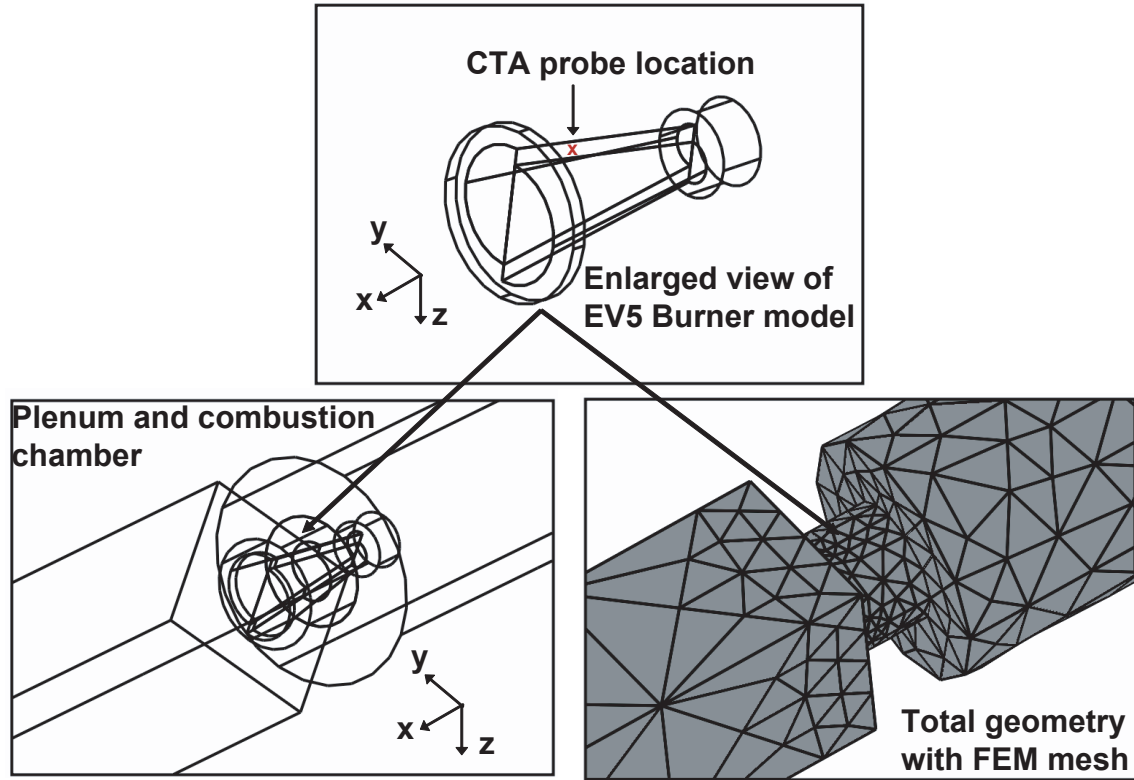


**Figure A.1:** *Acoustic FEM model representing the single burner test rig with its main components.*

**Table A.1:** *Characteristics of the sub-domains in the FEM model*

Sub-domain	Dependent variable	Application mode properties	Space dimension
Plenum	$p_{pl}$	Lagrange-quadratic, time harmonic analysis, weak constrains: off	3-D
EV5 burner	$p_{EV5}$	-same-	-same-
Combustion chamber	$p_{cc}$	-same-	-same-

A constant pressure source of excitation and an impedance boundary condition at upstream and downstream ends, respectively has been implemented. A hard wall boundary condition has been used to represent the walls of the test rig. A simulation was carried out with upstream excitation and acoustic pressure and velocities were obtained at prescribed microphone locations as

in the measurement set up. Also, the pressure and velocity field at the inlet to the burner slots was obtained as shown previously in section 4.4. The results revealed the existence of large pressure and velocity gradients inside the slots leading to a 3-D acoustic field there, while a 1-D planar acoustic field is observed at the rest of the locations.

In principle it would be interesting to find a position where the axial acoustic velocity component ( $u_x$ ) is larger than the other two components ( $u_y, u_z$ ) within the slots with 3-D acoustic field. Towards this, data is obtained at several points in the vicinity of the CTA probe location (see Fig. A.1, middle of the slot is at  $(x,y,z)=[-0.027,0.000,0.017]$ ) for a frequency of 350 Hz as shown in table A.2. The result shows that only at  $(-0.027, -0.002, 0.017)$  will give a slightly higher axial velocity component compared to the other two components. Nonetheless, the data also shows that all three components are of the same order and that their value changes substantially in the CTA region.

**Table A.2:** Axial acoustic velocity component normalized with its local velocity obtained at various locations in the EV5 burner slot.  $(0,0,0)$  corresponds to the burner center axis at the burner exit plane

Location (x,y,z) [m]	$u_x/u$	$u_y/u$	$u_z/u$
$(-0.027, -0.002, 0.015)$	0.53	0.76	0.36
$(-0.027, -0.002, 0.017)$	<b>0.62</b>	0.60	0.51
$(-0.027, -0.002, 0.019)$	0.64	0.37	0.66

In addition, a simulation of the MMM was carried out to obtain the BTM numerically. A comparison (not shown) has been made with the measured BTM. Since the FEM model is isentropic the results illustrates the influence of damping on the BTM coefficients. In future this model, in particular with the geometry retained, can be developed further to include the flame as an additional source term and implementing suitable damping and heat losses.

## A.2 Flame length model

Here, a detailed derivation of the flame length model presented in chapter 5 is presented. The flame surface is approximated by a conical shell anchoring at inner radius  $r_i$  (at  $x = 0$ ) of the annular burner exit and extends until the end of the reaction zone with radius  $r_f$  (at  $x = L_f$ ) as previously presented in the Fig. 5.1. Now, consider only a small element of this flame surface with radius  $r(x)$  as a function of axial distance ( $x$ ) as shown in Fig. A.2.

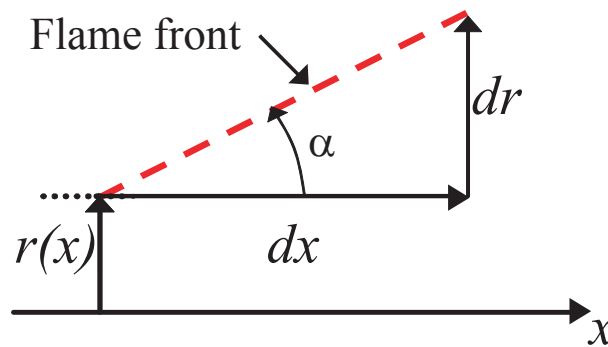


**Figure A.2:** Schematic of the flame length model

From the flame geometry, the surface area of the flame can be obtained as

$$A_f = \int_0^{L_f} 2\pi r(x) \frac{dx}{\cos \alpha} \quad (\text{A.2})$$

$$= \int_{r_i}^{r_f} 2\pi r \frac{dr}{\sin \alpha} \quad (\text{A.3})$$

$$= \frac{\pi}{\sin \alpha} (r_f^2 - r_i^2). \quad (\text{A.4})$$

Now, from the continuity equation we have the relation for the flow field between the burner exit plane ( $A_0, U_0$ ) and flame zone ( $A_f, s_t$ ) as

$$A_0 U_0 = A_f s_t. \quad (\text{A.5})$$

Substituting the Eqn. A.4 into Eqn. A.5 and then using the relation  $r_f = r_i + L_f \tan \alpha$  we get a relation for flame length as follows:

$$s_t A_f = s_t \frac{\pi}{\sin \alpha} (r_f^2 - r_i^2) \quad (\text{A.6})$$

$$\Rightarrow r_f = \sqrt{\frac{A_0 U_0 \sin \alpha}{s_t \pi} + r_i^2} \quad (\text{A.7})$$

$$L_f = \frac{r_f}{\tan \alpha} - \frac{r_i}{\tan \alpha} \quad (\text{A.8})$$

$$= \sqrt{\frac{A_0 U_0 \cos \alpha}{s_t \pi \tan \alpha} + \frac{r_i^2}{\tan^2 \alpha}} - \frac{r_i}{\tan \alpha}. \quad (\text{A.9})$$

### A.3 Data post processing

In this section various software routines/tools used to post process different data sets from the measurements will be presented. A similar approach as previously made at Lehrstuhl für Thermodynamik by Fischer, 2004 and Eckstein, 2004 [18,22] has been implemented. In particular, the measurement of burner and flame transfer matrices using the MMM is the key for the present investigation. The measurement procedure is outlined in section 3.2.1. Here the post processing of the acquired data files will be discussed.

**Setup file (.stp):** This file gives the information on the location of the microphones embedded in a code for each microphone and for each measurement. This information is used later in the protocol file as input to the Mathematica routines to assign corresponding pressure vectors. The position for each microphone location can be decoded from the notation given in table A.3.

The position of each microphone is measured and assigned to its code correspondingly. Optionally, any microphone channel can be disregarded from further post processing by setting the flag variable to a value of one as shown in table A.3. It is useful to disregard microphones in the low frequency domain whose measurement values show an unexpected behavior.

**Protocol file (.prc):** This file contains all necessary operating and data acquisition parameters:

**Table A.3:** *Measurement setup file containing the microphone position code*

Code	Position
20xx	Microphone in primary square combustion chamber
40xx	For CTA (only one fixed position)
50xx	Microphone in secondary square combustion chamber
60xx	Microphone in Plenum
x1xx	Set channel dummy flag

- Mass flow rate of air and fuel (g/s)
- Temperature readings from thermocouples
- Static pressure drop across the burner
- Microphone amplification factor and their respective locations
- Sampling frequency and number of frequencies investigated
- Number of measurement loops per frequency

**FFT file (.fft):** It contains the *Fast Fourier Transformed* (FFT) amplitudes ( $A_i$ ) and phases  $\phi_i$  of measured pressure and other dynamic signals obtained from CTA and UV-photomultiplier. The structure of the *FFT* file is given in table A.4.

**Table A.4:** *FFT file containing the amplitudes and phases obtained from several dynamic signals per measurement loop*

Meas. number	$f_{ideal}$	$f_{actual}$	$A_1 \dots A_{10}$	Meas. number	$f_{ideal}$	$f_{actual}$	$\phi_1 \dots \phi_{10}$
--------------	-------------	--------------	--------------------	--------------	-------------	--------------	--------------------------

The data is always acquired in this standard form with up to ten channels including the CTA, UV photomultiplier and the reference signal from the siren. The microphone signals acquired in volts are converted to their respective

pressure signal (in Pa) using their sensitivity and amplification factor (mV/Pa) before performing online Fourier transformation. The FFT file data is originally stored in binary (big endian 32 bit-float) format requiring less memory space. This file is later converted to an IEE standard binary format to be able to read in Mathematica. The phase values of the reference signal stored in the last column are subtracted from phase values of all other signals before being averaged over several measurement loops per frequency.

**Calibration file (.txt):** This file contains the calibration coefficients with respect to a selected reference microphone. The calibration coefficients are applied to their respective microphone signal and also the reference phase is subtracted from all other signals to minimize the relative errors between the microphones.

All these files are made available in a single folder containing the Mathematica routines to calculate the Riemann invariants  $f$  and  $g$  up- and downstream separately from the fit procedure (see section 3.2.1). The output of this step is the file (.xls) containing the Riemann invariants for each frequency and for the two cases, with upstream excitation (case “a”) and downstream excitation (case “b”). This file is used to perform the matrix multiplication to obtain finally the transfer matrices of burner and flame.

# Bibliography

- [1] Abom. A note on the experimental determination on acoustical two-port matrices. *J. of Sound and Vibration*, 155(1):185–188, 1992.
- [2] P. R. Alemela, D. Fanaca, F. Ettner, C. Hirsch, T. Sattelmayer, and B. Schuermans. Flame transfer matrices of a premixed flame and a global check with modelling and experiments. GT2008-50111 in Proc. of ASME Turbo Expo 2008, Berlin, Germany, 2008.
- [3] M. Auer, C. Gebauer, K. Moesl, C. Hirsch, and T. Sattelmayer. Active Instability Control: Feedback of Combustion Instabilities on the Injection of Gaseous Fuel. *J. of Eng. for Gas Turbines and Power*, 127:748–754, 2005.
- [4] M. P. Auer, C. Hirsch, and T. Sattelmayer. Influence of air and fuel mass fluctuations in a premix swirl burner on flame dynamics. GT2006-90127 in Proc. of ASME Turbo Expo 2006, Barcelona, Spain, 2006.
- [5] R. Borghi. *On the Structure and Morphology of Turbulent Premixed Flames*. Recent Advances in Aerospace Sciences. Plenum Press, New York, 1985.
- [6] B.-T. Chu. On the generation of pressure waves at a plane flame front. *4th Symp (Int.) on Combustion*, 1953.
- [7] P. Clavin, J. Kim, and F. Williams. Turbulence induced noise effects on high frequency combustion instabilities. *Combust. Sci. and Tech.*, 96:61–84, July 1994.
- [8] COMSOL. *COMSOL Multiphysics User's Guide*, 3.2 edition, September 2005.

- 
- [9] S. M. Correa. A review of nox formation under gas turbine combustion conditions. *Combust. Sci. and Tech.*, 87:329–362, October 1992.
- [10] L. Crocco and S. I. Cheng. *Theory of combustion instability in liquid propellant rocket motors*. Butterworths Science Publication, note: AGARDOGRAPH N 8, 1956.
- [11] F. E. C. Culick. Some recent results for nonlinear acoustics in combustion chambers. *AIAA Journal*, 32(1):146–169, 1994. vorhanden.
- [12] J. Curlier. Thermoacoustic oscillations in combustion chambers. Master's thesis, University of Washington, 1996.
- [13] G. Damköhler. Der Einfluß der Turbulenz auf die Flammengeschwindigkeit in Gasmischungen. *Zeitschrift f. Elektrochem. u. angew. Chemie*, 46:601 – 626, 1940.
- [14] P. O. A. L. Davies. Practical flow duct acoustics. *J. of Sound and Vibration*, 124:91–115, 1988.
- [15] A. P. Dowling. The calculation of thermoacoustic oscillations. *J. of Sound and Vibration*, 180(4):557–581, 1995.
- [16] A. P. Dowling. Modeling and control of combustion oscillations. GT2005-68452 in Proc. of ASME Turbo Expo 2005, Reno-Tahoe, Nevada, USA, 2005.
- [17] S. Ducruix, D. Durox, and S. Candel. Theoretical and experimental determinations of the flame transfer function of a laminar premixed flame. *Proc. of the Comb. Institute*, 28:765–773, 2000.
- [18] J. Eckstein. *On the Mechanisms of Combustion Driven Low-Frequency Oscillations in Aero-Engines*. PhD thesis, TU München, 2004.
- [19] J. Eckstein, E. Freitag, C. Hirsch, and T. Sattelmayer. Experimental study on the role of entropy waves in low-frequency oscillations in a rql combustor. *J. of Eng. for Gas Turbines and Power*, 128(2):264–270, 2006.
- [20] D. Fanaca, P. R. Alemela, F. Ettner, C. Hirsch, T. Sattelmayer, and B. Schuermans. Determination and comparison of the dynamic characteristics of

- a perfectly premixed flame in both single and annular combustion chambers. GT2008-50781 in Proc. of ASME Turbo Expo 2008, Berlin, Germany, 2008.
- [21] D. Fanaca, P. R. Alemela, C. Hirsch, T. Sattelmayer, and B. Schuermans. Comparison of the flow field of a swirl stabilised premixed burner in an annular and a single burner combustion chamber. GT2009-59884 in Proc. of ASME Turbo Expo 2009, Orlando, Florida, USA, 2009. To be published in the J. Eng. for Gas Turbines and Power.
- [22] A. Fischer. *Hybride, thermoakustische Charakterisierung von Drallbrennern*. PhD thesis, TU München, Munich, Germany, April 2004.
- [23] A. Fischer, C. Hirsch, and T. Sattelmayer. Comparison of multi-microphone transfer matrix measurements with acoustic network models of swirl burners. *J. of Sound and Vibration*, 298:73–83, 2006.
- [24] A. Fleifil, A. M. Annaswamy, Z. A. Ghoneim, and A. F. Ghoniem. Response of a laminar premixed flame to flow oscillations: A kinematic model and thermoacoustic instability results. *Combust. and Flame*, 106:487–510, 1996.
- [25] P. Flohr, C. O. Paschereit, B. van Roon, and B. Schuermans. Using cfd for time-delay modeling of premix flames. 2001-GT-0376 in Proc. of ASME Turbo Expo 2001, New Orleans, Louisiana, USA, 2001.
- [26] E. Freitag, H. Konle, M. Lauer, C. Hirsch, and T. Sattelmayer. Pressure influence on the flame transfer function of a premixed swirling flame. GT2006-90540 in Proc. of ASME Turbo Expo 2006, Barcelona, Spain, 2006.
- [27] Y. Fu, J. Cai, S.-M. Jeng, and H. Mongia. Confinement effects on the swirling flow of a counter-rotating swirl cup. GT2005-68622 in Proc. of ASME Turbo Expo 2005, Reno-Tahoe, Nevada, USA, 2005.
- [28] A. Gentemann, A. Fischer, S. Evesque, and W. Polifke. Acoustic transfer matrix reconstruction and analysis for ducts with sudden change of area. AIAA-2003-3142 in 9th AIAA/CEAS Aeroacoustics Conference and Exhibit, Hilton Head, SC, USA, 2003.

- [29] P. Griebel, R. Schären, P. Siewert, R. Bombach, A. Inauen, and W. Kreutner. Flow field and structure of turbulent high-pressure premixed methane/air flames. GT2003-38398 in Proc. of ASME Turbo Expo 2003, Atlanta, Georgia, USA, 2003.
- [30] E. J. Gutmark and F. F. Grinstein. Flow Control with noncircular Jets. *Annual Review of Fluid Mechanics*, Vol. 31:239–272, 1999.
- [31] L. C. Haber, W. R. Saunders, and V. K. Khanna. An examination of the relationship between chemiluminescent light emissions and heat release rate under non-adiabatic conditions. GT-2000-0121 in Proc. of IGTI 2000, Munich, Germany, 2000.
- [32] M. A. Heckl. Active control of the noise from a rijke tube. *J. of Sound and Vibration*, 124:117–133, 1988.
- [33] C. Hirsch, D. Fanaca, P. Reddy, W. Polifke, and T. Sattelmayer. Influence of the swirler design on the flame transfer function of premixed flames. GT2005-68195 in Proc. of ASME Turbo Expo 2005, Reno-Tahoe, Nevada, USA, 2005.
- [34] S. Hoffmann, P. Habisreuther, and B. Lenz. Development and assessment of correlations for predicting stability limits of swirling flames. *Chem. Eng. and Processing*, 33:393–400, 1994.
- [35] S. Hoffmann, B. Lenze, and H. Eickhoff. Results of experiments and models for predicting stability limits of turbulent swirling flames. 97-GT-396 in Int. Gas Turbine & Aeroengine Congr. & Exh., Orlando, USA, 1997.
- [36] A. Huber, L. Leandro, and W. Polifke. tax - a low-order modelling tool for thermo- and aero-acoustic instabilities, 2008. Private communication.
- [37] J. J. Keller. Thermoacoustic oscillations in combustion chambers of gas turbines. *AIAA Journal*, 33(12):2280–2287, 1995.
- [38] J. J. Keller, W. Egli, and J. Hellat. Thermally induced flow frequency oscillations. *J. of Appl. Math. Physics*, 36, March 1985.
- [39] C. Kühlsheimer and H. Büchner. Combustion dynamics of turbulent swirling flames. *Combust. and Flame*, 131:70–84, 2002.

- [40] J. Kopitz and W. Polifke. Cfd-based application of the nyquist criterion to thermo-acoustic instabilities. *J. of Computational Physics*, 227(14):6754–6778, 2008.
- [41] W. Krebs, S. Hoffmann, B. Prade, M. Lohrmann, and H. Büchner. Thermoacoustic flame response of swirl flames. GT-2002-30065 in Proc. of ASME Turbo Expo 2002, Amsterdam, The Netherlands, 2002.
- [42] U. Krüger, J. Hüren, S. Hoffmann, W. Krebs, P. Flohr, and D. Bohn. Prediction and measurement of thermoacoustic improvements in gas turbines with annular combustion systems. *J. of Eng. for Gas Turbines and Power*, 123:557–565, 2001.
- [43] K. Kunze. *Untersuchung des thermoakustischen Flammenübertragungsverhaltens in einer Ringbrennkammer*. PhD thesis, Technische Universität München, München, Germany, 2004.
- [44] K. Kunze, C. Hirsch, and T. Sattelmayer. Transfer function measurements on a swirl stabilized premix burner in an annular combustion chamber. GT2004-53106 in Proc. of ASME Turbo Expo 2004, Vienna, Austria, 2004.
- [45] A. H. Lefebvre. *Gas Turbine Combustion*. McGraw-Hill, 1983.
- [46] T. Lieuwen and V. Yang, editors. *Combustion Instabilities in Gas Turbine Engines: Operational Experience, Fundamental Mechanisms, and Modeling*. ISBN 156347669X in Progress in Astronautics and Aeronautics. AIAA, 2006.
- [47] T. Lieuwen and B. T. Zinn. The role of equivalence ratio oscillations in driving combustion instabilities in low nox gas turbines. Proc. of the 27th Symposium (International) on Combustion, Pittsburgh, 1998.
- [48] M. Lohrmann and H. Büchner. Scaling of stability limits in lean-premixed gas turbine combustors. GT2004-53710 in Proc. of ASME Turbo Expo 2004, Vienna, Austria, 2004.
- [49] M. Lohrmann, H. Büchner, N. Zarzalis, and N. Krebs. Flame transfer function characteristics of swirl flames for gas turbine applications. GT2003-38113 in Proc. of ASME Turbo Expo 2003, Atlanta, Georgia, 2003.

- [50] M. Mastrovito, S. M. Camporeale, A. Forte, and B. Fortunato. Analysis of pressure oscillations data in gaz turbine annular combustion chamber equipped with passive damper. GT2005-69056 in Proc. of ASME Turbo Expo 2005, Reno-Tahoe, Nevada, USA, 2005.
- [51] K. R. McManus, T. Poinsot, and S. M. Candel. A review of active control of combustion instabilities. *Prog. Energy Combust. Sci.*, 19:1–29, 1993.
- [52] H. J. Merk. An analysis of unstable combustion of premixed gases. *Appl. Sci. Res.*, 6:500–511, 1956.
- [53] M. L. Munjal. *Acoustics of ducts and mufflers*. John Wiley & Sons, 1987.
- [54] M. L. Munjal and A. G. Doige. Theory of a two source-location method for direct experimental evaluation of the four-pole parameters of an aeroacoustic element. *J. of Sound and Vibration*, 141, 1990.
- [55] D. R. Noble, Q. Zhang, A. Shareef, J. Tootle, A. Meyers, and T. Lieuwen. Syngas mixture composition effects upon flashback and blowout. GT2006-90470 in Proc. of ASME Turbo Expo 2006, Barcelona, Spain, 2006.
- [56] C. Pankiewitz. *Hybrides Berechnungsverfahren für thermoakustische Instabilitäten von Mehrbrennersystemen*. PhD thesis, Technische Universität München, 2004.
- [57] C. Pankiewitz, S. Evesque, W. Polifke, and T. Sattelmayer. Stability analysis of annular gas turbine combustors. LECT Workshop on Instabilities in Aero-Engine Combustors, Stuttgart, Germany, 2001.
- [58] C. Pankiewitz and T. Sattelmayer. Time domain simulation of combustion instabilities in annular combustors. *J. of Eng. for Gas Turbines and Power*, 125(3):677–685, 2003.
- [59] C. O. Paschereit and W. Polifke. Investigation of the thermoacoustic characteristics of a lean premixed gas turbine burner. 98-GT-582 in Int. Gas Turbine & Aeroengine Congr. & Exh., Stockholm, Sweden, 1998.

- [60] C. O. Paschereit, B. Schuermans, W. Polifke, and O. Mattson. Measurement of transfer matrices and source terms of premixed flames. 99-GT-133 in Int. Gas Turbine & Aeroengine Congr. & Exh., Indianapolis, Indiana, USA, 1999.
- [61] C. O. Paschereit, B. Schuermans, W. Polifke, and O. Mattson. Measurement of transfer matrices and source terms of premixed flames. *J. of Eng. for Gas Turbines and Power*, 124:239–247, 2002.
- [62] C. O. Paschereit, W. Weisenstein, and E. J. Gutmark. Role of coherent structures in acoustic combustion control. A98-32792 in 29th AIAA Fluid Dynamics Conference, Albuquerque, New Mexico, 1998.
- [63] M. C. A. M. Peters, A. Hirschberg, A. J. Reijnen, and A. P. J. Wijnands. Damping and reflection coefficient measurements for an open pipe at low mach and low helmholtz numbers. *J. of Fluid Mech.*, 256:499–534, 1993.
- [64] N. Peters. Kinetic foundation of thermal flame theory. *Advances in combustion science: In honor of Ya. B Zeldovich, Prog. Astronautics and Aeronautics, AIAA*, (173):73–91, 1997.
- [65] N. Peters. The turbulent burning velocity for large scale and small scale turbulence. *J. of Fluid Mech.*, 384:107–132, 1999.
- [66] N. Peters. *Turbulent Combustion*. Cambridge University Press, 2000. ISBN 0-521-66082-3.
- [67] T. Poinsot, A. Trounev, D. Veynante, S. Candel, and E. Esposito. Vortex-driven acoustically coupled combustion instabilities. *J. of Fluid Mech.*, 177, 1987.
- [68] W. Polifke. *System modelling and stability analysis*. VKI lecture Series "Basics of Aero- and thermoacoustics", Von Karman Institute, Belgium, 3rd-7th Dec 2007.
- [69] W. Polifke and A. Gentemann. Order and realisability of impulse response filters for accurate identification of acoustical multi-ports from transient cfd. *Int. J. of Acoustics and Vibration*, 9:139–148, 2004.

- [70] W. Polifke, J. Kopitz, and A. Serbanovic. Impact of the fuel time lag distribution in elliptical premix nozzles on combustion stability. AIAA 2001-2104 in 7th AIAA/CEAS Aeroacoustic Conference May 28-30, 2001/ Maastricht, The Netherlands, 2001.
- [71] W. Polifke, C. O. Paschereit, and K. Döbbeling. Constructive and destructive interference of acoustic and entropy waves in a premixed combustor with a choked exit. *Int. J. of Acoustics and Vibration*, 6(3):1–12, 2001.
- [72] W. Polifke, A. Poncet, C. O. Paschereit, and K. Döbbeling. Reconstruction of acoustic transfer matrices by instationary computational fluid dynamics. *J. of Sound and Vibration*, 245(3):483–510, 2001.
- [73] W. Polifke, J. van der Hoek, and B. Verhaar. Everything you always wanted to know about f and g. Technical report, ABB Corporate Research, Baden,CH, 1997.
- [74] R. Price, I. Hurle, and T. Sugden. Optical studies of the generation of noise in turbulent flames. *Proc. of the Comb. Institute*, 12:1093–1102, 1968.
- [75] M. Raffel, C. Willert, and J. Kompenhans. *Particle Image Velocimetry*. Springer Berlin, Heidelberg, New York, 1st edition edition, 1998.
- [76] R. L. Raun, M. W. Beckstead, J. C. Finlinson, and K. P. Brooks. A review of rijke tubes, rijke burners and related devices. *Prog. Energy Combust. Sci.*, 19:313–364, 1993.
- [77] L. Rayleigh. The explanation of certain acoustical phenomena. *Nature*, 18:319–321, 1878.
- [78] S. W. Rienstra and A. Hirschberg. *An Introduction to Acoustics*. Eindhoven University of Technology, October 2004.
- [79] D. Ronneberger and Ahrens. Wall shear stress caused by small amplitude perturbations of turbulent boundary-layer flow : an experimental investigation. *J. of Fluid Mech.*, 32, 1977.
- [80] M. Russ, A. Meyer, and H. Büchner. Scaling thermo-acoustic characteristics of lpp swirl flames. GT2007-27775 in Proc. of ASME Turbo Expo 2007, Montreal, Canada, 2007.

- [81] T. Sattelmayer. Influence of the combustor aerodynamics on combustion instabilities from equivalence ratio. *J. of Eng. for Gas Turbines and Power*, 125:11–19, 2003.
- [82] T. Sattelmayer, M. Felchlin, J. Haumann, J. Hellat, and D. Styner. Second-generation low-emission combustors for abb gas turbines: Burner development and tests at atmospheric pressure. *J. of Eng. for Gas Turbines and Power*, 114:118–125, 1992.
- [83] T. Sattelmayer and W. Polifke. Assessment of methods for the computation of the linear stability of combustors. *Combust. Sci. and Tech.*, 175(3):453–476, 2003.
- [84] T. Sattelmayer and W. Polifke. A novel method for the computation of the linear stability of combustors. *Combust. Sci. and Tech.*, 175(3):477–497, 2003.
- [85] K. C. Schadow, E. Gutmark, T. P. Parr, D. M. Parr, K. J. Wilson, and J. E. Crump. Large-scale coherent structures as drivers of combustion instability. *Combust. Sci. and Tech.*, 64:167–186, 1989.
- [86] H. Schmid, P. Habisreuther, and W. Leuckel. A model for calculating heat release in premixed turbulent flames. *Combust. and Flame*, 113:79–91, 1998.
- [87] B. Schuermans. *Modelling and Control of Thermoacoustic Instabilities*. PhD thesis, Ecole Polytechnique Federale De Lausanne, Switzerland, 2003.
- [88] B. Schuermans. Entwicklung eines fortschrittlichen Systems zur Verbrennungskontrolle. Abschlussbericht 0327710K, TD-TUM, AG Turbo COOREFF-T, Vorhaben-Nr. 2.1.2, 2008.
- [89] B. Schuermans, V. Bellucci, F. Guethe, F. Meili, P. Flohr, and C. O. Paschereit. A detailed analysis of thermoacoustic interaction mechanisms in a turbulent premixed flame. GT2004-53831 in Proc. of ASME Turbo Expo 2004, Vienna, Austria, 2004.

- [90] B. Schuermans, F. Guethe, and W. Mohr. Optical transfer function measurements for technically premixed flames. GT2008-51500 in Proc. of ASME Turbo Expo 2008, Berlin, Germany, 2008.
- [91] B. Schuermans, H. Luebcke, D. Bajusz, and P. Flohr. Thermoacoustic analysis of gas turbine combustion systems using unsteady cfd. GT2005-68393 in Proc. of ASME Turbo Expo 2005, Reno-Tahoe, Nevada, USA, 2005.
- [92] B. Schuermans, W. Polifke, and C. O. Paschereit. Modeling transfer matrices of premixed flames and comparison with experimental results. 99-GT-132 in Int. Gas Turbine & Aeroengine Congress & Exhibition, Indianapolis, Indiana, USA, 1999.
- [93] B. Schuermans, W. Polifke, C. O. Paschereit, and J. H. van der Linden. Prediction of acoustic pressure spectra in combustion systems using swirl stabilized gas turbine burners. 2000-GT-0105 in Proc. of IGTI TE 2000, Munich, Germany, 2000.
- [94] P. Siewert. *Flame front characteristics of turbulent lean premixed methane / air flames at high-pressure*. PhD thesis, Swiss Federal Institute of Technology Zurich, 2006.
- [95] A. Stella, G. Guj, J. Kompenhans, M. Raffel, and H. Richard. Application of particle image velocimetry to combusting flows. *Exp. in Fluids*, 30:167–180, 2001.
- [96] W. C. Strahle. On combustion generated noise. *J. of Fluid Mech.*, 49(2):399–414, 1971.
- [97] S. R. Turns. *An Introduction to Combustion*. McGraw-Hill, Boston, 2000.
- [98] A. Winkler, J. Wäsle, and T. Sattelmayer. Development of a hs-lif-system for lagrangian correlation measurement. *Exp. in Fluids*, 46(4):607–616, 2008.
- [99] J. Wäsle, A. Winkler, and T. Sattelmayer. Spatial coherence of the heat release fluctuations in turbulent jet and swirl flames. *Flow Turbulence and Combustion*, 75:29–50, 2005.